University of Nottingham
UK | CHINA | MALAYSIA

Coupled Electrothermal Modelling of Plasma using Unstructured Transmission-Line Modelling Method

Kaiqi Yan

This thesis is submitted to the University of Nottingham

for the degree of Doctor of Philosophy

George Green Institute for Electromagnetics Research

Department of Electrical and Electronic Engineering

University of Nottingham

September 2023

Supervisors:

Prof Ana Vukovic

Prof Phillip Donald Sewell

Prof Trevor Mark Benson (retired)

Declaration

This thesis is substantially my own work. Where reference has been made to other research this is acknowledged in the text and bibliography.

Kaiqi Yan

September 2023

Publications associated with this thesis:

(Under Review) K. Yan, A. Vukovic, and P. Sewell, "Two-dimensional coupled electrothermal model of plasma using unstructured transmission-line modelling for lightning protection simulations," *IEEE Journal on Multiscale and Multiphysics Computational Techniques*, 2023

K. Yan, A. Vukovic, and P. Sewell, "Two-dimensional TE series node transmission-line modelling based on unstructured triangular meshes," in *2022 52nd European Microwave Conference (EuMC)*, pp. 448–451, 2022.

K. Yan, A. Vukovic, P. Sewell, and T. M. Benson, "Two-dimensional thermal diffusion equation solver based on unstructured transmission-line modelling and optimal Delaunay Triangular meshes," *IEEE Journal on Multiscale and Multiphysics Computational Techniques*, vol. 7, pp. 268–275, 2022.

Acknowledgement

I would like to thank my supervisors, my family, my friends, people who I love, people who love me, and all that help and support me. Words are not enough to express my sincerest thanks; I will cherish these unforgettable memories through my live.

Abstract

The protection against the lightning strike is widely researched and applied to commercial and engineering facilities such as modern aircraft and wind turbine blades, and the simulation investigation on lightning effects involves the electrothermal modelling of plasma. The aim of this work is to derive and implement a two-dimensional time-domain two-way coupled electrothermal numerical scheme to model plasma materials. This work mainly focuses on the applications and extensions of the unstructured transmission-line modelling (TLM) methods, namely the UTLM methods. In order to cope with complex geometries, this work uses two-dimensional Delaunay triangular meshes. The transverse electric series node version of the two-dimensional electromagnetic UTLM method is proposed to directly model the principal transverse electric field components which are of the interest in lightning effects analyses, and the two-dimensional thermal UTLM method is proposed to conduct the heat diffusion simulation using the same mesh as that of the electromagnetic simulation so that the re-sampling of the field profile in unstructured grids is avoided. The plasma material is described by using the Drude plasma model to reflect its frequency-dependent permittivity, and the way to embed it into the electromagnetic UTLM method requires the newly-designed digital filters. The two-way coupled plasma modelling scheme integrates the two-dimensional Drude-embedded electromagnetic UTLM method and the two-dimensional thermal UTLM method, in which the plasma parameters and the temperature are updated according to each other in each simulation time step, forming the two-way closed-loop coupling. The two-way coupled plasma model is applied to simulate the plasmonic nanotip waveguide and to investigate the lightning effects on segmented lightning diverter strips.

Contents

1 Introduction **1**

1.1 Background and Motivation 1

1.2 Review of Electrothermal Coupling Methods 2

1.2.1 Overview 2

1.2.2 One-way Electrothermal Coupling 3

1.2.3 Two-way Electrothermal Coupling 3

1.2.4 TLM-Related Electrothermal Models 7

1.3 Review of Plasma Modelling Methods 8

1.3.1 Hydrodynamics Based Models 8

1.3.2 The Drude Model of Plasma 9

1.4 Review of Lightning Effects Investigations 10

1.5 Organisation of the Thesis 11

2 Cartesian EM TLM Method **13**

2.1 Overview 13

2.2 One-dimensional TLM 15

2.2.1 Model Derivation 15

2.2.2 Link Model and Stub Model 16

2.2.3 Scattering and Connection 17

2.3 Two-dimensional Shunt Model 20

2.3.1 Model Derivation 20

2.3.2 Scattering and Connection 22

2.4 Two-dimensional Series Model 26

2.4.1 Model Derivation 26

2.4.2 Scattering and Connection 28
2.5 Conclusion 30

3 Cartesian Thermal TLM Method 31
3.1 Overview 31
3.1.1 Heat Diffusion Equation 32
3.2 One-dimensional Thermal TLM 33
3.2.1 Model Derivation 33
3.2.2 Scattering and Connection 34
3.3 Two-dimensional Shunt Model 36
3.3.1 Model Derivation 36
3.3.2 Scattering and Connection 38
3.4 Conclusion 40

4 Two-dimensional EM UTLM 41
4.1 Overview 41
4.2 Delaunay Triangulation 43
4.2.1 Definition and Triangulation Algorithm 43
4.2.2 Space Discretisation in UTLM 45
4.3 Two-dimensional Unstructured Shunt Model 47
4.3.1 Review 47
4.3.2 Assumptions and Mappings 48
4.3.3 Derivation of Electric Component Quantities 50
4.3.4 Scattering and Connection 52
4.4 Two-dimensional Unstructured Series Model 54
4.4.1 Review 54
4.4.2 Node Layout and Quantity Mapping 55
4.4.3 Derivation of Electrical Component Quantities 56
4.4.4 Time Step and The Position of the Port 57
4.4.5 Scattering and Connection 59
4.4.6 Cylindrical Resonator Validation Test 61

4.4.7 Nanotip Waveguide 62
4.4.8 Field Components Extraction 64
4.5 Mesh Optimisation 66
4.6 Remarks on using the Delaunay Mesh 69
4.7 Conclusion 69

5 Two-dimensional Thermal UTLM 71
5.1 Overview 71
5.2 Theory of Thermal UTLM 72
5.2.1 Derivation of Electrical Component Quantities 72
5.2.2 Transmission-Line Model 76
5.2.3 Scattering and Connection 78
5.2.4 Initial Conditions and Boundary Conditions 79
5.2.5 Node Clustering and Mesh Optimisation 80
5.3 Results 81
5.3.1 Convergence Test 81
5.3.2 Mesh with Quadrilateral Combined Nodes 85
5.3.3 Simulation of Power Transistor 86
5.4 Conclusion 92

6 Drude Plasma Model and the Implementations 93
6.1 Plasma Physics and the Drude Model 93
6.1.1 Overview 93
6.1.2 The Drude Model 94
6.2 Expression of Electron Concentration 97
6.3 Implementation of the Drude Model 99
6.3.1 Overview 99
6.3.2 In Cartesian Uniform Grids 99
6.3.3 In Unstructured Triangular Grids 103
6.4 Results 106
6.4.1 Power Density Calculation Method 106

6.4.2 Nanotip Waveguide 110
6.5 Conclusion 113

7 Coupled UTLM and Applications on Lightning Protection 114
7.1 Overview 114
7.2 Two-way Electrothermal Coupling 116
7.3 Results 117
7.3.1 Two Lightning Strip Buttons 117
7.3.2 Lightning Diverter Strips Designs 122
7.4 Conclusion 124

8 Conclusions and Future Work 125
8.1 Summary of the Thesis 125
8.2 Future Work 126

List of Symbols

Symbol	Physical Quantity
$\boldsymbol{E}$	Electric Field Strength
$\boldsymbol{H}$	Magnetic Field Strength
$\boldsymbol{B}$	Magnetic Flux Density
ρ	Electric Charge Density
$\boldsymbol{J}$	Current Density
σ	Electrical Conductivity
ε	Permittivity
μ	Permeability
ω	Angular Frequency
f	Ordinary Frequency
V	Voltage
I	Current
L	Inductance
C	Capacitance
ρ_m	Mass Density
c_p	Specific Heat Capacity
T	Temperature
k_{th}	Thermal Conductivity
Q_{VS}	Volume Heat Source

List of Symbols (Cont.)

Symbol	Physical Quantity
q_e	Electron Charge
m_e	Electron Mass
n_e	Electron Concentration
$\boldsymbol{p}$	Momentum
ω_p	Plasma Frequency
ν_c	Collision Frequency

List of Abbreviations

Abbreviation	Meaning
TLM	Transmission-line Modelling
UTLM	Unstructured TLM
CFL	Courant-Friedrichs-Lewy
FDTD	Finite-Difference Time-Domain
FEM	Finite Element Method
EM	Electromagnetic / Electromagnetics
EHD	Electrohydrodynamic / Electrohydrodynamics
MHD	Magnetohydrodynamic / Magnetohydrodynamics
CFRP	Carbon Fibre Reinforced Polymer
PDE	Partial Differential Equation
ODE	Ordinary Differential Equation
CVT	Centroidal Voronoi Tessellation
ODT	Optimal Delaunay Triangulation

Chapter 1

Introduction

The introduction to the thesis starts from explaining the motivation of the research topics covered in this work. Then, related existing research works about the electrothermal coupling, the plasma modelling and the lightning effects are reviewed. The organisation of this thesis is displayed as well.

1.1 Background and Motivation

Lightning strikes may cause severe damages to an aircraft, and the protection against lightning strikes is vitally important to make aircraft reliable and safe. The effects caused by lightning strikes include direct effects (e.g. shock wave generation and resistive heating) and secondary effects (e.g breakdown of electronic devices and even destruction of structural components) [1–4]. In terms of previous-generation aircraft, their external parts were made mainly of aluminium, which naturally provided considerable protections against the lightning strike because the high electrical and thermal conductivity of aluminium reduced and diffused the Joule heat, and the energy was mostly blocked outside the aircraft due to the Faraday shield effect. Recent years have witnessed an increasing use of composite materials in aircraft structures because of their higher strength, higher stiffness and lower weight [5], but the electrical and thermal conductivity of composite materials are far lower than those of aluminium, which increases the accumulated resistive heat when hit by lightning and also makes some vulnerable metallic parts of the outside aircraft (e.g.

fasteners) become highly potential attachment points of lightning strikes. Therefore, protection facilities such as conducting coatings [6, 7], metal meshes [8, 9] and segmented lightning diverter strips [10–13] are essential to support this new material technology. In terms of the radome part of the aircraft, segmented lightning diverter strips are preferred because they have fewer impacts on the antenna's characteristics [10, 11].

The conduction of electric currents through segmented lightning diverter strips requires the breakdown of the air-gaps between adjacent strips, and therefore, the numerical analysis on the protection performance of different segmented diverter designs usually involves the simulation of air plasma. In order to simulate plasma, both its electromagnetic and its thermal behaviour should be tracked because its multiphysical parameters are closely coupled with each other. Two-dimensional simulations are considered as it can reasonably capture representative physical behaviours during the breakdown of air and at the same time reduce the computational load compared with three-dimensional simulations.

The aim of this thesis was to develop a two-dimensional two-way electrothermal coupled numerical method to analyse plasma behaviours and the breakdown of air.

1.2 Review of Electrothermal Coupling Methods

1.2.1 Overview

Generally, electrothermal coupling methods are divided into one-way coupling methods and two-way coupling methods. One-way coupling means that the generated heat power calculated by the electromagnetic solver is fed into the thermal solver, giving temperature changes, while two-way coupling means that in addition to one-way coupling, the electromagnetic parameters and thermal parameters affected by the temperature are updated according to the results provided by the thermal solver, forming a closed loop.

1.2.2 One-way Electrothermal Coupling

For the modelling of microwave heating, the work presented in [14] was to simulate the microwave heating during the curing process of epoxy resin, where the finite element method with the variational formulation was used as the electromagnetic solver. The Joule heating power in the frequency domain was used there. One of the insightful points in [14] was that the three-dimensional magnetic field was simulated as its two-dimensional slice in the $r - z$ plane owing to its axisymmetric distribution around the z-axis, which significantly reduced the computational load. This is illustrated in Fig. 1.2.1.

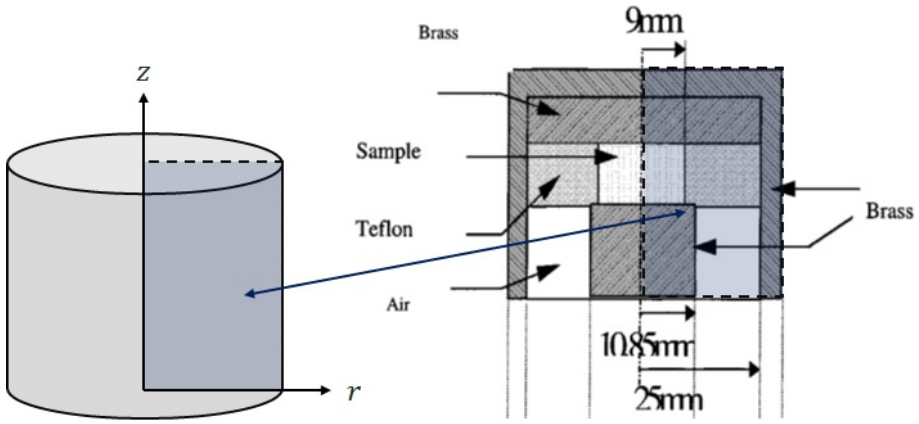

Fig. 1.2.1: The computational domain mentioned in [14]; figure modified.

The computational load can also be reduced by reshaping the computational domain. For example, in [15], where simple thermal circuits were used to model the heat diffusion around the microheater for semiconducting metal oxide gas sensors, a four-sector bow-ties shape was used to replace the rectangular membrane shape so that a two-dimensional simulation was reduced into one-dimension using the cylindrical coordinate system with only the radial dependence. However, the heat source in [15] was only set as a constant power input, and hence no electrothermal coupling was involved.

1.2.3 Two-way Electrothermal Coupling

In additional to [14], another microwave heating model was provided in [16] which used an explicit finite difference heat equation solver along with an explicit

finite-difference time-domain (FDTD) electromagnetic solver to simulate the heating process of the aluminium specimens placed in a cavity microwave furnace. The Joule heating effect was included in [16]; Newton's law of cooling and the Stefan-Boltzmann law were used to evaluate the advection and radiation heat flux. The permittivity and the electrical conductivity of 99.5% alumina were modelled as third-order polynomials against the temperature, while the thermal parameters were kept constant. Since this fully explicit scheme [16] was based on the finite difference method, its simulation time step was limited by the CFL condition which points out that the numerical domain of dependence must contain the physical domain of dependence [17].

A simulation platform for the design and evaluation of switching mode power supplies was developed in [18]. This platform was able to estimate the temperature distribution, and they chose an LED driver circuit as the example for demonstration. The computation part of this simulation platform was all based on commercial software. 'Saber' and 'Ansys' were used as the circuit simulator and the thermal simulator respectively, and their power dissipation and temperature output were passed to each other using 'Isight'. They claimed that their circuit performance parameters were functions of the temperature, although the specific functions of those parameters were not mentioned. One may be aware that the interaction between different software takes extra CPU time compared with using a single integrated multiphysics simulation software.

The work done in [19] also took commercial software as the whole computation part. This work focused on the temperature distribution around the bipolar junction transistors (BJTs) in integrated circuits. The circuit simulator and the thermal simulator were 'SPICE' and 'COMSOL' respectively, and they were connected via MATLAB codes. The interaction between SPICE and COMSOL is illustrated in Fig. 1.2.2. Two-way coupling was achieved, and particularly a nonlinear expression [19] for the thermal conductivity of silicon against the temperature was used.

Similar relations were also used in [20], where the electric field and the temperature conditions of high-voltage DC (HVDC) cable joints during their

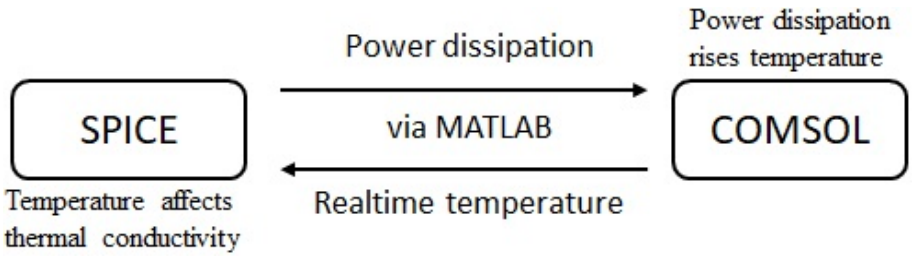

Fig. 1.2.2: Interaction between SPICE and COMSOL described in [19].

different working states were investigated using 'COMSOL' software. Although the thermal conductivities were fixed, the electrical conductivities of the cable and joint insulation materials were expressed using the product of one exponential function with respect to the temperature T and another exponential function with respect to the electric field strength E; the coefficients before the exponential functions and the coefficients in the exponents were obtained by fitting the experimental results [20]. Another way to couple the electrical resistivity/conductivity with the temperature is to use a linear electrical resistivity given in [21]. Two-way coupled simulation with this linear resistivity was used in [21] to investigate the temperature change of an induction heater working under the 50Hz mains power, and they also demonstrated the significance of using two-way coupling by comparing results from one-way coupled schemes and two-way coupled schemes. Apart from that, the thermal conductivity of iron was described by using tabulated equations in [21] because its change against varying temperatures was non-negligible but not easy to describe using explicit expressions. Tabulated equations are look-up tables of data obtained from physical experiments or theoretical calculations, with appropriate interpolation schemes if needed.

The linear electrical resistivity model was also used to calculate the Joule heating power in [22] which used the discontinuous Galerkin time-domain (DGTD) method to solve the electromagnetic waves propagating in a waveguide. Their following work [23] showed that in terms of parallel computing, the DGTD method had achieved much higher speedup ratio and parallel efficiency compared with the finite element time domain (FETD) method because of its domain decomposition scheme.

Back to tabulated parameter equations, in [24], where the temperature evolution of the zinc-oxide varistor core undergoing voltage and current pulses was simulated,

the electrical conductivity profile of the zinc-oxide under different temperatures and different electric field strengths was firstly measured using physical experiments, and then, linear and nonlinear regressions were used to produce a fitted function of the electrical conductivity against the temperature and the electric field strength. It helped especially in this case when the electrical conductivity of zinc-oxide varies significantly against the temperature and the electric field strength. The finite element method was used in [24] as the EM solver, and they suggested that implicit solvers should be used as the thermal solver because of the considerable non-linearity of the electrical conductivity. A related work was presented in [25], where the temperature distribution along the resistor stack of the pluggable voltage surge arrester was simulated. One of the insightful points in [25] was that they used a nonlinear equivalent thermal conductivity to cover all of the heat conduction, convection and radiation. The convection term was approximated using the Nusselt number (Nu) which is defined as the ratio of convective to conductive heat transfer across the fluid boundary. Note that strictly the convection in this definition includes the energy exchange due to both the mass transport (advection) and the heat conduction. The equivalent thermal conductivity for the radiation term was given in [26] as a function of the temperature. Both [24] and [25] took advantage of the axisymmetric layout of the computational domain to reduce a three-dimensional simulation into two-dimension as [14] did.

In addition to [15], the thermal circuit method was also used in the thermal solver of [27] to estimate the temperature of inverter chips in hybrid vehicles; this paper compared two thermal circuit layouts, namely the Foster network and the Cauer network, and the Foster network performed better in that case. A multi-step predictor–corrector style scheme was proposed and adopted in the coupling process. The Joule heating was calculated first by the electrical solver and then fed into the thermal solver. The temperature output at this step was fed back into the electrical solver to correct the device electrical parameters. The electrical solver then calculated the corrected Joule heating, and the thermal solver lastly produced the corrected temperature update. In terms of the thermal circuit construction, all

silicon chips were related to each other, and the thermal impedance network was expressed as a matrix in a compact form, which was similar to the case in [28].

1.2.4 TLM-Related Electrothermal Models

Since the transmission-line modelling (TLM) method is one of the main topics of this thesis, this section is designated for the existing works about the electrothermal modelling based on the TLM method. The TLM method has not been widely exploited in the area of coupled electrothermal modelling. The idea of TLM was adopted in [29] and [30], but it was used only as a finite element matrix solver instead of a complete EM solver; the equations and matrices were constructed in terms of finite elements with the magnetic vector potential as unknowns. The Joule heating power with the linear resistivity model was included in [30].

Three-dimensional thermal TLM schemes were used in [31, 32] to simulate the transient temperature change of power transistors. One of the insightful points in [31] was that the simulation time step was adjusted intelligently according to the real-time temperature profile to ensure the diffusive behaviour was more significant than the wave behaviour, which enabled the thermal TLM algorithm to jump large time step at slow-changing temperature periods for efficiency and to refine it in small time step at fast-changing periods for accuracy. However, these were only thermal simulations; constant input power was used as the heat source and no coupling was involved.

The thermal TLM method was also used in [33] to simulate the temperature in nanowires. This was a thermal simulation only, and it used only a one-dimensional thermal TLM scheme because the length-to-diameter ratio of nanowires was large. In addition to heat diffusion, the radiation effect was also considered via using the Stefan–Boltzmann law, and this radiation term was modelled as an extra conductance in the TLM equivalent circuit.

A two-way coupled true TLM method was used in [34] to investigate the ageing effects on radio frequency laterally diffused metal oxide semiconductor (RF LDMOS) transistors. Two-dimensional TLM methods based on shunt nodes were applied as

both the EM and the thermal solver, and the electrical parameters of the transistors depended on not only the temperature but also the physical time, reflecting ageing. The ambient temperature was also alternated to mimic the change of seasons. The investigations on the microwave heating effect were reported in [35] and [36], where both the EM TLM and the thermal TLM methods were also used. The Newton's law of cooling and the Stefan-Boltzmann law were employed in [35] to represent the heat convection and the heat radiation. Another two-way coupled TLM method was developed in [37], where the Joule heat generated in plasma materials was fed into the thermal TLM solver, and the plasma parameters used in the electromagnetic TLM solver were updated according to the temperature.

1.3 Review of Plasma Modelling Methods

1.3.1 Hydrodynamics Based Models

Hydrodynamic based models involving electrothermal coupling include electrohydrodynamic (EHD) models and magnetohydrodynamic (MHD) models. The EHD model was used in [38] to simulate the temperature distribution in moving coolant (dielectric liquid) driven by an external electric field, and it was also used in [39] to analyse the surface breakdown process when a high voltage was injected onto the interface between the dielectric liquid and the solid insulator plate through a needle tip. The effect of the magnetic field $\boldsymbol{B}$ was not considered in these EHD models.

In terms of MHD models, the behaviour of the electric arc attached to substrates made of different materials, namely two resistive composites and one metal, was investigated in [40]. The MHD model was also used to compare with physical experimental results. In [41], physical experiments were conducted first. An electrode was placed above the composite plate, and a high current released from a capacitor was injected towards the plate through the electrode to excite the air plasma. Based on this physical experimental layout, they simulated the plasma evolution using a three-dimensional MHD model. The temperature

profile was recorded, and two-way coupling was achieved in [41] by using a temperature-dependent resistivity. In addition to [41], the electromagnetic boundary conditions for MHD models are explained in detail in [42]. Also, [41] could have taken use of the axisymmetry to achieve the dimensional reduction.

As hydrodynamic models, both EHD and MHD maintain the fluid behaviour including the pressure information, and the Joule heating term is naturally covered in the energy transport equation. These are helpful to the plasma modelling related to our work, but simplifications on Maxwell's equations are usually made [41, 43], and either or both of the magnetic field $\boldsymbol{B}$ and the electric field $\boldsymbol{E}$ in those EHD and MHD models were calculated using the magnetostatic and electrostatic Poisson's equations, which might not describe a fully time-varying electromagnetic field. Also, plasma is a dispersive medium; its permittivity, hence its conductivity, depends not only on the temperature but also on the wave frequency. Although EHD and especially MHD models are popular to describe the plasma, the dispersive property of plasma is not clearly modelled because the permittivity in those EHD and MHD models mentioned were treated as constant. Furthermore, in the simulation of lightning-excited plasma, which is related to the applications of our work, a specific channel area was pre-heated (to 10000 K in [40], to 1000 K in [41]) as an initial condition to initiate the plasma flow. This was a pre-defined plasma channel, and this assumption could be avoided if using electrodynamics solvers.

1.3.2 The Drude Model of Plasma

The Drude model [37, 44–47] is another approach to describe the plasma characteristics. In the Drude model, the permittivity is defined as

$$\varepsilon(\omega) = \varepsilon_0 \left(1 + \frac{\omega_p^2}{\omega(j\nu_c - \omega)}\right), \tag{1.3.1}$$

where ω_p is the plasma frequency [48], and ν_c is the electron-ion collision frequency. Detailed theory about the Drude model will be explained in Chapter 6.

The Drude model of plasma can be implemented in the Finite-Difference Time-Domain (FDTD) method [45, 47] or the Transmission-Line Modelling (TLM)

method [37, 46], enabling the full electrodynamics of plasma to be maintained. A two-way coupled numerical scheme for plasma simulation based on the Drude model was presented in [37], where the Cartesian TLM method was applied to both EM and thermal diffusion problems. Although the advection of plasma was not considered in those Drude-model-based schemes, the plasma arc channel did not need to be pre-defined on account of full electrodynamics. One also needs to be aware that the permittivity, hence the conductivity, of plasma depends on not only the temperature but also the EM wave frequency, which is not easy to be considered in MHD-based schemes.

Since the Drude model is expressed in the frequency domain and the TLM method is a time-domain method, z-transforms and digital filters were used in [37, 46] to bring the frequency domain relationship of plasma permittivity into the time domain. New TLM update formula based on the Drude model and digital filtering was derived [37], but this derivation was based on the normalisation of the space length. This normalisation is useful when dealing with structured and uniform computational grids, but if the grid is not uniform, the normalisation of space length will no longer hold.

1.4 Review of Lightning Effects Investigations

Coupled electrothermal modelling methods have been used in the research on the lightning effects and the lightning protections of modern aircraft with carbon fibre reinforced polymer (CFRP) materials. Physical experiments and numerical simulations were completed in [43] to investigate the lightning direct effects around the fasteners inserted in a piece of CFRP aircraft skin. Both experiments and simulations used an indirect electrode, which consisted of a tungsten rod ending with an insulator sphere, placed above the test CFRP samples to model the lightning injection. The MHD model was used in their simulation.

Another simulation work was provided in [49], where also an indirect electrode was placed above the CFRP sample. The $k - \varepsilon$ model of turbulent flow was added into their MHD governing equations, and the air in room temperature was

described by using the cold-field electron emission model so that no pre-heating was needed at the electrode boundary. Both the EM equations and the hydrodynamic equations were solved using the finite element method. Despite the advantage that using indirect electrodes could avoid unnatural damages on the test samples [43] during physical experiments, it was argued in [50] that a direct electrode without the insulator sphere should be used in associated experiments because the indirect electrode could cause metal vapour generated during the ignition, which changed the hydrodynamics around the electric arc.

In addition, an explicit FDTD scheme was used in [51]. To represent the anisotropic property of the CFRP material, the permittivity, the electrical conductivity and the thermal conductivity were all expressed as tensors, and hence, their FDTD formulation was derived based on tensors. Similar tensor FDTD formulation was also introduced in [52], where an implicit scheme was used together to solve the thermal diffusion equation, and only one-way coupling with Joule heating effect was considered in terms of electrothermal coupling.

A two-way coupled model for plasma simulation was proposed in [37]; it was applied to analyse the breakdown process of the air-gaps between segmented lightning diverter strips, and the breakdown sequence of the air-gaps in a row was observed. The shape of the diverter buttons was chosen to be square only, and buttons with other different shapes could have been investigated.

1.5 Organisation of the Thesis

This thesis is organised as follows.

In Chapter 2, the classic Cartesian electromagnetic (EM) TLM methods are introduced and derived from first principles based on the derivative form of Maxwell's equations; The details on the usage of link/stub models are covered, and the scattering and connection process is explained step by step.

In Chapter 3, the Cartesian thermal TLM method is introduced and derived, showing the capability of TLM methods to solve thermal diffusion equations by taking the diffusion process as low-frequency waves propagating in highly lossy

media.

In Chapter 4, applications of the TLM methods are extended from structured Cartesian grids to unstructured triangular grids. The triangulation mesh used by unstructured TLM (UTLM) methods is firstly introduced, building the bridge from Cartesian TLM methods to unstructured TLM methods, and the mesh generation algorithm is briefly covered. Then, the existing EM UTLM method using shunt nodes is derived in an alternative way, and next, the new EM UTLM method using series nodes is proposed. The mesh optimisation techniques for UTLM methods are also explained and tested.

In Chapter 5, the UTLM method for thermal diffusion problems is proposed; the thermal UTLM method uses the same triangular mesh as the EM UTLM method so that it is ideally suitable for electrothermal coupled simulations.

Chapter 6 first briefly covers the physics of plasma and the Drude plasma model, and then the Drude plasma model is implemented in both Cartesian grids and triangular grids. New update formulae (digital filters) for unstructured triangular grids are derived to reflect the frequency-dependent permittivity of the plasma and to evaluate the Joule heating power density generated by the plasma.

Chapter 7 proposes the two-way coupled electrothermal model of plasma using the EM UTLM, the thermal UTLM and the Drude plasma model; its applications on the analyses of different segmented lightning diverter strips designs are covered as well.

Lastly, Chapter 8 summarises the author's work and puts forward some potential future advancements.

Chapter 2

Cartesian EM TLM Method

This chapter starts with a quick review of popular Maxwell's equations solvers. Then, the transmission-line modelling (TLM) methods in Cartesian grids are derived from first principles by mapping Maxwell's equations to the transmission-line equations. The one-dimensional TLM method, the two-dimensional transverse magnetic TLM method and the two-dimensional transverse electric TLM method are covered respectively with step-by-step explanations on the scattering and connection process.

2.1 Overview

The numerical simulation of electromagnetic waves requires the numerical solution to Maxwell's equations:

$$\nabla \cdot \boldsymbol{E} = \frac{\rho}{\varepsilon}, \qquad (2.1.1) \qquad\qquad \nabla \cdot \boldsymbol{B} = 0, \qquad (2.1.2)$$

$$\nabla \times \boldsymbol{E} = -\frac{\partial \boldsymbol{B}}{\partial t}, \qquad (2.1.3) \qquad\qquad \nabla \times \boldsymbol{B} = \mu \boldsymbol{J} + \mu\varepsilon \frac{\partial \boldsymbol{E}}{\partial t}, \qquad (2.1.4)$$

where $\boldsymbol{E}$ is the electric field strength, ρ is the charge density, $\boldsymbol{B}$ is the magnetic flux density, $\boldsymbol{J}$ is the electric current density.

Popular categories of electromagnetic solvers include the finite difference time domain (FDTD) method, the finite element method (FEM) and the

transmission-line modelling (TLM) method.

The FDTD method is based on the direct discretisation of Maxwell's equations in terms of both time and space, and different finite difference approximations of partial derivatives yield different specific FDTD schemes. The electric field and the magnetic field are sampled in different positions in both space and time; they have an offset of a half space step ($\Delta s/2$) and a half time step ($\Delta t/2$) [53, 54]. The electric field and the magnetic field are then updated alternately, and this common characteristic of FDTD schemes is described as 'leap-frog'. FDTD methods can be either implicit or explicit. Implicit FDTD methods require matrix solving, whereas explicit FDTD methods has a maximum time step limited by the CFL condition which essentially points out that the numerical domain of dependence should cover the physical domain of dependence [54].

The FEM can be derived through either the weighted residual approach or the variational approach [54, 55]. Both of them ultimately give a linear system of variables to optimise (minimise), hence a linear system of equations to solve. Most of the FEM applications are in the frequency domain, although the time-domain FEM exists, where usually the approximated electric field $\boldsymbol{E}$ is expressed using sampling points in computational cells and then substituted into the second-order curl-curl equation for $\boldsymbol{E}$:

$$\frac{1}{\mu}\nabla \times (\nabla \times \boldsymbol{E}) + \varepsilon \frac{\partial^2}{\partial t^2}\boldsymbol{E} + \sigma \frac{\partial}{\partial t}\boldsymbol{E} = 0 \tag{2.1.5}$$

so that this PDE (2.1.5) can be turned into a second-order ODE. Especially, if the square or cubic elements are used with sample points at the centre of each edge, the time-domain FEM reduces to the FDTD method [54].

The transmission-line modelling (TLM) method, as another popular method to numerically solve Maxwell's equations, is one of the main topics of this thesis. The TLM method is based on the electric circuit model of the transmission line. It uses a group of lumped electrical components (L, C, R and G) to model the electromagnetic behaviour of a short segment of the transmission line, and the whole transmission line is then modelled as multiple groups of lumped electrical components; therefore, this model is also known as the distributed-element model [56]. Similar to the

FDTD method, the TLM method is a time-domain method, but instead of solving the Maxwell's PDEs directly, it solves electric circuit models with governing PDEs of the same structure as Maxwell's PDEs. Usually, a local part of the circuit can be solved by representing the rest part of the circuit using their Thévenin equivalent circuits. In this way, the whole PDE system can be decoupled so that large matrix solving is avoided while the unconditional stability is still maintained as long as the electrical component parameters are physical, which is a representative advantage of the TLM method.

2.2 One-dimensional TLM

2.2.1 Model Derivation

From this section, we start to introduce how the TLM method is applied to solve the electromagnetic waves, or essentially, Maxwell's equations. The one-dimensional version is described first. If we consider an electromagnetic wave with only E_x and H_y components propagating in the z-direction, the Faraday's law (2.1.3) and the Ampere's law (2.1.4) in Cartesian coordinates becomes

$$\frac{\partial E_x}{\partial z} = -\mu \frac{\partial H_y}{\partial t} \tag{2.2.1}$$

and

$$\frac{\partial H_y}{\partial z} = -\varepsilon \frac{\partial E_x}{\partial t} \tag{2.2.2}$$

respectively.

Then, we consider a one-dimensional transmission line segment shown in Fig. 2.2.1.

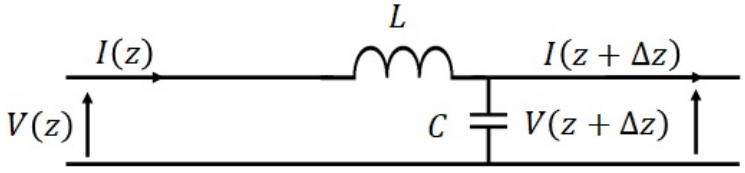

Fig. 2.2.1: A single 1D TLM node

If we use the first-order Taylor expansion to approximate the voltage $V(z)$ and

the current $I(z)$, the circuit shown in Fig. 2.2.1 can be described using

$$\Delta V = V(z+\Delta z) - V(z) = \Delta z \frac{\partial V}{\partial z} = -L\frac{\partial I}{\partial t}, \tag{2.2.3}$$

$$\Delta I = I(z+\Delta z) - I(z) = \Delta z \frac{\partial I}{\partial z} = -C\frac{\partial V}{\partial t}. \tag{2.2.4}$$

One may find that (2.2.3) and (2.2.1) have similar structures; so do (2.2.4) and (2.2.2). If we make the mapping $V \leftrightarrow E_x\Delta z$ and $I \leftrightarrow H_y\Delta z$, the inductance L and the capacitance C are then evaluated, given as

$$L = \mu\Delta z, \tag{2.2.5}$$

$$C = \varepsilon\Delta z. \tag{2.2.6}$$

These two expressions indicates that in TLM methods, the permeability is modelled as the inductance per unit length, and the permittivity is modelled as the capacitance per unit length. This concept helps the reader understand various TLM methods, and it is usually the case for Cartesian TLM, but for unstructured TLM, this pattern may be slightly changed.

2.2.2 Link Model and Stub Model

The TLM method is based on the solution to the transmission-line circuit. In each iteration, the TLM method evolves the circuit state by a certain time step Δt. This is not through discretising the time partial derivative mathematically but through associating Δt with the characteristic impedance of inductors and capacitors. Two models, namely the `link model` and the `stub model`, can be used to represent an inductor or a capacitor [57]. The relations between the electrical components and their characteristic impedance are listed in Table 2.2.1 according to [57]. Each capacitor model leads to an error inductance, and each inductor model leads to an error capacitance.

One may need to be aware that the term Δt is the single trip time for links but the round trip time for stubs; usually, the single trip time is half of the round trip time.

Table 2.2.1: Characteristic impedance and associated error term

Model	Characteristic Impedance	Error
Link Capacitor	$Z_C = \Delta t/C$	$L_e = (\Delta t)^2/C$
Link Inductor	$Z_L = L/\Delta t$	$C_e = (\Delta t)^2/L$
Stub Capacitor	$Z_C = \Delta t/(2C)$	$L_e = (\Delta t)^2/(4C)$
Stub Inductor	$Z_L = (2L)/\Delta t$	$C_e = (\Delta t)^2/(4L)$

2.2.3 Scattering and Connection

The local voltages are updated by solving the local transmission-line circuit and representing the rest of the transmission-line using their Thévenin equivalent circuits. If the incident voltage V^i comes with a characteristic input impedance Z (illustrated in Fig. 2.2.2a), the Thévenin equivalent circuit will be a voltage source of $2V^i$, which is the open circuit voltage of the input voltage source, in series with an internal impedance Z (illustrated in Fig. 2.2.2b).

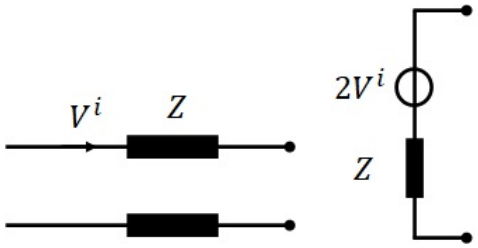

Fig. 2.2.2: (a) One segment of the transmission line and (b) its Thévenin equivalent circuit. Solid dots at the right side are the terminals under investigation.

The Thévenin equivalent circuits that need to be solved in the TLM methods are linear and usually not too complicated, and the solution to the circuits can be obtained as explicit expressions. If we consider two adjacent 1D TLM nodes shown in Fig. 2.2.1, the transmission-line circuit is illustrated in Fig. 2.2.3a, and if we model inductors using links and model capacitors using stubs, the TLM circuit becomes Fig. 2.2.3b.

The link impedance Z in Fig. 2.2.3b is calculated directly using $Z = L/\Delta t$ as is listed in Table 2.2.1, but the stubs impedance is calculated after evaluating the stub capacitance $C_s = C - C_e$ which is the original capacitance in the model subtracted by the error capacitance of the link inductor. This can reduce the error caused by the

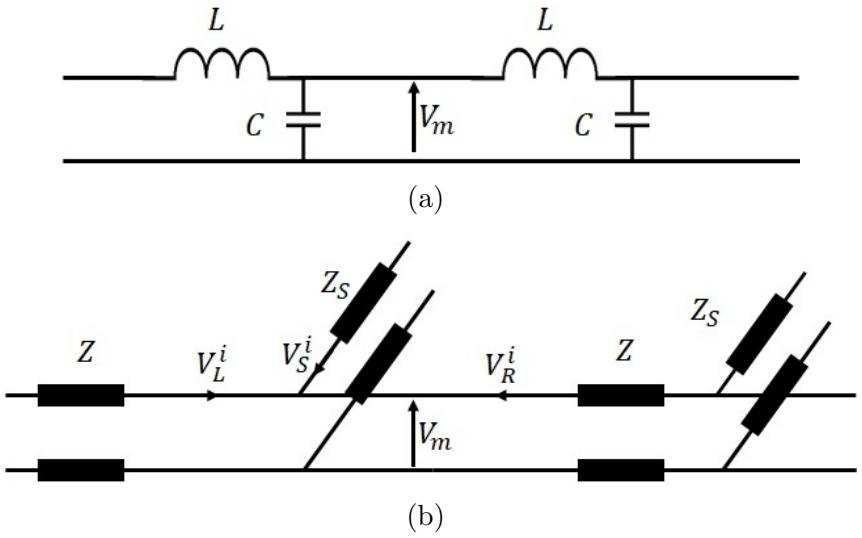

Fig. 2.2.3: (a) Two adjacent 1D TLM nodes, where (b) inductors modelled using links and capacitors modelled using stubs. Subscripts $_L$ and $_R$ stand for the left and the right side link respectively, and the subscript $_s$ stands for the stub. V^i means the incident voltage, and V_m is the voltage at the port interface.

link models in TLM methods. Considering (2.2.5), (2.2.6) and the error capacitance defined in Table 2.2.1, the stub capacitance is obtained as

$$C_s = \varepsilon \Delta z - \frac{\Delta t^2}{\mu \Delta z}, \tag{2.2.7}$$

and then the stubs capacitance is calculated using $Z_s = \Delta t/(2C_s)$ as is listed in Table 2.2.1. The Thévenin equivalent circuit of Fig. 2.2.3b is shown in Fig. 2.2.4 based on the concept illustrated in Fig. 2.2.2. Note that the right-most stub in Fig. 2.2.3b is not involved in the Thévenin circuit; this decouples the whole transmission-line circuit into local parts when we analyse a specific port so that solving large linear systems of equations is avoided, which is one of the main advantages of TLM methods. Applying nodal voltage analysis gives the middle voltage at the port as

$$V_m = \frac{2\left(\dfrac{V_L^i}{Z} + \dfrac{V_R^i}{Z} + \dfrac{V_s^i}{Z_s}\right)}{\dfrac{2}{Z} + \dfrac{1}{Z_s}}. \tag{2.2.8}$$

If the medium under investigation is vacuum and uniform, and the simulation time step is chosen as $\Delta t = \Delta z/c_0$, where c_0 is the speed of light in vacuum, then C_s vanishes (Z_s is infinity), giving the same circuits and equations that are introduced

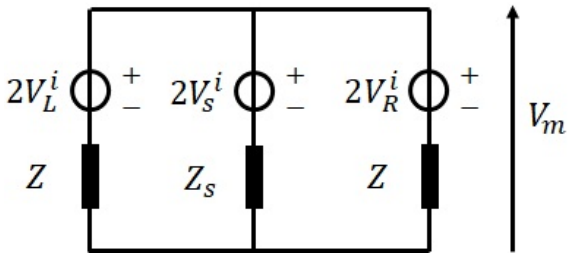

Fig. 2.2.4: Thévenin equivalent circuit at the port between two 1D TLM nodes

in [57].

Once the nodal voltages V_m are obtained, the reflected voltages V^r are calculated as

$$V_L^r = V_m - V_L^i, \tag{2.2.9}$$

$$V_R^r = V_m - V_R^i, \tag{2.2.10}$$

$$V_s^r = V_m - V_s^i. \tag{2.2.11}$$

This process is known as `scattering`, especially the scattering at the port in this context. When the scattering is completed, the reflected voltage of the present time step (denoted as $V^r[n]$) at every node is treated as the incident voltage of the next time step (denoted as $V^i[n+1]$) into its adjacent nodes. This process is known as `connection`, specifically the connection along link lines. For stubs, the connection process is within themselves, and a capacitive stub gets its next incident voltage from its present reflected voltage itself, denoted as

$$V_s^i[n+1] = V_s^r[n]. \tag{2.2.12}$$

By alternating between the scattering and connection process, the circuit state is evolved.

2.3 Two-dimensional Shunt Model

2.3.1 Model Derivation

Although electromagnetic waves are three-dimensional phenomena in nature, two-dimensional simulations are useful in many cases such as the investigations on some particular propagation modes or the surface plasmon behaviours involved in this thesis. A two-dimensional simulation generally takes less CPU time; even if at the end, a three-dimensional simulation is required, the two-dimensional simulation can sill contribute to the understanding of the target problem from its own point of view.

The two-dimensional shunt model is designed to simulate the transverse magnetic (TM) modes of the wave propagation. The magnetic field is assumed to have only H_x and H_y components, and the electric field is assumed to have only E_z component. The EM wave propagates in the $x-y$ plane, and no variation is assumed in the z-direction ($\partial/\partial z = 0$). A single 2D shunt node is shown in Fig. 2.3.1.

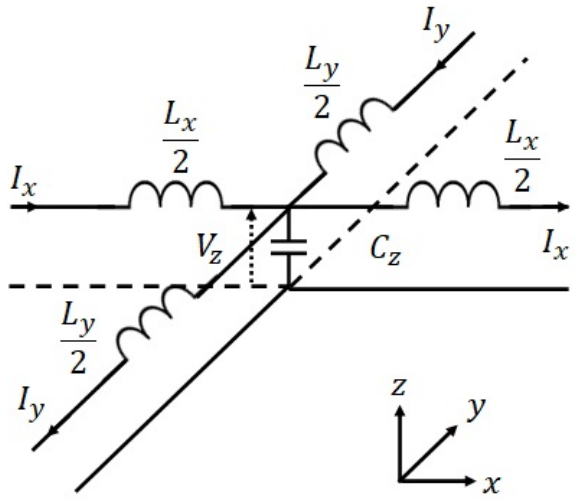

Fig. 2.3.1: A single 2D shunt Cartesian TLM node

In the case of transverse magnetic modes, the Maxwell's curl equations become (2.3.1) (2.3.2) (2.3.3) in Cartesian coordinates.

$$\frac{\partial H_y}{\partial x} - \frac{\partial H_x}{\partial y} = \varepsilon \frac{\partial E_z}{\partial t} \tag{2.3.1}$$

$$\frac{\partial E_z}{\partial x} = \mu \frac{\partial H_y}{\partial t} \tag{2.3.2}$$

$$\frac{\partial E_z}{\partial y} = -\mu \frac{\partial H_x}{\partial t} \tag{2.3.3}$$

Multiplying both sides of (2.3.1) by $\Delta x \Delta y$ yields

$$\frac{\partial H_y}{\partial x}\Delta_x \Delta y - \frac{\partial H_x}{\partial y}\Delta_x \Delta y = \varepsilon \frac{\partial E_z}{\partial t}\Delta_x \Delta y. \tag{2.3.4}$$

If we make the equivalences $I_x \leftrightarrow H_y \Delta y$, $I_y \leftrightarrow H_x \Delta x$ and $V_z \leftrightarrow E_z \Delta z$, (2.3.4) becomes

$$\frac{\partial I_x}{\partial x}\Delta_x - \frac{\partial I_y}{\partial y}\Delta y = \varepsilon \frac{\Delta_x \Delta y}{\Delta z}\frac{\partial V_z}{\partial t}. \tag{2.3.5}$$

If we use the first-order approximation of ΔI_x and ΔI_y, then the LHS of (2.3.5) is the net current flowing out of the capacitor C_z in Fig. 2.3.1, denoted as $-\Delta I$. According to $-\Delta I = C \cdot dV/dt$, the analogous capacitance C_z is expressed as

$$C_z = \varepsilon \frac{\Delta_x \Delta y}{\Delta z}. \tag{2.3.6}$$

Note that since C_z is shared between two 1D transmission lines in the x-direction and the y-direction respectively, the equivalent capacitance for each transmission line should be half of C_z.

To evaluate the analogous inductance, two adjacent shunt nodes should be considered together. Fig. 2.3.2 shows two shunt nodes connected in the x-direction, and the y-direction components are omitted for now.

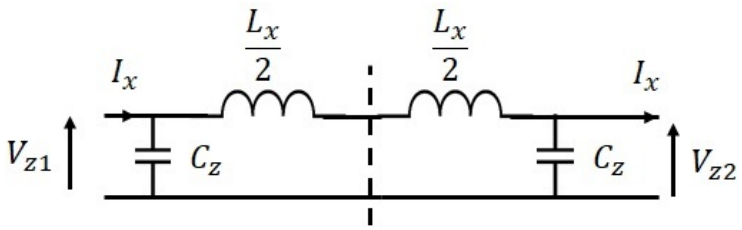

Fig. 2.3.2: Two adjacent shunt nodes in the x-direction

Multiplying both sides of (2.3.2) by Δx and using the same equivalences ($I_x \leftrightarrow H_y \Delta y$ and $V_z \leftrightarrow E_z \Delta z$) yield

$$\frac{\partial V_z}{\partial x}\Delta x = \mu \frac{\Delta x \Delta z}{\Delta y}\frac{\partial I_x}{\partial t}. \tag{2.3.7}$$

It is seen that the LHS of (2.3.7) is the first-order approximation of the voltage change across the inductor L_x, denoted as $-\Delta V$. According to $-\Delta V = L \cdot dI/dt$, the analogous inductance L_x is expressed a

$$L_x = \mu \frac{\Delta x \Delta z}{\Delta y}. \tag{2.3.8}$$

The analogous inductance in the y-direction can be derived as (2.3.9) in a similar way from (2.3.3), leading to

$$L_y = \mu \frac{\Delta y \Delta z}{\Delta x}. \tag{2.3.9}$$

2.3.2 Scattering and Connection

The scattering and connection process in 2D TLM methods contains the process at the node centre and the process at the port. We still use links to model inductors and stubs to model capacitors. After doing this, the shunt node becomes Fig. 2.3.3a at the node centre. Similar to the 1D case, the stub impedance is still calculated using the stub capacitance $C_s = C - C_e$. Considering (2.3.6), (2.3.8), (2.3.9), and Table 2.2.1, we obtain

$$C_s = \varepsilon \Delta l - \frac{(\Delta t/2)^2}{\mu \Delta l/2} \times 4 = \varepsilon \Delta l - \frac{2\Delta t^2}{\mu \Delta l}, \tag{2.3.10}$$

where $\Delta l = \Delta x = \Delta y = \Delta z$ is assumed to keep the convention used in [57]. There are several points to mention about the calculation of C_s. Firstly, the inductance of a single transmission line branch is $L_x/2$ and $L_y/2$ instead of L_x and L_y; secondly, Δt refers to the simulation time step covering the scattering and connection process at both node centres and ports, and the single trip time on a single link is $\Delta t/2$; third, the error capacitance of all four branches should be deducted from the original central capacitance; fourth, when evaluating the characteristic impedance of the stub capacitor, the round trip time is Δt. The stub impedance is calculated as

$$Z_s = \frac{\Delta t}{2C_s}, \tag{2.3.11}$$

and the link impedance is calculated as

$$Z_1 = Z_3 = \frac{L_y/2}{\Delta t/2} = \mu\frac{\Delta y \Delta z}{\Delta x \Delta t} = \frac{\mu \Delta l}{\Delta t}, \tag{2.3.12}$$

$$Z_2 = Z_4 = \frac{L_x/2}{\Delta t/2} = \mu\frac{\Delta x \Delta z}{\Delta y \Delta t} = \frac{\mu \Delta l}{\Delta t}, \tag{2.3.13}$$

where $\Delta l = \Delta x = \Delta y = \Delta z$ is assumed to still keep the convention used in [57].

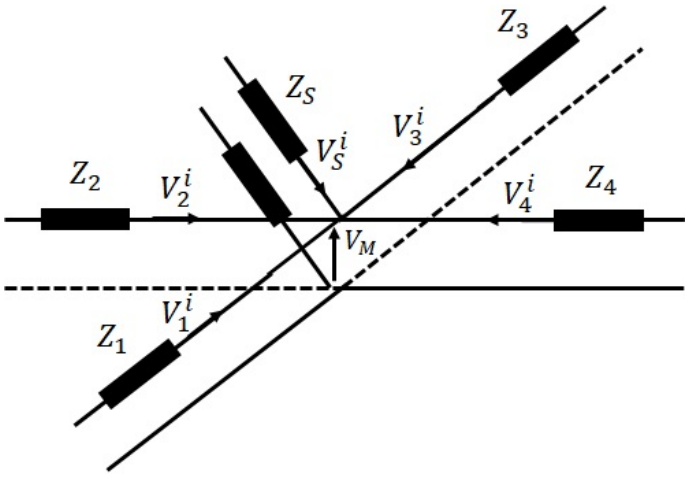

(a)

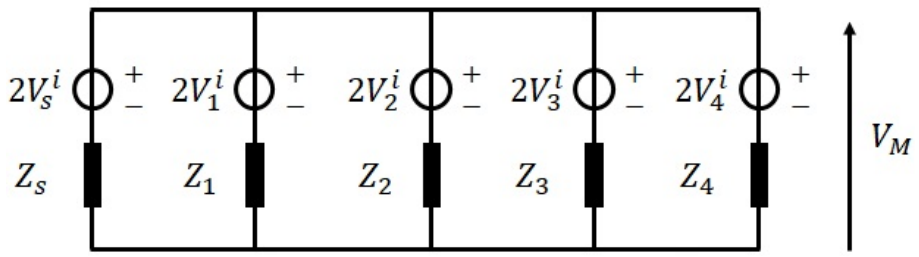

(b)

Fig. 2.3.3: (a) A 2D shunt Cartesian TLM node with inductors modelled using links and capacitors modelled using stubs; (b) the Thévenin equivalent circuit at the node centre.

The Thévenin equivalent circuit at the node centre is shown in Fig. 2.3.3b. Applying nodal voltage analysis gives the middle voltage V_M at the node centre:

$$V_M = \frac{2\left(\frac{V_1^i}{Z_1} + \frac{V_2^i}{Z_2} + \frac{V_3^i}{Z_3} + \frac{V_4^i}{Z_4} + \frac{V_s^i}{Z_s}\right)}{\frac{1}{Z_1} + \frac{1}{Z_2} + \frac{1}{Z_3} + \frac{1}{Z_4} + \frac{1}{Z_s}}. \tag{2.3.14}$$

If the medium under investigation is vacuum and uniform, the simulation time

step to give zero central stub capacitance is found using (2.3.10) as

$$\Delta t = \frac{\Delta l}{\sqrt{2}c_0}, \tag{2.3.15}$$

where $c_0 = 1/\sqrt{\mu_0 \varepsilon_0}$ is the speed of light in vacuum. In this case, if $Z = Z_1 = Z_2 = Z_3 = Z_4$ which is the link characteristic impedance in uniform Cartesian grids is also assumed, the expression of the middle voltage at the node centre V_M is simplified to be

$$V_M = 0.5\left(V_1^i + V_2^i + V_3^i + V_4^i\right), \tag{2.3.16}$$

which is the same as the expression given on page 94 of [57].

The reflected voltages are calculated as

$$V_1^r = V_M - V_1^i, \tag{2.3.17}$$

$$V_2^r = V_M - V_2^i, \tag{2.3.18}$$

$$V_3^r = V_M - V_3^i, \tag{2.3.19}$$

$$V_4^r = V_M - V_4^i, \tag{2.3.20}$$

$$V_s^r = V_M - V_s^i. \tag{2.3.21}$$

At the port connecting two links from adjacent nodes (e.g. Fig. 2.3.2), the Thévenin equivalent circuit can be described using Fig. 2.3.4, where subscripts $_L$ and $_R$ stand for the left and the right side without loss of generality, and V_N is the middle voltage at the port. The impedance Z_L and Z_R are calculated according to the left-side node and the right-side node respectively.

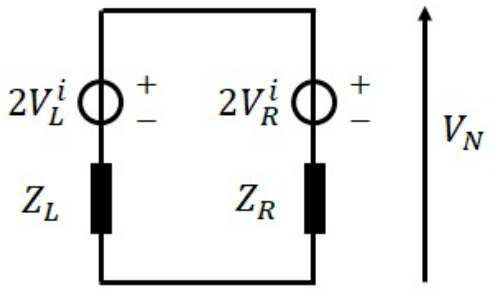

Fig. 2.3.4: Thévenin equivalent circuit at the port

Applying nodal voltage analysis gives

$$V_N = \frac{2\left(\frac{V_L^i}{Z_L} + \frac{V_R^i}{Z_R}\right)}{\frac{1}{Z_L} + \frac{1}{Z_R}}, \tag{2.3.22}$$

and the reflected voltages are

$$V_L^r = V_N - V_L^i, \tag{2.3.23}$$

$$V_R^r = V_N - V_R^i. \tag{2.3.24}$$

In terms of the connection process, the reflected voltages from the ports become the incident voltages towards the node centres, and the reflected voltages from the node centres become the incident voltages towards the ports. The reflected voltage itself of the capacitive stub becomes the incident voltage of the stub in the next iteration.

2.4 Two-dimensional Series Model

2.4.1 Model Derivation

A different model, the two-dimensional series model, is designed to simulate the transverse electric (TE) modes of the wave propagation. In this case, the electric field is assumed to have only E_x and E_y components, and the magnetic field is assumed to have only H_z component. No variation is assumed in the z-direction ($\partial/\partial z = 0$). Fig. 2.4.1 shows a 2D series node.

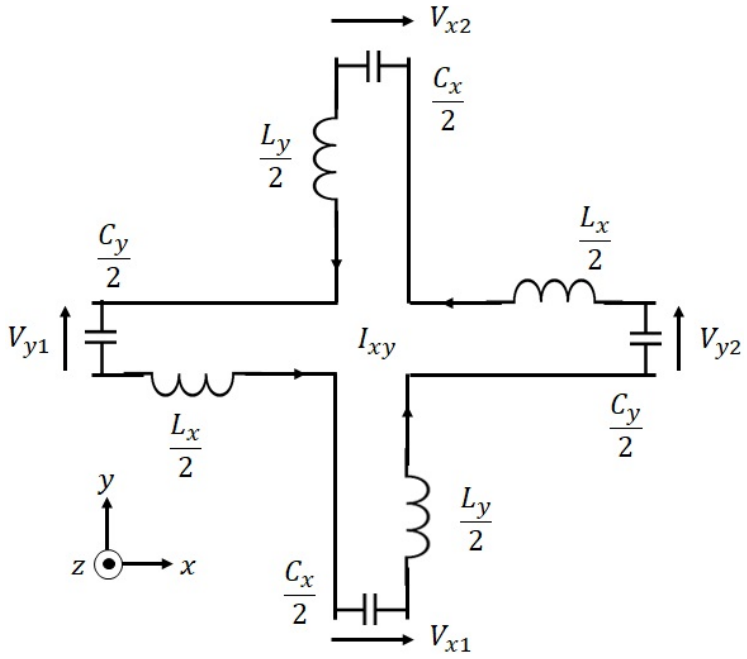

Fig. 2.4.1: A single 2D series Cartesian TLM node

The Maxwell's curl equations in TE modes are reduced to (2.4.1) (2.4.2) and (2.4.3) in Cartesian coordinates.

$$\frac{\partial E_y}{\partial x} - \frac{\partial E_x}{\partial y} = -\mu \frac{H_z}{\partial t} \tag{2.4.1}$$

$$\frac{\partial H_z}{\partial y} = \varepsilon \frac{\partial E_x}{\partial t} \tag{2.4.2}$$

$$-\frac{\partial H_z}{\partial x} = \varepsilon \frac{\partial E_y}{\partial t} \tag{2.4.3}$$

Multiplying both sides of (2.4.1) by $\Delta x \Delta y$ gives

$$\frac{\partial E_y}{\partial x}\Delta x\Delta y - \frac{\partial E_x}{\partial y}\Delta x\Delta y = -\mu\frac{H_z}{\partial t}\Delta x\Delta y. \tag{2.4.4}$$

If the equivalence $I_{xy} \leftrightarrow H_z\Delta z$, $V_x \leftrightarrow E_x\Delta x$ and $V_y \leftrightarrow E_y\Delta y$ are used, (2.4.4) becomes

$$\frac{\partial V_y}{\partial x}\Delta x - \frac{\partial V_x}{\partial y}\Delta y = -\mu\frac{\Delta x\Delta y}{\Delta z}\frac{I_{xy}}{\partial t}. \tag{2.4.5}$$

If the first-order approximations are used, then the LHS of (2.4.5) is the total change of the voltage along the mesh current I_{xy}. According to $\Delta V = -L \cdot dI/dt$, the analogous inductance L_{xy} is obtained as

$$L_{xy} = \frac{1}{2}\mu\Delta l, \tag{2.4.6}$$

where $L_x = L_y = L_{xy}$ and $\Delta x = \Delta y = \Delta z = \Delta l$ is assumed.

Next, two adjacent series nodes in the x-direction are considered together to evaluate C_y. Fig. 2.4.2 shows the joint in the x-direction of two series nodes. Multiplying both sides of (2.4.3) by Δx and using the same equivalence ($I_{xy} = H_z\Delta z$

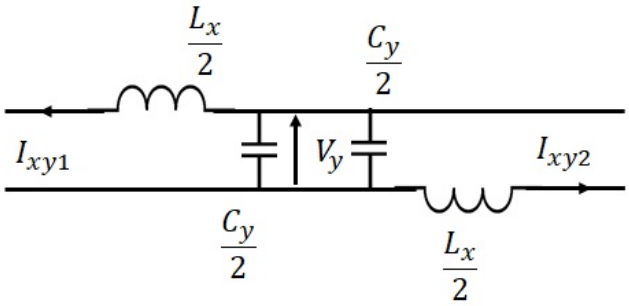

Fig. 2.4.2: Two adjacent series nodes in the x-direction

and $V_y = E_y\Delta y$) yields

$$\frac{\partial I_{xy}}{\partial x}\Delta x = -\varepsilon\frac{\Delta x\Delta z}{\Delta y}\frac{\partial V_y}{\partial t}. \tag{2.4.7}$$

According to $\Delta I = -C \cdot dV/dt$, the analogous capacitance facing the y-direction C_y is expressed as (2.4.8), and the analogous capacitance facing the x-direction C_x (2.4.9) can be obtained in the same way, where $\Delta x = \Delta y = \Delta z = \Delta l$ is assumed.

$$C_y = \varepsilon\Delta l \tag{2.4.8}$$

$$C_x = \varepsilon\Delta l \tag{2.4.9}$$

2.4.2 Scattering and Connection

The scattering and connection process for the TE series model is similar to that for the TM shunt model. Both of them contain the process at the node centre and the process at the port, but different circuit models lead to different Thévenin equivalent circuits to solve. We still use links to model inductors and stubs to model capacitors, and the Thévenin equivalent circuit at the node centre is demonstrated in Fig. 2.4.3, where I is the loop current within this node, and the impedance is calculated as

$$Z_1 = Z_2 = Z_3 = Z_4 = \frac{L_{xy}/2}{\Delta t/2} = \frac{1}{2}\frac{\mu \Delta l}{\Delta t} \tag{2.4.10}$$

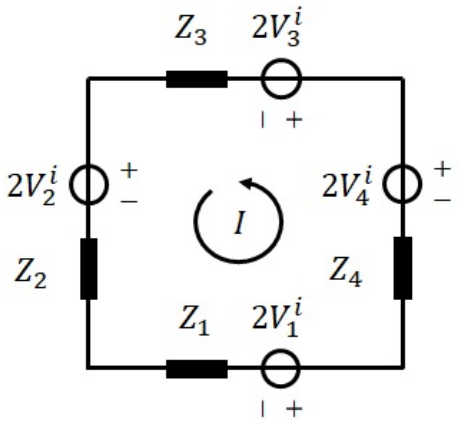

Fig. 2.4.3: Thévenin equivalent circuit at the node centre

Solving the Thévenin equivalent circuit gives

$$I = \frac{2\left(V_1^i + V_4^i - V_3^i - V_2^i\right)}{Z_1 + Z_2 + Z_3 + Z_4}, \tag{2.4.11}$$

and the reflected voltages from the node centre are

$$V_1^r = \left(2V_1^i - Z_1 I\right) - V_1^i = V_1^i - Z_1 I, \tag{2.4.12}$$

$$V_4^r = \left(2V_4^i - Z_4 I\right) - V_4^i = V_4^i - Z_4 I, \tag{2.4.13}$$

$$V_3^r = \left(2V_3^i + Z_3 I\right) - V_3^i = V_3^i + Z_3 I, \tag{2.4.14}$$

$$V_2^r = \left(2V_2^i + Z_2 I\right) - V_2^i = V_2^i + Z_2 I. \tag{2.4.15}$$

At the port connecting two series nodes (e.g. Fig. 2.4.2), the Thévenin equivalent

circuit can be described using Fig. 2.4.4, where Z_s is the characteristic impedance of the capacitive stub; it results from the stub capacitance calculated still via using $C_s = C - C_e$ as

$$C_s = \varepsilon\Delta l - \frac{(\Delta t/2)^2}{\mu\Delta l/2/2} \times 2 = \varepsilon\Delta l - \frac{2\Delta t^2}{\mu\Delta l}, \tag{2.4.16}$$

and the simulation time step of

$$\Delta t = \frac{\Delta l}{\sqrt{2}c_0} \tag{2.4.17}$$

will give zero stub capacitance in uniform Cartesian grids for vacuum.

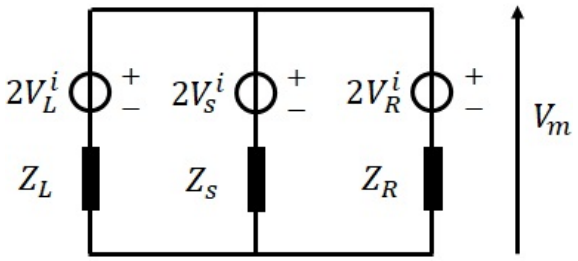

Fig. 2.4.4: Thévenin equivalent circuit at the port. Subscripts $_L$ and $_R$ stand for the left and the right side without loss of generality.

Applying nodal voltage analysis to Fig. 2.4.4 yields the the middle voltage at the port

$$V_m = \frac{2\left(\dfrac{V_L^i}{Z_L} + \dfrac{V_R^i}{Z_R} + \dfrac{V_s^i}{Z_s}\right)}{\dfrac{1}{Z_L} + \dfrac{1}{Z_R} + \dfrac{1}{Z_s}}, \tag{2.4.18}$$

and the reflected voltages are

$$V_L^r = V_m - V_L^i, \tag{2.4.19}$$

$$V_R^r = V_m - V_R^i, \tag{2.4.20}$$

$$V_s^r = V_m - V_s^i. \tag{2.4.21}$$

The reflected voltages from the node centres become the incident voltages towards the ports, and the reflected voltages from the ports become the incident voltages towards the node centres. The reflected voltage of the capacitive stub becomes the incident voltage in the next time step.

2.5 Conclusion

The classic Cartesian EM TLM methods have been introduced and derived from first principles in this chapter, mapping Maxwell's equations to the transmission-line circuit equations. Differential forms of Maxwell's equations are employed in the derivations since it is convenient to discretise space derivatives in Cartesian coordinates. For 2D TLM methods, the shunt TM model uses orthogonal transmission-line connections, whereas the series TE model employs mesh transmission-line connections. The scattering and connection process for the 2D shunt model and the 2D series model are very similar only with different Thévenin equivalent circuits that need to be solved. Next in Chapter 3, the TLM method will be extended to solve the thermal diffusion problem.

Chapter 3

Cartesian Thermal TLM Method

This chapter starts with a quick review of time-domain heat diffusion solvers. Then, the thermal version of the TLM methods in Cartesian grids are derived via mapping the heat diffusion parameters to the transmission-line parameters. The one-dimensional method and the two-dimensional method are covered respectively with detailed explanations on the scattering and connection process.

3.1 Overview

The simulation of heat conduction is widely used in many areas of scientific research from electronics to medical applications. The heating happens as a result of another physical or biological process such as microwave signal, lightning, and metabolism; in order to fully describe the transient or real-time thermal phenomena, time-domain numerical methods are needed. An adequate choice of methodology within which to develop especially multiphysics simulations is therefore important in terms of both numerical stability and computational efficiency. The algorithms to solve the thermal diffusion equation numerically in the time domain include the finite difference method [58], the finite volume method [59, 60] and the transmission-line modelling (TLM) method [57, 61]. Fully explicit finite difference schemes suffer from late time instability issues that are typical for large-scale problems. The stability condition can be improved using implicit schemes such as the Crank–Nicolson method, but they require matrix-solving which can become costly if the number of

samples is large, especially when the algorithm is applied in higher dimensions [58]. One of the main advantages of the TLM method is its unconditional stability [62]. As an explicit scheme, the TLM method is also easy to parallelise and is therefore computationally efficient for large-scale problems.

The TLM method, originally developed for microwave applications, has been developed to solve diffusion equations via modelling the diffusion process as low-frequency waves in highly lossy media [57, 61]. Over the years, it has been applied to a variety of thermal diffusion problems such as the modelling of the heat conduction in transistors [31, 32] and biomedical applications [63, 64]; it is also used in [35–37] as the thermal solver of the electrothermal coupling schemes.

3.1.1 Heat Diffusion Equation

The heat diffusion equation describes the heat conduction behaviour. If a substance is calorifically ideal, then its total heat energy Q (unit: J) can be expressed as

$$Q = c_p \rho_m T, \tag{3.1.1}$$

where ρ_m is the mass density in $\mathrm{kg} \cdot \mathrm{m}^{-3}$ and c_p is the specific heat capacity at constant pressure in $\mathrm{J} \cdot \mathrm{kg}^{-1} \cdot \mathrm{K}^{-1}$.

By Fourier's law of thermal conduction in an isotropic medium, the heat flux $\boldsymbol{F}$ (unit: $\mathrm{W} \cdot \mathrm{m}^{-2}$) is calculated as

$$\boldsymbol{F} = -k_{th} \nabla T, \tag{3.1.2}$$

where k_{th} is the thermal conductivity in $\mathrm{W} \cdot \mathrm{m}^{-1} \cdot \mathrm{K}^{-1}$.

The conservation of the total heat energy gives

$$\frac{\partial Q}{\partial t} + \nabla \cdot \boldsymbol{F} = Q_{VS}, \tag{3.1.3}$$

where Q_{VS} is the volume heat source in $\mathrm{W} \cdot \mathrm{m}^{-3}$.

Substituting (3.1.1) and (3.1.2) into (3.1.3) yields the thermal diffusion equation

$$\frac{\partial T}{\partial t} = \frac{k_{th}}{c_p \rho_m} \nabla^2 T + \frac{Q_{VS}}{c_p \rho_m}. \tag{3.1.4}$$

3.2 One-dimensional Thermal TLM

3.2.1 Model Derivation

In the one-dimensional case, we assume the heat flux and the change of temperature is in the x-direction only. Hence, the heat flux can be expressed as $\boldsymbol{F} \equiv (F_x, 0, 0)$ for now. Integrating both sides of (3.1.2) along an arbitrary length Δx from an arbitrary point x in the x-direction gives

$$\int_x^{x+\Delta x} F_x dx = -k_{th} \left[T\right]_x^{x+\Delta x} = -k_{th} \Delta T. \tag{3.2.1}$$

Then, we consider the one-dimensional thermal TLM node shown in Fig. 3.2.1.

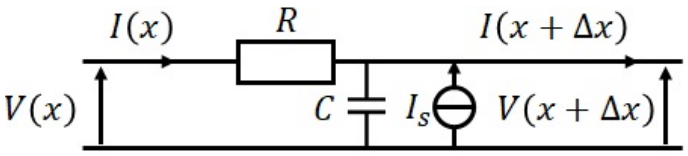

Fig. 3.2.1: A 1D thermal TLM node

In this 1D thermal TLM node, the voltage change along the x-direction is expressed as

$$\Delta V = V(x + \Delta x) - V(x) = -I(x)R. \tag{3.2.2}$$

Comparing (3.2.2) with (3.2.1), it is seen that they have similar structures. If we use the equivalences $V \leftrightarrow T$ and $I \leftrightarrow (\int_x^{x+\Delta x} F_x dx)/\Delta x$, the analogous resistance R is obtained to be

$$R = \frac{\Delta x}{k_{th}}. \tag{3.2.3}$$

Here, the transmission line current $I(x)$ is made equivalent to the integral average of the heat flux F_x. This equivalence can be simplified to $I \leftrightarrow F_x$ if we assume a piecewise constant distribution of F_x. The expression (3.2.3) is slightly different from the definition given in [57], but both definitions are correct because the fictitious

cross-sectional area A can be taken as unity without loss of generality since it is only a scaling factor when we make mappings. One can find the original physical quantity according to the associated scaling factor from the mapped quantity.

Next, multiplying both sides of (3.1.3) by Δx, substituting (3.1.1) into it, and expanding the divergence in 1D respectively yield

$$c_p \rho_m \Delta x \frac{\partial T}{\partial t} + \frac{\partial F_x}{\partial x} \Delta x = Q_{VS} \Delta x. \tag{3.2.4}$$

Back to Fig. 3.2.1, the current change along the x-direction is expressed as

$$\Delta I = I(x + \Delta x) - I(x) = -C \frac{dV(x)}{dt} + I_s. \tag{3.2.5}$$

If we keep the simplified mapping $I \leftrightarrow F_x$, then $\frac{\partial F_x}{\partial x} \Delta x$ is the first-order approximation of ΔI. Comparing (3.2.5) and (3.2.4) and also taking $V \leftrightarrow T$ yield

$$C = c_p \rho_m \Delta x, \tag{3.2.6}$$

$$I_s = Q_{VS} \Delta x. \tag{3.2.7}$$

Different from the EM TLM method, the thermal TLM method does not have a time step limit from its numerical stability point of view because there is no inductance in the model formulation, and there is no non-physical electrical component quantity caused by the time step. Instead, it has a suggested time step to balance the unwanted underlying wave phenomena and the simulation run-time. For the Cartesian thermal TLM method, the suggested time step could be the RC constant in the model [65].

3.2.2 Scattering and Connection

We consider two adjacent 1D thermal TLM nodes shown as Fig. 3.2.2a. The capacitors are modelled using links, while the resistors and the current sources remain as themselves, giving the resultant Thévenin equivalent circuit as Fig. 3.2.2, where Z_C is the characteristic impedance of the capacitive link, and V_m is the middle

voltage at the port interface. Note that when calculating Z_C, the single trip time equals the simulation time step Δt (i.e. $Z_C = \Delta t/C$).

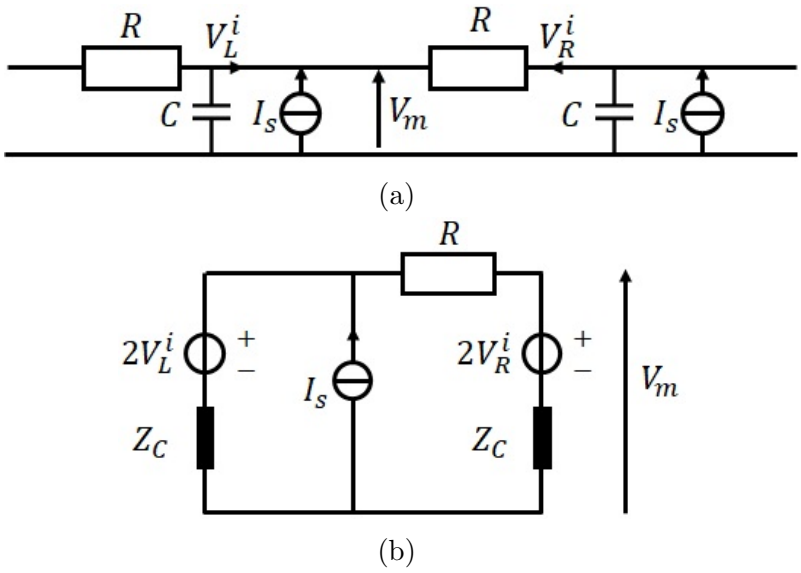

Fig. 3.2.2: (a) Two adjacent 1D thermal TLM nodes and (b) the Thévenin equivalent circuit at the port.

Applying nodal voltage analysis leads to the middle voltage

$$V_m = \frac{\dfrac{2V_L^i}{Z_C} + \dfrac{2V_R^i}{Z_C + R} + I_s}{\dfrac{1}{Z_C} + \dfrac{1}{Z_C + R}}, \tag{3.2.8}$$

and the reflected voltages of the left and the right side are

$$V_L^r = V_m - V_L^i, \tag{3.2.9}$$

$$V_R^r = \left(V_m - \frac{V_m - 2V_R^i}{Z_C + R} R\right) - V_R^i. \tag{3.2.10}$$

After the scattering, the connection is completed via taking the reflected voltage from the adjacent node as the incident voltage, which is the same as that of the 1D EM TLM method.

3.3 Two-dimensional Shunt Model

3.3.1 Model Derivation

In the two-dimensional case, we assume the heat flux and the temperature distribution relate only with x and y (i.e. $\partial/\partial z = 0$), and the heat flux now is expressed as $\boldsymbol{F} \equiv (F_x, F_y, 0)$. The 2D shunt model from the EM TLM method is modified to cope with the diffusion problem, leading to the node shown in Fig. 3.3.1.

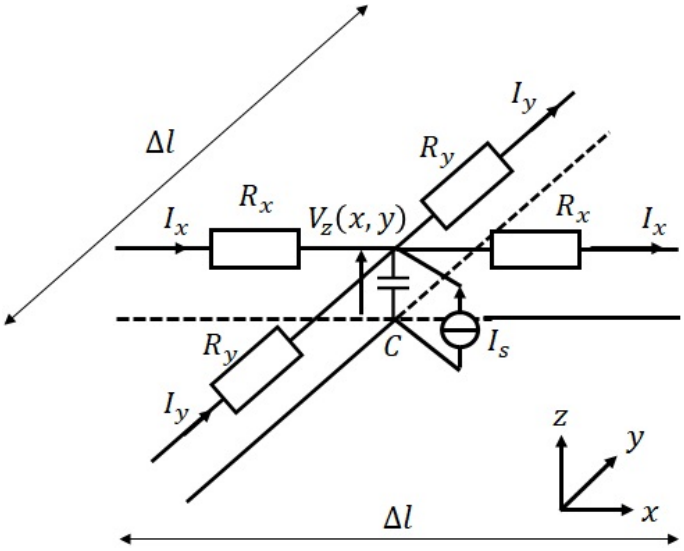

Fig. 3.3.1: A 2D thermal TLM shunt node

It is seen that the inductors in the EM TLM shunt node are replaced by resistors in the thermal TLM shunt node, and $\Delta x = \Delta y = \Delta l$ is assumed for the sake of simplicity. To evaluate the analogous resistance, two adjacent shunt nodes are considered together. Fig. 3.3.2 shows two shunt nodes connected in the x-direction, and the y-direction components are omitted for now.

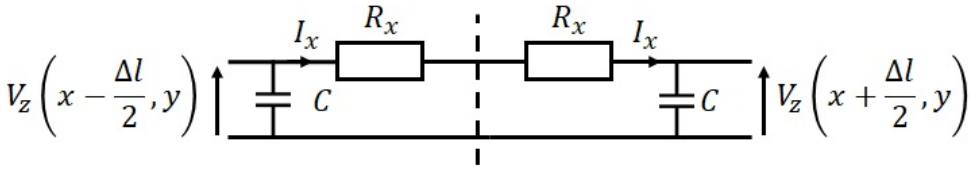

Fig. 3.3.2: Two adjacent 2D thermal TLM nodes in the x-direction

Integrating both sides of (3.1.2) along an arbitrary length Δl from an arbitrary point $(x - \frac{\Delta l}{2}, y)$ in the x-direction gives

$$\int_{x-\Delta l/2}^{x+\Delta l/2} F_x dx = -k_{th} \left[T\right]_{x-\Delta l/2}^{x+\Delta l/2} = -k_{th}\Delta_x T. \tag{3.3.1}$$

Since the integration route is along the x-direction, the y-components of the heat flux and the temperature change are not involved in (3.3.1). Similar to the case in one-dimension, the analogous current I_x can be mapped to the integral average of the heat flux along the x-direction within the Cartesian computational cell of edge length Δl; or similarly, a simplified mapping of $I_x \leftrightarrow F_x$ can be used. Taking $V_z \leftrightarrow T$ as well yields

$$I_x \Delta l = -k_{th} \left(V_z(x + \Delta l/2, y) - V_z(x - \Delta l/2, y)\right). \tag{3.3.2}$$

According to $IR = -\Delta V$, the analogous resistance in the x-direction R_x is obtained as

$$R_x = \frac{1}{2}\frac{\Delta l}{k_{th}}, \tag{3.3.3}$$

where the coefficient $1/2$ in the front is because we intentionally divide the total resistance into two R_x from two adjacent nodes.

The analogous resistance in the y-direction is obtained in a similar way, giving

$$R_y = \frac{1}{2}\frac{\Delta l}{k_{th}}. \tag{3.3.4}$$

Next, multiplying both sides of (3.1.3) by Δl, substituting (3.1.1) into it, and also expanding the divergence in 2D yield

$$c_p \rho_m \Delta l \frac{\partial T}{\partial t} + \frac{\partial F_x}{\partial x}\Delta l + \frac{\partial F_y}{\partial y}\Delta l = Q_{VS}\Delta l. \tag{3.3.5}$$

If we keep the simplified mappings $I_x \leftrightarrow F_x$ and $I_y \leftrightarrow F_y$, the second term and the third term of the LHS of (3.3.5) become the first-order approximation of the change of current in two coordinate directions respectively, namely ΔI_x and ΔI_y.

According to $\Delta I = -C\frac{dV}{dt} + I_s$, the analogous capacitance and the analogous current source are obtained as

$$C = c_p \rho_m \Delta l, \tag{3.3.6}$$

$$I_s = Q_{VS} \Delta l. \tag{3.3.7}$$

Similar to the 1D thermal TLM method, the suggested simulation time step could be the RC constant in the model [65].

3.3.2 Scattering and Connection

The scattering and connection for the 2D thermal TLM method is also conducted by alternating the process at node centres and the process at ports. At the node centre, the central capacitor in Fig. 3.3.1 should be shared evenly among four transmission-line branches (i.e. $C/4$ in each), leading to the Thévenin equivalent circuit shown in Fig. 3.3.3, where $Z_1 = Z_2 = Z_3 = Z_4 = Z_C$ is the characteristic impedance of the capacitive link, and V_M is the middle voltage at the node centre. Note that the link model of capacitors is used, and when calculating Z_C for the 2D thermal TLM method, the single trip time equals half of the simulation time step (i.e. $\Delta t/2$). The impedance of the capacitive link is calculated as

$$Z_C = \frac{\Delta t/2}{C/4} = \frac{2\Delta t}{C}. \tag{3.3.8}$$

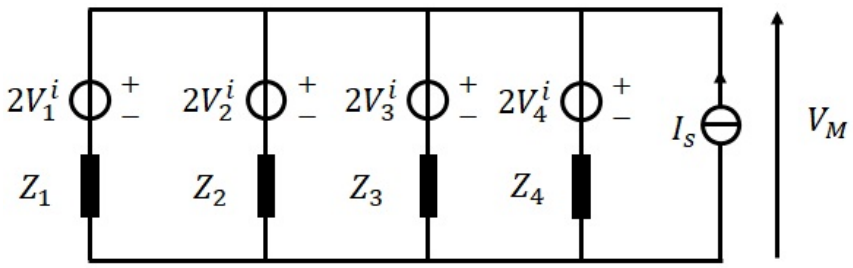

Fig. 3.3.3: Thévenin equivalent circuit at the centre of the 2D thermal TLM node

Solving the circuit in Fig. 3.3.3 gives the middle voltage as

$$V_M = \frac{\frac{2V_1^i}{Z_1} + \frac{2V_2^i}{Z_2} + \frac{2V_3^i}{Z_3} + \frac{2V_4^i}{Z_4} + I_s}{\frac{1}{Z_1} + \frac{1}{Z_2} + \frac{1}{Z_3} + \frac{1}{Z_4}}, \tag{3.3.9}$$

and the reflected voltages from the node centres are

$$V_1^r = V_M - V_1^i, \tag{3.3.10}$$

$$V_2^r = V_M - V_2^i, \tag{3.3.11}$$

$$V_3^r = V_M - V_3^i, \tag{3.3.12}$$

$$V_4^r = V_M - V_4^i. \tag{3.3.13}$$

At the port interface, the Thévenin equivalent circuit is sketched in Fig. 3.3.4, where V_N is the middle voltage at the port.

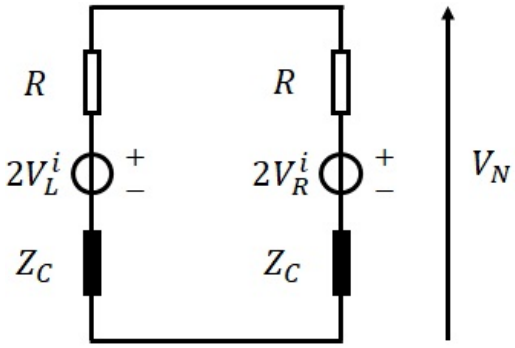

Fig. 3.3.4: Thévenin equivalent circuit at the port interface of two 2D thermal TLM nodes

Solving the equivalent circuit in Fig. 3.3.4 leads to the middle voltage

$$V_N = \frac{\frac{2V_L^i}{Z_C + R} + \frac{2V_R^i}{Z_C + R}}{\frac{1}{Z_C + R} + \frac{1}{Z_C + R}} = V_L^i + V_R^i, \tag{3.3.14}$$

and the reflected voltages from the ports are

$$V_L^r = \left(V_N - \frac{V_N - 2V_L^i}{Z_C + R} R\right) - V_L^i, \tag{3.3.15}$$

$$V_R^r = \left(V_N - \frac{V_N - 2V_R^i}{Z_C + R} R\right) - V_R^i. \tag{3.3.16}$$

The reflected voltages from the node centre become the incident voltages towards the port, and the reflected voltages from the port become the incident voltages towards the node centre, forming connection.

3.4 Conclusion

The application of the TLM in solving thermal diffusion problems has been covered in this chapter. The one-dimensional thermal TLM method and the two-dimensional method have been derived and explained respectively. In summary, thermal TLM methods model the thermal resistance using resistors, model the total heat capacity using capacitors and model the heat source using current sources (current generators). All the derived electrical component quantities in this chapter agree with the classic definitions given in [57], and the fictitious cross-sectional area A is treated as unity because the choice of scaling factors in mapping does not ruin the generality and the final result when thermal quantities (e.g. temperature) are mapped back. The concept of scaling factor is also useful when we derive unstructured TLM methods (EM and thermal) in Chapter 4 and Chapter 5 respectively.

Chapter 4

Two-dimensional EM UTLM

In this chapter, the Delaunay triangular mesh and its dual mesh, the Voronoi mesh, used in the UTLM methods are introduced first. Then, the classic EM UTLM method using TM shunt nodes is derived in an alternative way, and a new EM UTLM method using TE series nodes is presented and validated. The scattering and connection process of the TM shunt UTLM method and the TE series UTLM method is explained respectively in details. Furthermore, the algorithm to optimise the Delaunay mesh for the UTLM methods is introduced.

4.1 Overview

Simulations based on structured grids usually tend to run faster in terms of processing a single computational cell because in most programming languages, structured data stored in arrays are cached well, but structured grids may not provide a smooth discretisation for arbitrary curved domain boundaries. One may reduce the global cell size, which may significantly increase the total number of cells, or use the conformal meshing method [66, 67], which increases the density of grid lines only at the area of interest, or use the adaptive mesh refinement method [68, 69], where small cells that are not bounded by fixed grid lines are placed at the area of interest. Alternatively, unstructured grids, on account of the flexible orientations and sizes of their facets (triangles), naturally provide smooth boundaries for curved shapes.

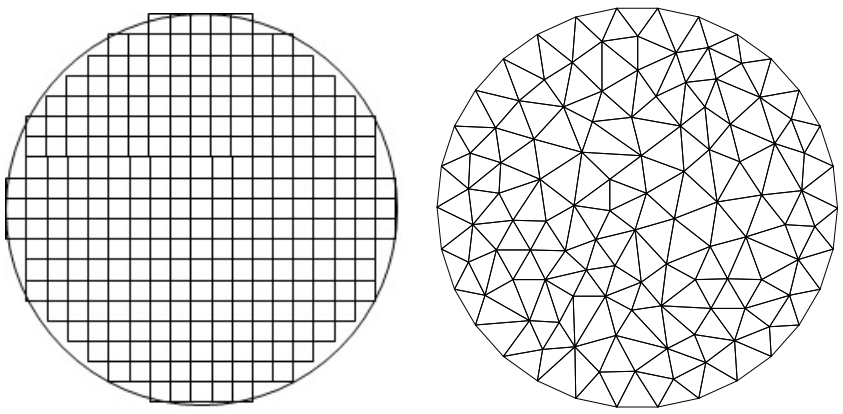

(a) (b)

Fig. 4.1.1: Comparison between (a) the structured Cartesian mesh (265 squares) and (b) the unstructured triangular mesh (202 triangles)

As is shown in Fig. 4.1.1, the triangular mesh uses fewer elements but has a significantly smoother boundary than the square mesh so that the stair-casing effects at the boundary can be reduced. To cover the blanks in the stair-casing parts of Fig. 4.1.1a better, finer mesh resolutions are required, and the number of square cells will far exceed the number of triangles in Fig. 4.1.1b.

Simulations based on unstructured grids may not be as efficient as those using structured grids in terms of processing a single cell due to the neighbour-finding in the algorithm aspect and the cache misses in the hardware aspect, but a smaller number of elements (triangles) are needed for a reasonable discretisation of the space with insignificant star-casing effects. In the context of EM simulations, singularities of the EM field at tip-shape areas can be described better by using unstructured triangular meshes. In addition, unstructured modelling techniques can also be used to connect two or more structured computational grids [70, 71], giving the compatibility to different grid resolutions but still maintaining the processing speed and parallel computing prospects in each structured grid.

The fundamental concept going through the derivation of the two-dimensional unstructured TLM (UTLM) methods is to relate arbitrary pairs of points in the 2D plane. Similar to Cartesian TLM nodes, each UTLM node has one node centre and typically 3 link lines (instead of 4 in Cartesian) connecting to its neighbours. Usually, the circumcentres of Delaunay triangles [72] are chosen as the UTLM node centres, and the link lines are then along the Voronoi edges [73].

4.2 Delaunay Triangulation

4.2.1 Definition and Triangulation Algorithm

The Delaunay triangulation is a reliable method to obtain an unstructured computational grid, and it has the advantage of maximising the minimum angle among all triangles, which is one of the criteria to evaluate the mesh quality. The theory behind the Delaunay triangulation and the two-dimensional triangulation software used in this thesis are referred to the `Triangle Project` by Shewchuk [72]. Multiple but equivalent definitions of a Delaunay mesh are presented in [72, 74] which state that a triangle mesh is Delaunay if one of the following is satisfied, and if so, the other two are satisfied automatically. Illustrative diagrams are shown in Fig. 4.2.1. In Fig. 4.2.1a, the circumcircles do not contain vertices of other triangles, so the mesh is Delaunay, whereas in Fig. 4.2.1b, the red circumcircle contains one blue vertex, resulting in a non-Delaunay mesh; in Fig. 4.2.1c, each edge can find a circumcircle that does not contain other vertices, so the mesh is Delaunay, whereas in Fig. 4.2.1d, the purple edge cannot find a circumcircle that does not contain other vertices, resulting in a non-Delaunay mesh.

1. (Delaunay Triangle) For all triangles in the mesh, a circumcircle of each triangle does not contain vertices of any other triangles.

2. (Delaunay Edge) For all edges in the mesh, at least one circumcircle of each edge does not contain the other vertices.

3. (Locally Delaunay Edge) For all edges in the mesh, at least one circumcircle of each edge does not contain the other vertices of triangles that use this edge.

For a given point set in two-dimension, its Delaunay triangulation can be found by solving an associated three-dimensional convex hull problem [72]. First, each 2D point in the $x - y$ plane is lifted to a height in the z-direction defined by either a parabolic function or a sphere function, known as the parabolic lifting map [75] and the spherical lifting map [76] respectively. Then, the 3D convex hull of the lifted points is solved. The triangles on the surface of this convex hull provide how lifted

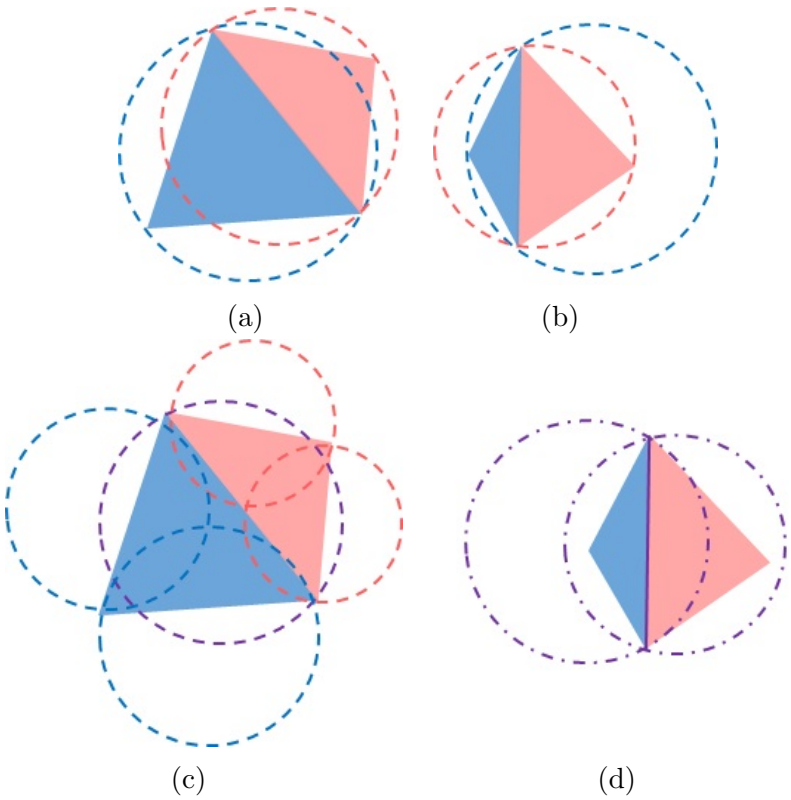

Fig. 4.2.1: (a) Delaunay triangles, (b) non-Delaunay triangles, (c) Delaunay edges, and (d) one non-Delaunay edge.

points are connected, and applying those connections back to the original 2D points yields a Delaunay triangulation of this 2D point set.

In terms of numerical performance, [74] recommends using the parabolic lifting map. Fig. 4.2.2 illustrates how the parabolic lifting map turns a 2D Delaunay triangulation problem (in the $x-y$ plane) into a 3D convex hull problem. The 2D points A, B, C and D are lifted to A', B', C' and D' respectively by a parabolic function, and the 3D convex hull of the lifted points contains $\Delta A'B'C'$ and $\Delta B'C'D'$. Then, since $A'B'$ is on the 3D convex hull, AB should be included in the 2D triangulation; so do AC, BC, BD and CD, and these edges provide a Delaunay triangulation of the original 2D points A, B, C and D. Therefore, once the 3D convex hull is solved, the 2D Delaunay triangulation is obtained. The the convex hull algorithm is a topic in computer science, and one may refer to [77]. The Shewchuk triangulation code implements a combination of the divide-and-conquer algorithm, the incremental algorithm and the sweepline algorithm to generate Delaunay meshes. After a Delaunay triangulation is obtained, its corresponding Voronoi mesh is created by taking its circumcentres as new vertices and connecting each pair of two

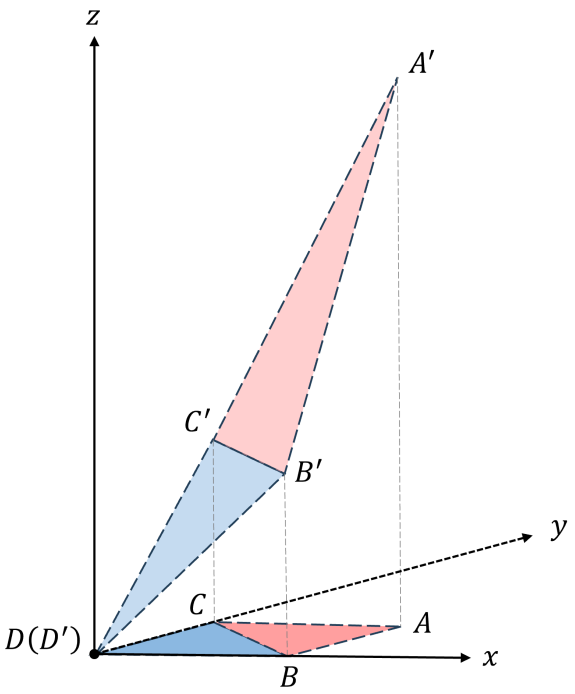

Fig. 4.2.2: The parabolic lifting map. Light blue / light red triangles ($\Delta A'B'C'$ and $\Delta B'C'D'$) are formed by lifted points, and dark blue / dark red triangles (ΔABC and ΔBCD) are formed by original 2D points.

circumcentres of two adjacent triangles using new edges. Especially, if a triangle is at the boundary, one or more edges of its circumcentre connect to infinity; when an edge connects to infinity, it starts from a circumcentre, leads to the direction point to the midpoint of the boundary edge, and extends to infinity. An example Delaunay mesh and the corresponding Voronoi mesh are shown in Fig. 4.2.3. The Voronoi mesh reveals the link lines used in the unstructured TLM, and the Delaunay property ensures a positive length for link-lines, which will be seen later in this chapter.

4.2.2 Space Discretisation in UTLM

The two-dimensional problem geometry is discretised using Delaunay triangles in UTLM methods. Circumcentres of all triangles are chosen as the computational node centres, and the transmission-lines are the segments along the Voronoi edges, connecting adjacent node centres. Fig. 4.2.4a shows an arbitrary triangular UTLM node, where Δ_0, Δ_1 and Δ_2 are the distances of link-lines connecting node centres to ports. Fig. 4.2.4b shows the connection between two adjacent UTLM nodes.

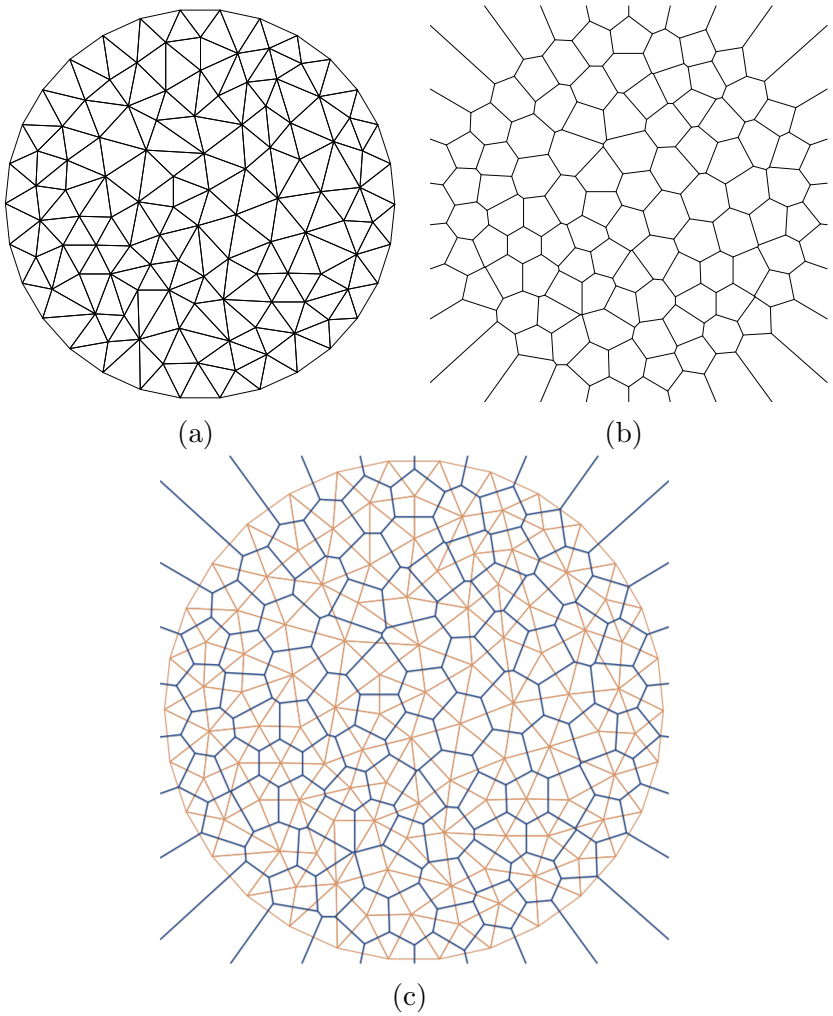

Fig. 4.2.3: (a) The Delaunay mesh, (b) the Voronoi mesh, and (c) the cascaded view of these two meshes.

Both the classic shunt TM UTLM method and the newly proposed series TE UTLM method use the same space discretisation scheme, and as will be seen in this chapter later, they only involve different Thévenin equivalent circuits to solve during the scattering and connection process. The optimal Delaunay triangulation (ODT) algorithm [78, 79] covered in Section 4.5 can be used to optimise the triangulation, making the shapes and sizes of triangles more uniform, which practically gives a larger simulation time step.

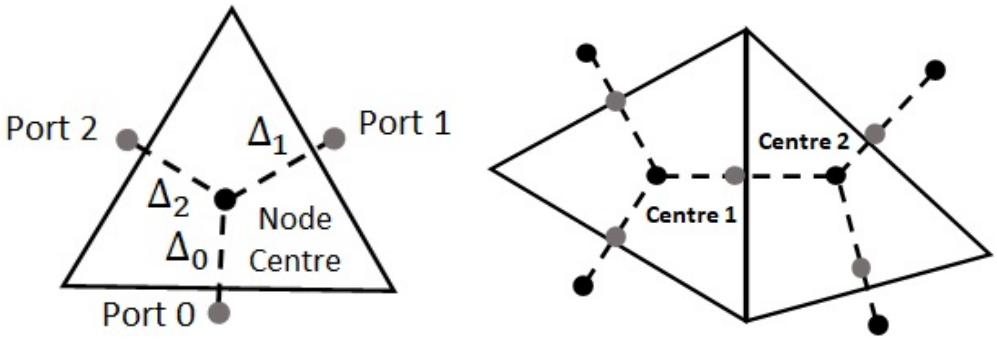

(a) (b)

Fig. 4.2.4: Schematic presentation of (a) single triangular node (b) nodes and link-lines for two adjacent triangles. Solid black circles represent node centres, and grey solid circles represent ports.

4.3 Two-dimensional Unstructured Shunt Model

4.3.1 Review

For two-dimensional problems, two categories of electromagnetic (EM) TLM models exist depending on the type of field configurations that is of interest, namely the series transverse electric (TE) model and the shunt transverse magnetic (TM) model (see [57] and also Chapter 2). The original derivation of the 2D EM shunt UTLM [71] was based on the solution of wave equations in cylindrical coordinates, and here another approach is presented. This alternative approach is based on the integral form of Maxwell's curl equations:

$$\oint_{\partial\Omega} \boldsymbol{E} \cdot d\boldsymbol{l} = -\mu \frac{d}{dt} \iint_{\Omega} \boldsymbol{H} \cdot d\boldsymbol{A}, \tag{4.3.1}$$

$$\oint_{\partial\Omega} \boldsymbol{H} \cdot d\boldsymbol{l} = \varepsilon \frac{d}{dt} \iint_{\Omega} \boldsymbol{E} \cdot d\boldsymbol{A}. \tag{4.3.2}$$

The integral forms are irrespective of the coordinate system. Different from the derivations of Cartesian TLM methods where differential forms are used, unstructured meshes in general do not align with any structured coordinates so that partial derivatives are not easy to discretise, so in this thesis, an alternative approach that uses the integral forms is presented.

Fig. 4.3.1 shows the layout of an arbitrary 2D three-port EM UTLM shunt node. Comparing Fig. 4.3.1 with the 2D Cartesian shunt node (Fig. 2.3.1), it is

seen that transmission line branches of Cartesian nodes and unstructured nodes are similar except that the central capacitance in Fig. 2.3.1 is shared evenly among 4 link lines. Furthermore, following the node clustering technique [71], two isosceles right-angled triangular nodes can be combined into a square node which is very close to the Cartesian shunt square node except that the defined positions of the shunt capacitors are shifted by half space step ($\Delta l/2$) from node centres to ports (see Fig. 4.3.2). It implies the idea that the unstructured TLM method is naturally compatible with the Cartesian TLM method.

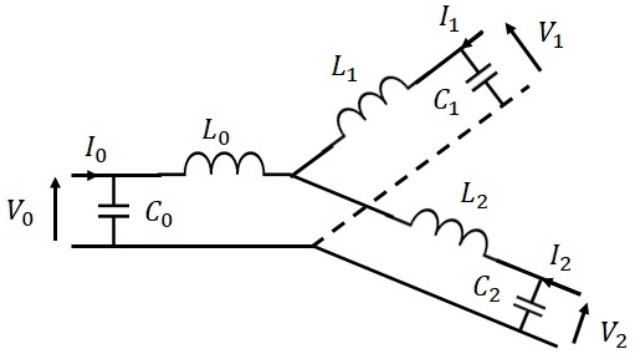

Fig. 4.3.1: A 2D three-port EM UTLM shunt node

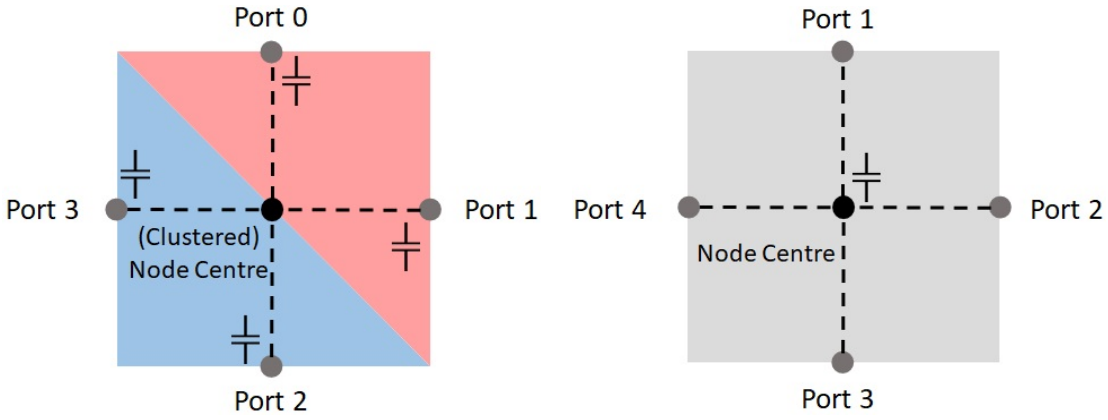

Fig. 4.3.2: (a) The clustered 2D shunt UTLM node with shunt capacitors at ports; (b) The 2D Cartesian shunt TLM node with the shunt capacitor at the node centre.

4.3.2 Assumptions and Mappings

Fig. 4.3.3 illustrates two local adjacent triangles which is used to derive the shunt UTLM formulation based on integral Maxwell's equations. The concept of the

average field strength and the midpoint rule of integration are used in the following derivations.

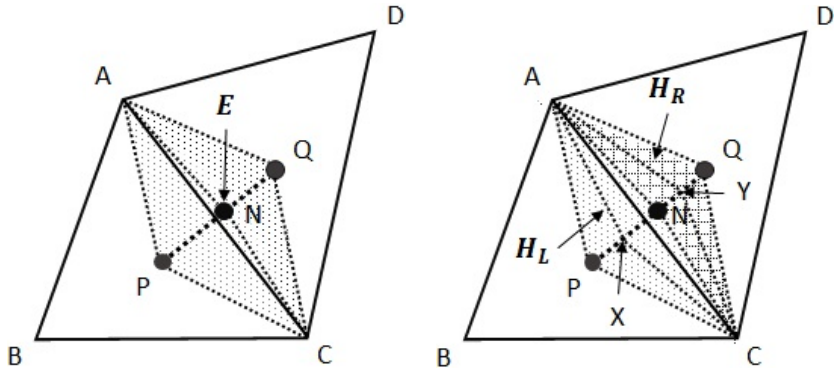

Fig. 4.3.3: $\boldsymbol{H_L}$ and $\boldsymbol{H_R}$ represent the average magnetic field strength in quadrilateral $APCN$ and quadrilateral $AQCN$ (denoted as the left side and the right side) respectively. $\boldsymbol{E}$ is the electric field strength at point N. ΔABC and ΔADC are Delaunay triangles. P and Q are circumcentres and also node centres. N is the port connecting two adjacent nodes and is usually the midpoint of PQ. X and Y are the midpoints of PN and QN.

The relationship between the electric field $\boldsymbol{E} \equiv (0, 0, E_z)$ and the analogous voltage remains similar to the Cartesian shunt TLM method, given as

$$V_z \leftrightarrow E_z \Delta z. \tag{4.3.3}$$

The line integral of the magnetic field strength $\boldsymbol{H} \equiv (H_x, H_y, 0)$ along $\overline{CXA}$ and $\overline{CYA}$ are mapped to the analogous current I_L and I_R respectively in Fig. 4.3.3b, expressed as

$$I_L \leftrightarrow \int_C^X \boldsymbol{H_L} \cdot d\boldsymbol{l} + \int_X^A \boldsymbol{H_L} \cdot d\boldsymbol{l} = \boldsymbol{H_L} \cdot \Delta \boldsymbol{l}, \tag{4.3.4}$$

$$I_R \leftrightarrow \int_C^Y \boldsymbol{H_R} \cdot d\boldsymbol{l} + \int_Y^A \boldsymbol{H_R} \cdot d\boldsymbol{l} = \boldsymbol{H_R} \cdot \Delta \boldsymbol{l}, \tag{4.3.5}$$

where subscripts $_L$ and $_R$ denote the left side and the right side respectively, and $\Delta \boldsymbol{l} = \overrightarrow{CA}$. This analogous current connects each node centre to the port. Note that the magnetic field strength $\boldsymbol{H}$ does not need to be constant along $\overline{CXA}$ or $\overline{CYA}$, but there exists an average magnetic field strength, which is constant, to give the same line integral result when this average magnetic field strength is dot-multiplied with $\boldsymbol{\Delta l}$. $\boldsymbol{H}_L$ and $\boldsymbol{H}_R$ are the average magnetic field strengths of each side respectively

in this case. Furthermore, the direction of $\boldsymbol{\Delta l}$ can be defined according to either the counter-clockwise or the clockwise convention, as long as it is kept consistent for the whole mesh.

4.3.3 Derivation of Electric Component Quantities

Firstly we use the integral form of Faraday's law (4.3.1). The integration surface Ω is chosen to be the vertical slice of the shunt model as we look down perpendicular to the plane $ABCD$ in Fig. 4.3.3b. Note that as is shown, the port N can be chosen at places other than the midpoint between PQ, although in practice, the midpoint is usually chosen to give a larger simulation time step.

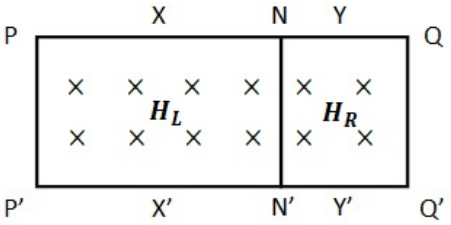

Fig. 4.3.4: Vertical slice of $\overline{PNQ}$

Applying Faraday's law on surface $PP'N'N$ gives,

$$E_{PP'}\Delta z + 0 - E_{NN'}\Delta z - 0 = -\mu \frac{d}{dt}\left(\boldsymbol{H_L} \cdot \boldsymbol{A}\right), \tag{4.3.6}$$

where $\Delta z = PP' = QQ'$. The vector area element $\boldsymbol{A}$ in (4.3.6) has the same direction as the vector $\boldsymbol{\Delta l}$ in (4.3.4) because $PQ \perp CA$. Substituting (4.3.4) and (4.3.3) into (4.3.6) yields

$$V_{PP'} - V_{NN'} = -\mu \frac{d}{dt}\left(I_L \frac{|\boldsymbol{A}|}{|\boldsymbol{\Delta l}|}\right) = -\mu \frac{d}{dt}\left(I_L \frac{|\overrightarrow{PN}|\Delta z}{|\boldsymbol{\Delta l}|}\right). \tag{4.3.7}$$

By inspection we obtain the analogous inductance L_{PN} according to $\Delta V = -L \cdot dI/dt$. Note that Δz is taken as unity without loss of generality because it is only a scaling factor in the mapping process.

$$L_{PN} = \frac{\mu|\overrightarrow{PN}|}{\Delta l}, \tag{4.3.8}$$

where $\Delta l = |\boldsymbol{\Delta l}|$.

We can get the analogous inductance L_{QN} on the right side using the same way.

$$L_{QN} = \frac{\mu|\overrightarrow{QN}|}{\Delta l} \tag{4.3.9}$$

Then we use the integral form of Ampere's law (4.3.2). The integration surface Ω is chosen as the quadrilateral $AYCX$ in Fig. 4.3.3a, leading to

$$\int_C^X \boldsymbol{H_L} \cdot d\boldsymbol{l} + \int_X^A \boldsymbol{H_L} \cdot d\boldsymbol{l} - \int_C^Y \boldsymbol{H_R} \cdot d\boldsymbol{l} - \int_Y^A \boldsymbol{H_R} \cdot d\boldsymbol{l} = \varepsilon \frac{d}{dt} (\boldsymbol{E} \cdot \boldsymbol{A}) . \tag{4.3.10}$$

Substituting (4.3.4), (4.3.5) and (4.3.3) into (4.3.10) gives

$$I_L - I_R = \varepsilon \frac{d}{dt} \left(V_{NN'} \Delta l |\overrightarrow{XY}| \right) . \tag{4.3.11}$$

Note that the vector area element $\boldsymbol{A}$ in (4.3.10) has the same direction as the electric field $\boldsymbol{E}$, and the area is still calculated based on $PQ \perp CA$. Δz is still taken as unity.

By inspection the total analogous capacitance C_{tot} is obtained according to $\Delta I = C \cdot dV/dt$.

$$C_{tot} = \varepsilon \cdot |\overrightarrow{XY}| \cdot \Delta l = \varepsilon \cdot |\overrightarrow{PN}| \cdot \Delta l = \varepsilon \cdot |\overrightarrow{QN}| \cdot \Delta l \tag{4.3.12}$$

To share the capacitance between two adjacent UTLM nodes, we divide this capacitance by 2 intentionally, giving

$$C_L = C_R = \frac{\varepsilon \cdot |\overrightarrow{PN}| \cdot \Delta l}{2} = \frac{\varepsilon \cdot |\overrightarrow{QN}| \cdot \Delta l}{2}. \tag{4.3.13}$$

If we let $\Delta_i = |\overrightarrow{XY}| = |\overrightarrow{PN}| = |\overrightarrow{QN}|$, then the expressions of the inductance and the capacitance become

$$L_i = \frac{\mu \Delta_i}{\Delta l}, \tag{4.3.14}$$

$$C_i = \frac{\varepsilon \Delta_i \Delta l}{2}, \tag{4.3.15}$$

where the subscript $_i$ denotes the edge index within each individual triangle, and $i = 0, 1, 2$. The derived expressions of the inductance and the capacitance match the definitions given in [71].

4.3.4 Scattering and Connection

To conduct the scattering and connection process, the equivalent circuits at the node centre and the ports should be figured out respectively. We use links to model inductors and stubs to model capacitors, and similar to the cases in Cartesian TLM methods, the stub capacitance is evaluated via using $C_s = C - C_e$, which means that the error capacitance due to the inductive link should be deducted from the original model capacitance. In the case of EM shunt UTLM method, the stub capacitance at the port is evaluated as

$$C_{s,i} = C_i - \frac{(\Delta t/2)^2}{L_i} = \frac{\varepsilon \Delta_i \Delta l}{2} - \frac{(\Delta t/2)^2 \Delta l}{\mu \Delta_i}, \tag{4.3.16}$$

where Δt is the simulation time step, and $\Delta t/2$ is the single trip time of the inductive link. From $C_{s,i} \geq 0$ we obtain the time step limit as

$$\Delta t \leq \sqrt{2\mu\varepsilon} \cdot \max_{\text{all triangles}} \{\Delta_i\}, \tag{4.3.17}$$

which is the same as the definition in [71].

Fig. 4.3.5 shows the Thévenin equivalent circuit at the node centre, where subscripts $_{0,1,2}$ refer to three shunt-connected transmission lines, and V_M is the middle voltage at the node centre.

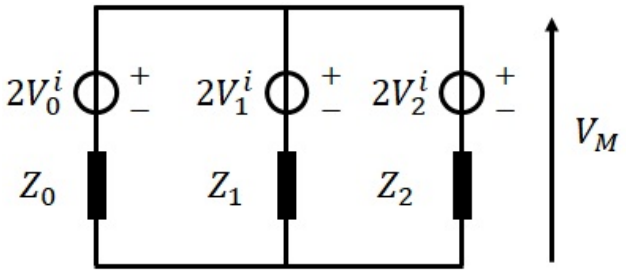

Fig. 4.3.5: Thévenin equivalent circuit at the centre of the 2D shunt EM UTLM node

The characteristic impedance of inductive links (Z_0, Z_1 and Z_2) is calculated with the single trip time taken as $\Delta t/2$, giving

$$Z_i = \frac{2\mu\Delta_i}{\Delta t \Delta l}, \tag{4.3.18}$$

where $i = 0, 1, 2$.

Applying nodal voltage analysis to the circuit in Fig. 4.3.5 yields the middle voltage at the centre

$$V_M = \frac{\frac{2V_0^i}{Z_0} + \frac{2V_1^i}{Z_1} + \frac{2V_2^i}{Z_2}}{\frac{1}{Z_0} + \frac{1}{Z_1} + \frac{1}{Z_2}}, \tag{4.3.19}$$

and the reflected voltages are

$$V_0^r = V_M - V_0^i, \tag{4.3.20}$$

$$V_1^r = V_M - V_1^i, \tag{4.3.21}$$

$$V_2^r = V_M - V_2^i. \tag{4.3.22}$$

Fig. 4.3.6 shows the Thévenin equivalent circuit at the port, where subscripts $_{L,R}$ refer to the left side and the right side, the subscript $_s$ refer to the capacitive stub, and V_N is the middle voltage at the port.

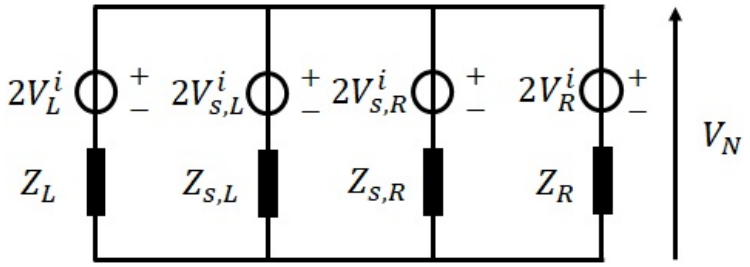

Fig. 4.3.6: Thévenin equivalent circuit at the port connecting two 2D shunt EM UTLM nodes

The characteristic impedance of capacitive stubs is calculated with the round trip time taken as Δt, giving

$$Z_{s,i} = \frac{\Delta t}{2C_{s,i}}, \tag{4.3.23}$$

or, the characteristic admittance is

$$Y_{s,i} = \frac{2C_{s,i}}{\Delta t} = \frac{\varepsilon \Delta_i \Delta l}{\Delta t} - \frac{\Delta t \Delta l}{2\mu \Delta_i}. \tag{4.3.24}$$

Applying nodal voltage analysis to the circuit in Fig. 4.3.6 gives the middle voltage at the port

$$V_N = \frac{\frac{2V_L^i}{Z_L} + \frac{2V_R^i}{Z_R} + \frac{2V_{s,L}^i}{Z_{s,L}} + \frac{2V_{s,R}^i}{Z_{s,R}}}{\frac{1}{Z_L} + \frac{1}{Z_R} + \frac{1}{Z_{s,L}} + \frac{1}{Z_{s,R}}}, \tag{4.3.25}$$

and the reflected voltages are

$$V_L^r = V_N - V_L^i, \qquad (4.3.26) \qquad V_R^r = V_N - V_R^i, \qquad (4.3.27)$$

$$V_{s,L}^r = V_N - V_{s,L}^i, \qquad (4.3.28) \qquad V_{s,R}^r = V_N - V_{s,R}^i. \qquad (4.3.29)$$

After the scattering is completed, the reflected voltages from the node centres become the incident voltages to the ports, and the reflected voltages from the ports become the incident voltages to the node centres. The incident voltages of the capacitive stubs equal the reflected voltages.

4.4 Two-dimensional Unstructured Series Model

4.4.1 Review

In the previous section, the shunt model version of the UTLM method [71] is introduced and re-derived with the principal electromagnetic field components being E_z, H_x and H_y. However, for certain classes of problems (e.g. the coupled electrothermal simulations with the Drude plasma model [37]), TE modes are more relevant. Although one can utilise the duality of the electric and magnetic fields to simulate TE waves with the shunt TM model, the TE series model itself is more useful as it assumes the transverse electric field components (E_x and E_y) to be principal. This is especially convenient as both the coupling between the electromagnetic and thermal behaviour and the change of parameters in the Drude plasma model are done via the electric field components. Therefore, here we derive a new two-dimensional UTLM method, namely 2D TE series node UTLM method. This method is validated in the case of the metallic cylindrical resonator and also applied to the problem of a photonic nanotip taper waveguide. The schematic of the TE triangular node, the parameters of link lines and the 2D series UTLM algorithm are presented as follows.

4.4.2 Node Layout and Quantity Mapping

The derivation of the 2D series UTLM method is also based on the integral form of Maxwell's curl equations given as (4.3.1) (4.3.2).

Fig. 4.4.1 shows the layout of a single series UTLM node, where inductors (L_0, L_1 and L_2) model the permeability along each triangle edge, and capacitors (C_0, C_1 and C_2) model the permittivity along each triangle edge. The voltages across each capacitor are denoted as V_0, V_1 and V_2, and the loop current within this series node is denoted as I.

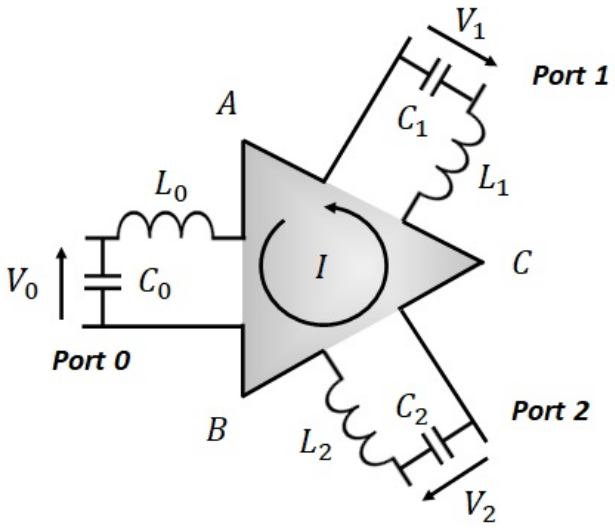

Fig. 4.4.1: A single 2D TE series node in unstructured TLM

Fig. 4.4.2 shows the port connecting two adjacent series UTLM nodes. The subscripts $_L$ and $_R$ represent the left side and the right side, and the subscripts $_i$ and $_j$ represent the index of each triangle edge within each triangle. V_m denotes the voltage at the middle of this port.

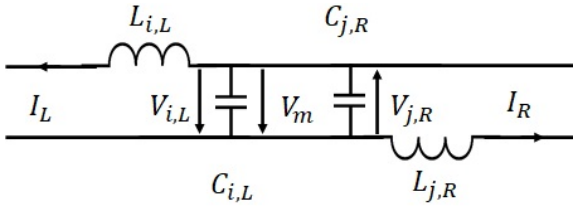

Fig. 4.4.2: A port connecting adjacent 2D series nodes in unstructured TLM

The mappings of physical quantities are given as

$$V_i \leftrightarrow E_i l_i, \qquad (4.4.1) \qquad\qquad I \leftrightarrow H_z \Delta z, \qquad (4.4.2)$$

where l_i is the length of the ith triangle edge, and Δz is the fictitious depth along the z-direction (perpendicular to the paper plane).

4.4.3 Derivation of Electrical Component Quantities

Firstly, (4.3.1) is applied to the single series UTLM node (Fig. 4.4.1). The discretised integral equation is written as

$$E_0 l_0 + E_1 l_1 + E_2 l_2 = -\mu \frac{d}{dt} \left(H_z \left(l_0 + l_1 + l_2 \right) \cdot r \cdot \frac{1}{2} \right), \tag{4.4.3}$$

where r denotes the in-radius of the triangle, and the integration direction is counter-clockwise. The coefficient $\frac{1}{2}$ is because the area of the triangle equals $\frac{1}{2}(l_0 + l_1 + l_2)r$.

Substituting the mapping relations (4.4.1) (4.4.2) into (4.4.3) gives

$$V_0 + V_1 + V_2 = -\mu \frac{d}{dt} \left(\frac{I}{\Delta z} \left(l_0 + l_1 + l_2 \right) \cdot r \cdot \frac{1}{2} \right). \tag{4.4.4}$$

Also, applying Kirchhoff's Voltage Law to this circuit model gives

$$V_0 + V_1 + V_2 = -L_{tot} \frac{dI}{dt}, \tag{4.4.5}$$

where $L_{tot} = L_0 + L_1 + L_2$.

Comparing (4.4.4) with (4.4.5) yields

$$L_{tot} = \frac{\mu \left(l_0 + l_1 + l_2 \right) \cdot r}{2 \Delta z}. \tag{4.4.6}$$

This total inductance is then split to each triangle edge, giving

$$L_i = \mu \frac{l_i r}{2}, \tag{4.4.7}$$

where the subscript $_i$ denotes the edge index. $\Delta z = 1$ is taken without loss of generality.

Then, (4.3.2) is applied to the port (Fig. 4.4.2), and the integration surface is

chosen as the vertical rectangle defined by the segment connecting two node centres and the fictitious z-direction. The discretised integral equation is written as

$$(H_L - H_R)\,\Delta z = \varepsilon \frac{d}{dt}\left(E\,(\Delta_L + \Delta_R)\,\Delta z\right), \tag{4.4.8}$$

where H_L and H_R denote the H_z at the left and the right side, and Δ_L and Δ_R represent the distance to the port from the left node centre and the right node centre respectively.

Substituting the mapping relations (4.4.1) (4.4.2) into (4.4.8) gives

$$I_L - I_R = \varepsilon \frac{d}{dt}\left(\frac{V_i}{l_i}\,(\Delta_L + \Delta_R)\,\Delta z\right). \tag{4.4.9}$$

Also, applying Kirchhoff's Current Law to this circuit model gives

$$I_L - I_R = C_{tot}\frac{dV_m}{dt}, \tag{4.4.10}$$

where $C_{tot} = C_0 + C_1 + C_2$. Note that $V_m = V_{i,L} = -V_{j,R}$.

Comparing (4.4.9) with (4.4.10) yields

$$C_{tot} = \varepsilon \frac{(\Delta_L + \Delta_R)\,\Delta z}{l_i}. \tag{4.4.11}$$

This total capacitance is then split to each node, and again $\Delta z = 1$ is taken.

$$C_i = \varepsilon \frac{\Delta_i}{l_i}, \tag{4.4.12}$$

where Δ_i represents the centre-port distance within an individual triangle, and the subscript $_i$ denotes the edge index within an individual triangle.

4.4.4 Time Step and The Position of the Port

The inductors are modelled as links. The impedance of a link inductor [57] is

$$Z_L = \frac{L}{\Delta t/2}, \tag{4.4.13}$$

with an associated error capacitance [57] of

$$C_e = \frac{(\Delta t/2)^2}{L}. \tag{4.4.14}$$

where Δt is the simulation time step, and $\Delta t/2$ is the single trip time on the link.

The capacitors are modelled as stubs, but the stub capacitance should compensate the error capacitance of link inductors in order to reduce errors. Therefore, stub capacitance is calculated as

$$C_s = C_i - C_e = \frac{\varepsilon \Delta_i}{l_i} - \frac{2\,(\Delta t/2)^2}{\mu l_i r}. \tag{4.4.15}$$

The stability condition of the two-dimensional UTLM method requires positive stub capacitance. Therefore, $C_s \geq 0$ gives

$$\Delta t^2 \leq 2\mu\varepsilon\Delta_i r. \tag{4.4.16}$$

To find the optimal position of the port, we need to maximise the minimum between $\Delta_L r_L$ and $\Delta_R r_R$. Since we know the distance between two adjacent node centres (denoted as Δ_{PQ}) is constant

$$\Delta_L + \Delta_R = \Delta_{PQ}, \tag{4.4.17}$$

the optimal position of the port should satisfy

$$\Delta_L r_L = \Delta_R r_R. \tag{4.4.18}$$

Following this relation, Δ_L and Δ_R are obtained as

$$\Delta_L = \frac{r_R}{r_L + r_R}\Delta_{PQ}, \tag{4.4.19}$$

$$\Delta_R = \frac{r_L}{r_L + r_R}\Delta_{PQ}. \tag{4.4.20}$$

In this way, the upper bound of $\min\{\Delta_L r_L, \Delta_R r_R\}$ is obtained as

$$\min\{\Delta_L r_L, \Delta_R r_R\} \leq \Delta_{PQ} \frac{r_L r_R}{r_L + r_R}, \tag{4.4.21}$$

and hence, the maximum simulation time step is

$$\Delta_{t,max} = \sqrt{2\mu\varepsilon \cdot \min_{\text{all triangles}} \left\{ \Delta_{PQ} \frac{r_L r_R}{r_L + r_R} \right\}}. \tag{4.4.22}$$

4.4.5 Scattering and Connection

Similar to the scattering and connection process of the classic Cartesian TLM method for series nodes, the equivalent circuit within nodes and the equivalent circuit at ports are solved alternately. Fig. 4.4.3 shows the equivalent circuit within a single series node, where the inductors are modelled as links and replaced by their Thévenin voltage sources with corresponding impedance; the superscript ^{i} represents the incident voltage.

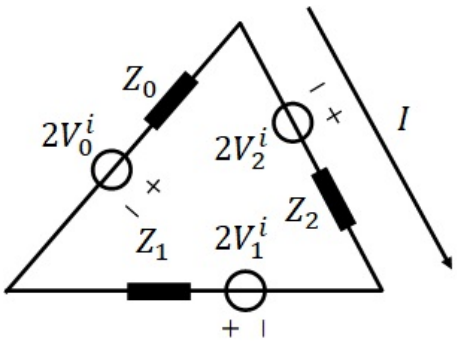

Fig. 4.4.3: Thévenin equivalent circuit of a single series node

Solving this circuit gives the loop current

$$I = \frac{2\left(V_0^i + V_1^i + V_2^i\right)}{Z_0 + Z_1 + Z_2}. \tag{4.4.23}$$

The reflected voltages are obtained by subtracting the incident voltage from the total voltage; the superscript ^{r} represents the reflected voltage.

$$V_0^r = \left(2V_0^i - Z_0 I\right) - V_0^i = V_0^i - Z_0 I \tag{4.4.24}$$

$$V_1^r = \left(2V_1^i - Z_1 I\right) - V_1^i = V_1^i - Z_1 I \tag{4.4.25}$$

$$V_2^r = \left(2V_2^i - Z_2 I\right) - V_2^i = V_2^i - Z_2 I \tag{4.4.26}$$

Fig. 4.4.4 shows the Thévenin equivalent circuit at a port, where the subscript $_s$ refers to the capacitive stubs. Note that the voltage direction of the right side transmission-line is different from that of the left side, and this is because the same capacitor voltage is defined in different directions by adjacent triangles (Fig. 4.4.2); for a certain edge shared between two triangles, the counter-clockwise direction defined by one triangle is opposite to the counter-clockwise direction defined by the other triangle.

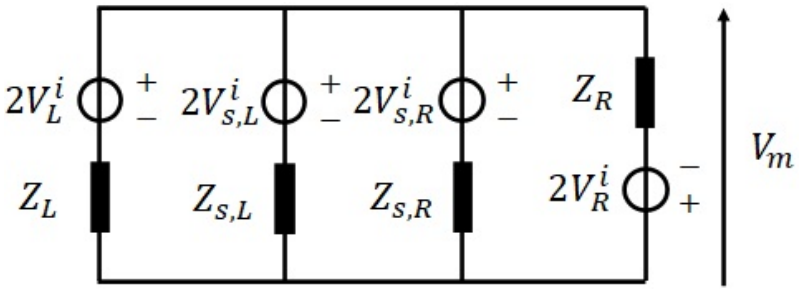

Fig. 4.4.4: Thévenin equivalent circuit at a port

Solving this circuit gives the middle voltage

$$V_m = \frac{2\left(\dfrac{V_L^i}{Z_L} + \dfrac{V_{s,L}^i}{Z_{s,L}} + \dfrac{V_{s,R}^i}{Z_{s,R}} - \dfrac{V_R^i}{Z_R}\right)}{\dfrac{1}{Z_L} + \dfrac{1}{Z_{s,L}} + \dfrac{1}{Z_{s,R}} + \dfrac{1}{Z_R}}, \tag{4.4.27}$$

and the reflected voltages are calculated as follows

$$V_L^r = V_m - V_L^i, \tag{4.4.28}$$

$$V_R^r = (-V_m) - V_R^i, \tag{4.4.29}$$

$$V_{s,L}^r = V_m - V_{s,L}^i, \tag{4.4.30}$$

$$V_{s,R}^r = V_m - V_{s,R}^i. \tag{4.4.31}$$

In the connection process, the reflected voltages from the ports become the incident voltages to the node centres, and the reflected voltages from node centres become the incident voltages to the ports. The reflected voltages from the stubs become the incident voltages of themselves in the next iteration because they are capacitive stubs [57].

4.4.6 Cylindrical Resonator Validation Test

The cylindrical resonator test is used to validate the series version of the two-dimensional UTLM method. In this test, the resonator is assumed to be a cylinder with an infinite height so that a two-dimensional simulation can be applied to its circular cross-section. The medium inside is set as vacuum, and the boundary is set as a perfect electrical conductor.

The radius of the cylindrical resonator is set to $a = 1$ m. An initial loop current of 1 A is applied at simulation time $t = 0$ s as the initial condition to represent a unit impulse input, and the input point is a single arbitrary triangular node other than the cylinder origin. Simulations are run for a sufficiently long time so that the waves inside the resonator almost reach the steady state resonance. The time series of the field component H_z at an arbitrary fixed point is measured and recorded, and the discrete Fourier transform is applied to this time series after the simulation to reveal its frequency components.

This simulation focuses on TE modes, and the TE resonant frequencies of the circular resonator are given as [48]

$$f_{TEnp} = \frac{h_{TEnp}}{2\pi\sqrt{\varepsilon\mu}}, \tag{4.4.32}$$

where $(h_{TEnp} \cdot a)$ equals the pth zero of the first-order derivative (J'_n) of the Bessel function (J_n).

Optimal Delaunay triangulation meshes with different numbers of triangles are used to discretise the circle of radius $a = 1$ m, and the resonant frequencies obtained from simulations using different mesh densities are collected in Table 4.4.1. Fig. 4.4.5 plots the relative error between the analytical solution and the numerical solution as a function of average link-line length (Δ). As is shown, the error reduces as the mesh becomes finer, and the slopes of the trendlines indicate that this series UTLM method has a spatial accuracy of approximately second order.

Table 4.4.1: Resonant frequency (Unit: 10^8 Hz) of each mode obtained by the 2D TE series UTLM method

	TE11	TE21	TE01	TE12
Analytical Result	0.8784	1.4572	1.8284	2.5436
UTLM (112 Triangles)	0.8816	1.4548	1.8155	2.5473
UTLM (494 Triangles)	0.8797	1.4582	1.8257	2.5331
UTLM (1005 Triangles)	0.8796	1.4587	1.8281	2.5399
UTLM (4952 Triangles)	0.8788	1.4576	1.8283	2.5433

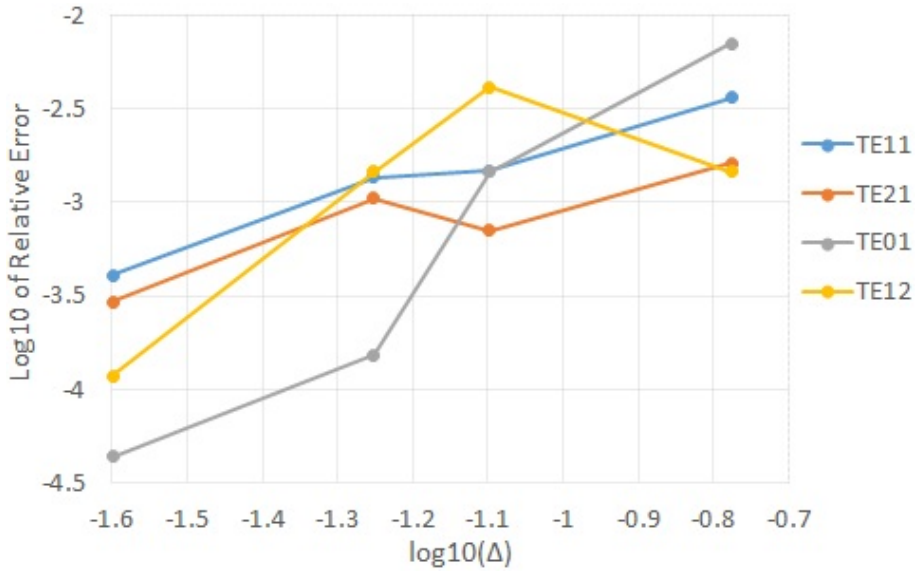

Fig. 4.4.5: Relative errors of each TE mode using different mesh densities

4.4.7 Nanotip Waveguide

The two-dimensional model of a photonic nanotip waveguide inserted into the metal (shown in Fig. 4.4.6) is used to demonstrate one application of the series UTLM method. The rectangular part of the silicon waveguide has a length of 3 μm and a width of 1 μm, and the triangular part has a base width of 0.4 μm and a length of 1 μm. The refractive index of the silicon waveguide is $n_m = 3.477$, and at the chosen operating wavelength $\lambda = 1.55$ μm, its effective refractive index is $n_{eff} = 3.3917$.

The fundamental mode of the dielectric waveguide is chosen as the excitation function, which is implemented at the left boundary of this model. Note that the photonic mode has H_z and E_y as the dominant field components. The magnetic

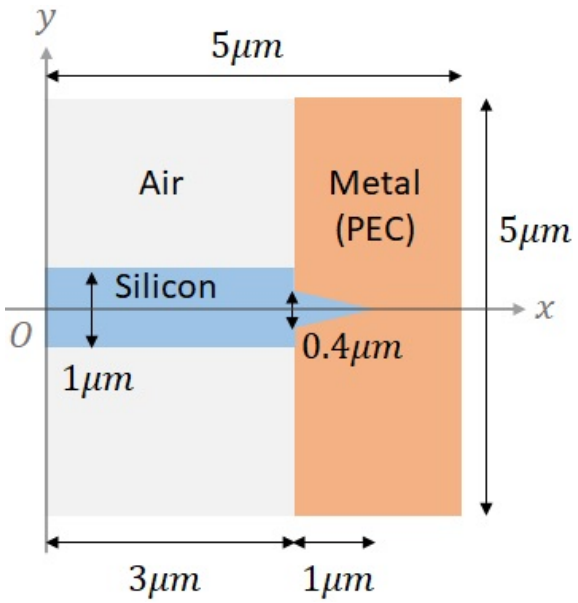

Fig. 4.4.6: A schematic of a nanotip waveguide taper inserted into the metal

field excitation function is given as

$$H_z(y,t) = H_z^0(y) \cdot \sin\left(2\pi \frac{c_0}{\lambda} \cdot t\right), \tag{4.4.33}$$

where

$$H_z^0(y) = \begin{cases} \cos(K_n d_0) \exp(-\gamma_c (y - d_0)) & y > d_0 \\ \cos(K_n y) & -d_0 \le y \le d_0 \\ \cos(K_n d_0) \exp(\gamma_c (y + d_0)) & y < -d_0 \end{cases}, \tag{4.4.34}$$

$K_n = \frac{2\pi}{\lambda}\sqrt{n_m^2 - n_{eff}^2}$, $\gamma_c = \frac{2\pi}{\lambda}\sqrt{n_{eff}^2 - n_c^2}$, $c_0 = 1/\sqrt{\mu_0 \varepsilon_0}$, $n_c = 1$, and $d_0 = 0.5 \times 10^{-6}$m.

The stop time is chosen as $t_{stop} = 5.496 \times 10^{-14}$s, and the magnetic field in the z-direction (H_z) obtained by the series UTLM method is shown in Fig. 4.4.7. Approximately 40000 triangles are used to mesh the computational domain, and the Cartesian series TLM method using 250-by-250 rectangles is used to validate and compare with the series UTLM method. The time step used in this simulation for both algorithms was $\Delta t = 3.59974 \times 10^{-18}$s. It can be seen by comparing Fig. 4.4.7a and Fig. 4.4.7b that the unstructured algorithm can significantly reduce the staircase effect when the geometrical boundary is not aligned with the coordinate axes, and

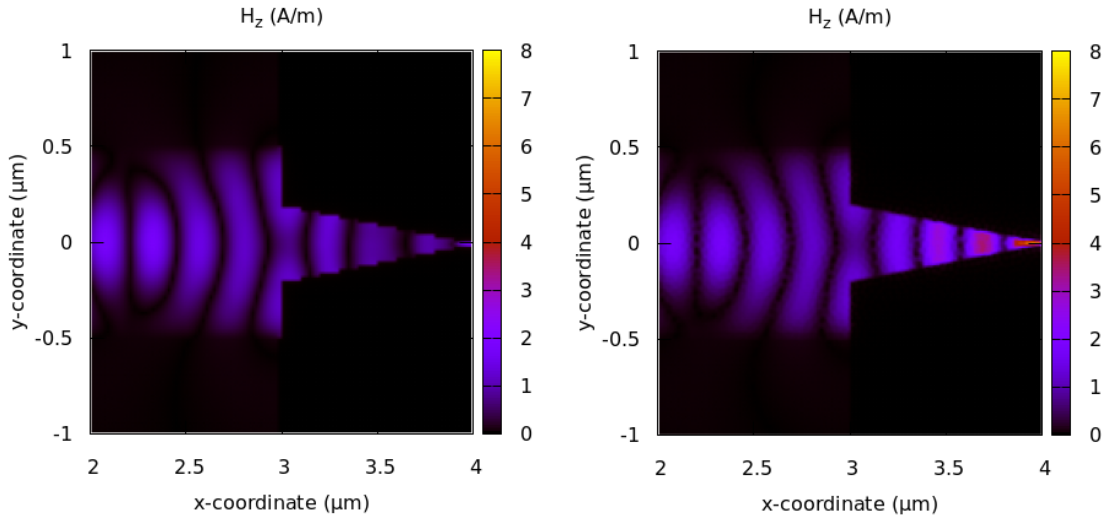

(a) (b)

Fig. 4.4.7: Comparison of the $|H_z|$ profile obtained from (a) structured Cartesian cells (b) unstructured triangular cells. $t_{stop} = 5.496 \times 10^{-14}$s.

the field pattern at the tip of the triangle can be described more clearly by the series UTLM algorithm.

4.4.8 Field Components Extraction

Different from the 2D TE Cartesian TLM method in which the electric field components E_x and E_y are explicitly mapped as V_x and V_y at the ports of each individual node, the 2D TE unstructured TLM method does not directly record these pair of orthogonal components. To extract these orthogonal components, one way is to deliberately set up a triangle element in the mesh which has an edge parallel to the target field component (i.e. x-direction or y-direction) at the target measurement point, but it is not possible to obtain the target field component at all nodes using a single mesh without turning the mesh back to Cartesian in essence. Therefore, an effective way to extract E_x and E_y for an arbitrary UTLM node is proposed as follows.

The port voltage, according to the UTLM formulation $V_i \leftrightarrow \boldsymbol{E} \cdot \boldsymbol{l_i}$, is the dot product of the electric field with the corresponding triangle edge vector. Clockwise direction within each triangle (shown in Fig. 4.4.8) is assumed without loss of generality. Since we have only two unknowns but three ports, which lead to three equations, the least squares method is used here to evaluate the E_x and E_y

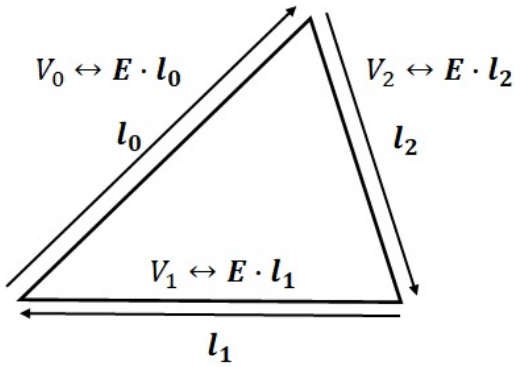

Fig. 4.4.8: In the 2D TE UTLM method, the dot product of $\boldsymbol{E}$ with the triangle edge vector is mapped to the port voltage. V_i $(i = 0, 1, 2)$ is the port voltage, and $\boldsymbol{l}_i$ $(i = 0, 1, 2)$ is the triangle edge vector.

components of the electric field $\boldsymbol{E}$.

The difference D_i is defined as

$$D_i = \boldsymbol{E} \cdot \boldsymbol{l_i} - V_i = E_x l_{i,x} + E_y l_{i,y} - V_i, \tag{4.4.35}$$

where $\boldsymbol{l_i}$ is explicitly written as $(l_{i,x}, l_{i,y})$.

The sum of the squared differences is then

$$S = \sum_{i=0}^{n-1} D_i^2 = \sum_{i=0}^{n-1} (E_x l_{i,x} + E_y l_{i,y} - V_i)^2, \tag{4.4.36}$$

where n is the number of ports associated with a node.

To minimise the sum S, we let $\partial S/\partial E_x = 0$ and $\partial S/\partial E_y = 0$, which leads to

$$\begin{pmatrix} \sum l_{i,x}^2 & \sum l_{i,x} l_{i,y} \\ \sum l_{i,x} l_{i,y} & \sum l_{i,y}^2 \end{pmatrix} \begin{pmatrix} E_x \\ E_y \end{pmatrix} = \begin{pmatrix} \sum l_{i,x} V_i \\ \sum l_{i,y} V_i \end{pmatrix}, \tag{4.4.37}$$

and the fitted (E_x, E_y) is obtained then using

$$\begin{pmatrix} E_x \\ E_y \end{pmatrix} = \begin{pmatrix} \sum l_{i,x}^2 & \sum l_{i,x} l_{i,y} \\ \sum l_{i,x} l_{i,y} & \sum l_{i,y}^2 \end{pmatrix}^{-1} \begin{pmatrix} \sum l_{i,x} V_i \\ \sum l_{i,y} V_i \end{pmatrix}. \tag{4.4.38}$$

Fig. 4.4.9 demonstrates the effectiveness of the least squares method to extract the orthogonal components of the electric field strength.

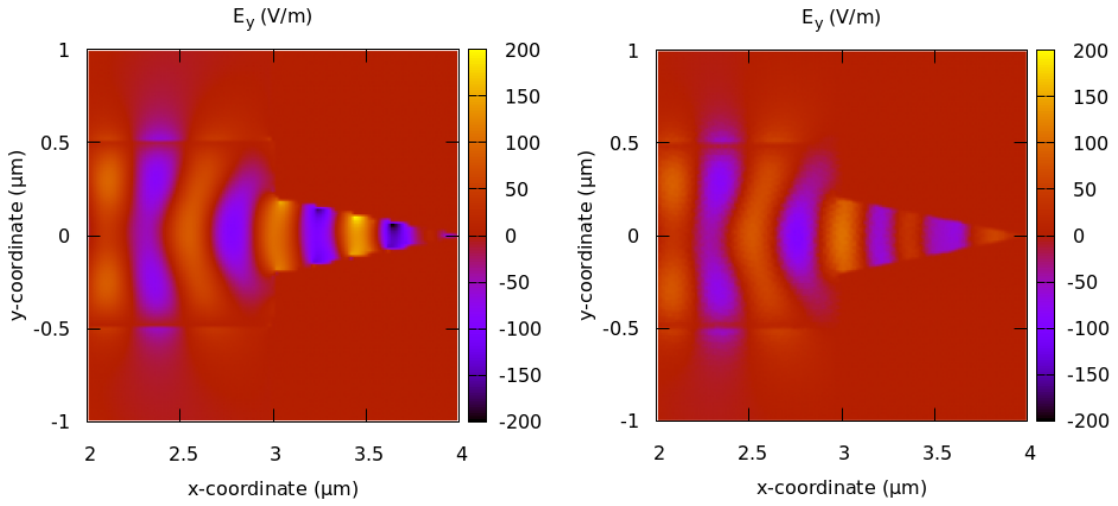

(a) (b)

Fig. 4.4.9: Comparison of the E_y profile obtained from (a) structured Cartesian cells (b) unstructured triangular cells. $t_{stop} = 5.496 \times 10^{-14}$s.

4.5 Mesh Optimisation

The mesh optimisation in this context refers to providing a larger global time step for the unstructured TLM simulation. Since the maximum time step is limited by the shortest length of link lines, the optimisation is therefore intended to separate the Voronoi vertices evenly so that no exceedingly short link line is expected. Two kinds of optimised meshes, namely the centroidal Voronoi tessellation (CVT) [80] and the optimal Delaunay triangulation (ODT) [81], are described here, both of which can be obtained via using iterative algorithms.

- (CVT) In the CVT mesh, every Delaunay vertex is located at the centroid of its local Voronoi polygon that contains it. The iterative algorithm to turn an ordinary Delaunay mesh into a CVT is known as the Lloyd's algorithm [82], which repeats to move every Delaunay vertex to the centroid of its local Voronoi polygon and then redo the Delaunay triangulation using new vertices until the overall displacement is less than certain threshold.

- (ODT) In the ODT mesh, every Delaunay vertex is located at the weighted average of its adjacent circumcentres. All triangles that use this vertex are considered as adjacent, and the weight equals the area of an individual adjacent triangle divided by the total area of all adjacent triangles. Similarly to the

CVT, an iterative algorithm is used to achieve an ODT. It repeats to move every Delaunay vertex to its corresponding weighted average point and then redo the Delaunay triangulation using new vertices until the total displacement is less than certain threshold.

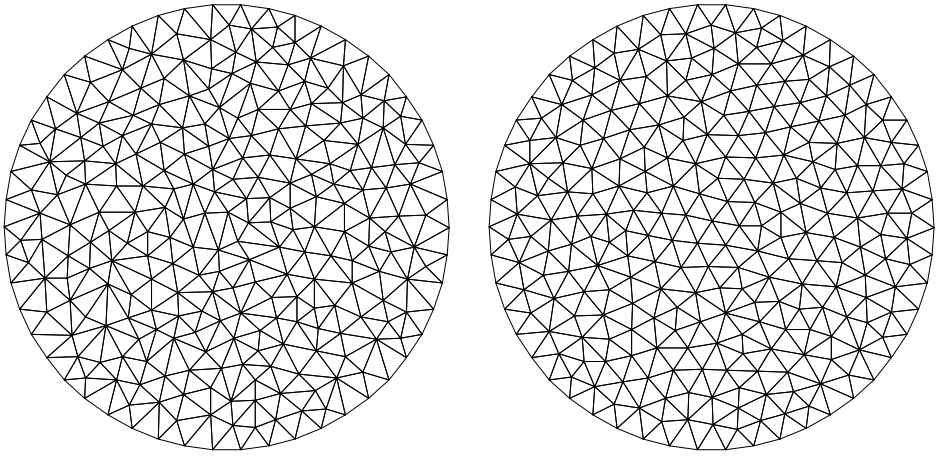

(a) (b)

Fig. 4.5.1: Comparison between the mesh (a) before ODT iterations and (b) after 500 ODT iterations. Both meshes have 494 triangles.

In this thesis, the ODT algorithm is chosen because of its straightforward implementation with matched effectiveness against CVT [83]. Fig. 4.5.1 compares the Delaunay mesh before and after the ODT iterations. The geometry domain is a unit circle with a radius of 1 m. Fig. 4.5.1a is the Delaunay mesh generated directly by Shewchuk Triangle [72] code, and Fig. 4.5.1b shows the optimised Delaunay mesh after 500 ODT iterations. Clearly, triangles in the mesh after ODT iterations tend to have similar shapes and sizes. This can also be seen in Fig. 4.5.2 that counts the link-line lengths of two meshes. Both meshes have 494 triangles, but the minimum link-line length increased from 0.000278621 m to 0.00187498 m (one order of magnitude up) after using the ODT algorithm. Note that the values 0.000278621 m and 0.00187498 m were obtained from direct measurements of the numerical simulation rather than visually from Fig. 4.5.2.

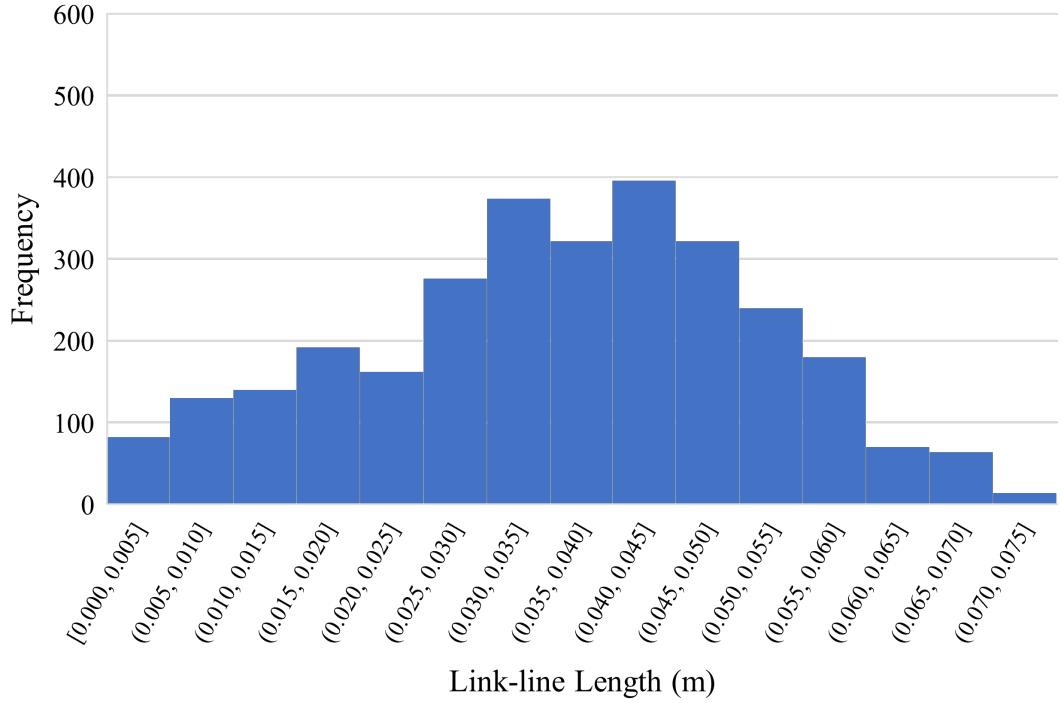

(a)

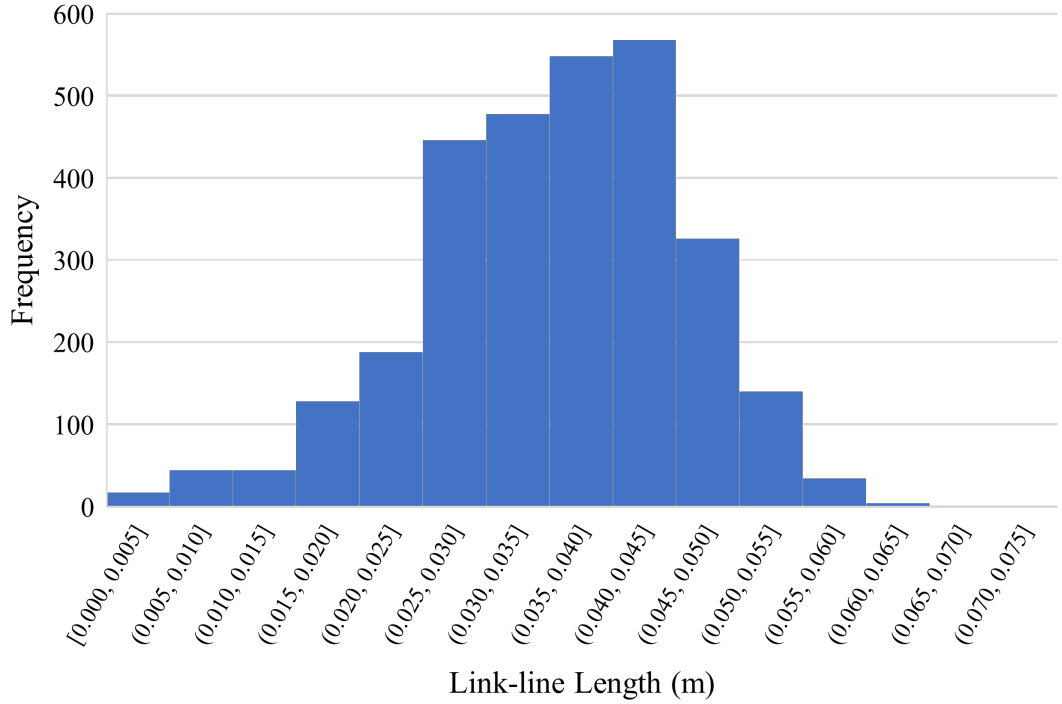

(b)

Fig. 4.5.2: The distributions of resultant link-line lengths (a) before ODT iterations and (b) after 500 ODT iterations

4.6 Remarks on using the Delaunay Mesh

In two-dimension, the derivations proposed in this thesis based on Delaunay triangular meshes will not be undermined as long as the circumcentre P does not go beyond (cross over) the circumcentre Q (see Fig. 4.6.1) because the idea of the UTLM in 2D is essentially to relate one point with its three 'well-posed' neighbouring points, and it is not fixated on the triangulation itself. The circumcentre P is guaranteed not to go beyond the circumcentre Q because the mesh is `conforming Delaunay`. In addition, the optimal Delaunay triangulation (ODT) iterative algorithm mentioned in Section 4.5 is useful to make triangles tend to have similar shapes; this can to a large extent hold the circumcentre P inside the triangle ABC, or at least not go too far inside the triangle ACD.

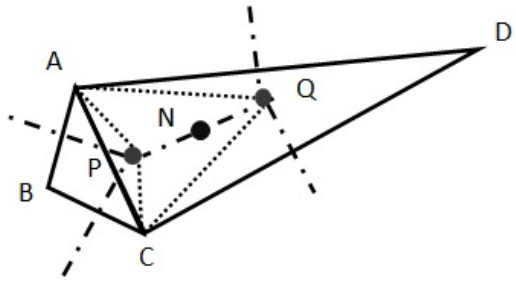

Fig. 4.6.1: The 2D UTLM is still valid when the circumcentre is outside the triangle.

4.7 Conclusion

The 2D EM UTLM methods covered in this chapter use Delaunay meshes to discretise the problem geometry space, and for the TM version and the TE version, they only involve different equivalent circuit to solve during the scattering and connection process. The characteristics of the Delaunay triangular mesh and its triangulation process have been covered. The classic TM shunt UTLM method has been derived in an alternative way using the integral form of Maxwell's equations, and following a similar idea, the TE series UTLM method has been developed. The newly-proposed TE series UTLM method has been validated using the canonical cylindrical resonator test; it is then applied to simulate the wave propagation in a tip-shaped waveguide, showing its capability to handle complex problem geometry.

The positions of the ports are carefully chosen (see (4.4.22)) in the proposed TE UTLM method in order to achieve a larger time step. The ODT algorithm can be used in the UTLM methods to optimise the mesh and increase the simulation time step.

Chapter 5

Two-dimensional Thermal UTLM

This chapter introduces the newly-developed 2D thermal UTLM method through first presenting the mapping of the 2D heat diffusion parameters to the transmission-line parameters and then describing the scattering and connection process at node centres and ports. Next, the convergence and the accuracy of this 2D thermal UTLM method is investigated; a canonical test of the heat flow in a 2D square domain is conducted, and the accuracy is compared against the explicit Cartesian five-point finite difference scheme. Finally, the thermal UTLM method is applied to characterise the temperature distribution on a power transistor with a heat sink.

5.1 Overview

As the problem space becomes complex, unstructured (e.g. triangular or tetrahedral) meshes are preferred to describe the geometry because of their capability to reduce staircase effects at curved material interfaces and boundaries. The application of the thermal unstructured TLM method on the bio-heat thermal diffusion modelling has been reported in [64], where the bio-energy equation was solved numerically; however, a non-Delaunay finite element mesh (Gmsh [84]) was used for space discretisation, which leads to two consequences: (a) The mesh is not optimally Delaunay and is prone to sliver triangles that typically cause numerical instabilities, and (b) the link lines in the formulation along which the heat flux

propagates are not perpendicular to triangle edges. This discrepancy is assumed to be small, but then small and regular-shaped triangles are generally required, which is a limitation that affects not only the stability but also nonphysical dissipation, memory usage and accuracy (reported errors greater than 0.5% when compared against the analytical solution [64]).

The aim of this chapter is to develop the two-dimensional (2D) thermal version of the unstructured TLM method based on an optimal Delaunay triangular (ODT) mesh. The Delaunay mesh maximises the minimum angle among all triangles in the mesh and thus avoids the sliver triangles that typically occur in any practical mesh and cause numerical instabilities [72]. The optimal Delaunay triangulation (ODT) algorithm is applied after the initial Delaunay mesh generation to optimise the minimum link-line length. The recommended time step is related to the minimum link-line length in the mesh, which in many practical situations can be close to zero. In order to increase the simulation time step, a standard approach in the UTLM is to coalesce small cells with link-line lengths below a specified clustering threshold into a large cell in which scatterings and connections are solved implicitly, and it is applied after the ODT. This approach can increase the time step by one order of magnitude [71, 85].

The thermal UTLM proposed in this chapter shares the same Delaunay and Voronoi meshes with the EM UTLM so that during the two-way coupling process, the re-sampling of the field profile is not needed. This makes it ideally suitable for the modelling of coupled electrothermal problems.

5.2 Theory of Thermal UTLM

5.2.1 Derivation of Electrical Component Quantities

In this section, we map the diffusion parameters onto the electric circuit parameters using the two-dimensional Delaunay [72] triangular mesh. Circumcentres of the Delaunay triangles are chosen as computational node centres, and adjacent node centres are connected by Voronoi [73] edges. The Voronoi mesh edges become

the transmission-line network along which signals propagate. Fig. 5.2.1 shows two triangles with vertices A, B, C and D. The node centres P and Q are connected by the Voronoi mesh which also connects them to other neighbouring nodes. Point N represents the port connecting these two node centres and is positioned at the midpoint between P and Q. X and Y are the midpoints of PN and QN respectively, and they are used later in the midpoint rule approximation. The length of both PN and QN are guaranteed to be positive by the Delaunay mesh.

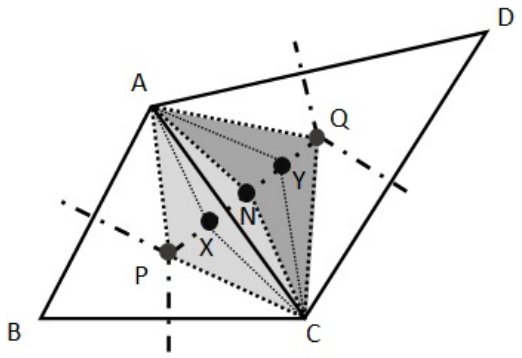

Fig. 5.2.1: Triangle ABC and triangle ADC are Delaunay triangles. P and Q are circumcentres as computational node centres. N is the port connecting two adjacent nodes. Dot-dashed lines are Voronoi edges. X and Y are the **midpoints** of PN and QN respectively.

In the thermal TLM convention [57], the temperature is analogous to the voltage:

$$V \leftrightarrow T. \tag{5.2.1}$$

The total two-dimensional heat fluxes $\boldsymbol{F} \equiv (F_x, F_y, 0)$ out of the quadrilateral $AXCY$ from $\overline{AXC}$ (denoted as left boundaries in this context) and $\overline{AYC}$ (denoted as right boundaries) are mapped to the analogous current I_L and I_R respectively, which are defined as (5.2.2) and (5.2.3), where $\widehat{\boldsymbol{n_0}}$ is the normal vector of the edge AC facing towards P (without loss of generality), and $\Delta l = |\overrightarrow{AC}|$. $\boldsymbol{G_L}$ and $\boldsymbol{G_R}$ are the equivalent uniform temperature gradients to give the same two-dimensional heat flowing out of two boundaries respectively, and this is to cope with the integral forms of the heat diffusion equations. Note that the subscripts $_L$ and $_R$ denote the

left side (triangle ABC) and the right side (triangle ACD) respectively.

$$\begin{aligned} I_L \leftrightarrow & \int_C^X (\boldsymbol{F} \cdot \hat{\boldsymbol{n}})\, dl + \int_X^A (\boldsymbol{F} \cdot \hat{\boldsymbol{n}})\, dl \\ & = -k_{th,L} \left(\boldsymbol{G_L} \cdot \widehat{\boldsymbol{n_0}}\right) \Delta l \end{aligned} \tag{5.2.2}$$

$$\begin{aligned} I_R \leftrightarrow & \int_A^Y (\boldsymbol{F} \cdot \hat{\boldsymbol{n}})\, dl + \int_Y^C (\boldsymbol{F} \cdot \hat{\boldsymbol{n}})\, dl \\ & = -k_{th,R} \left(\boldsymbol{G_R} \cdot -\widehat{\boldsymbol{n_0}}\right) \Delta l \end{aligned} \tag{5.2.3}$$

The integral forms of (3.1.2) and (3.1.3) are presented as (5.2.4) and (5.2.5) respectively.

$$\int_a^b \boldsymbol{F} \cdot d\boldsymbol{l} = -k_{th} \int_a^b \nabla T \cdot d\boldsymbol{l} = -k_{th} \left[T\right]_a^b \tag{5.2.4}$$

$$\frac{d}{dt} \iiint_V Q \cdot dV + \oiint_{\partial V} \boldsymbol{F} \cdot d\boldsymbol{A} = \iiint_V Q_{VS}\, dV \tag{5.2.5}$$

We choose the midpoint of PQ as the position of the port, and we firstly apply (5.2.4) from point N to point P. $\boldsymbol{G_L}$ is used to approximate the average temperature gradient along $\overrightarrow{NP}$.

$$\int_N^P \boldsymbol{F} \cdot d\boldsymbol{l} \approx -k_{th,L} \left(\boldsymbol{G_L} \cdot \widehat{\boldsymbol{n_0}}\right) |\overrightarrow{NP}| = -k_{th,L} \left(T_P - T_N\right) \tag{5.2.6}$$

Substituting (5.2.2) and (5.2.1) into (5.2.6) yields.

$$I_L \frac{|\overrightarrow{NP}|}{k_{th,L} \Delta l} = -\left(V_P - V_N\right). \tag{5.2.7}$$

According to $IR = -\Delta V$, the analogous resistance R_L is expressed as (5.2.8), where $\Delta_L = |\overrightarrow{NP}|$. Similarly, we apply (5.2.4) from point N to point Q to get the analogous resistance R_R, where $\Delta_R = |\overrightarrow{NQ}|$.

$$R_L = \frac{\Delta_L}{k_{th,L} \Delta l} \tag{5.2.8}$$

$$R_R = \frac{\Delta_R}{k_{th,R} \Delta l} \tag{5.2.9}$$

Applying (5.2.5) to the volume with the cross-section $AXCY$ gives (5.2.10),

where Δz represents the fictitious unit length perpendicular to the paper plane.

$$\begin{aligned}\frac{d}{dt}\left(\left(Q_L\frac{|\overrightarrow{XN}|}{2}+Q_R\frac{|\overrightarrow{YN}|}{2}\right)\Delta l\Delta z\right)+\left(\oint_{AXCY}(\boldsymbol{F}\cdot\widehat{\boldsymbol{n}})\,dl\right)\Delta z \\ =\left(Q_{VS,L}\frac{|\overrightarrow{XN}|}{2}\Delta l+Q_{VS,R}\frac{|\overrightarrow{YN}|}{2}\right)\Delta z\end{aligned} \tag{5.2.10}$$

The area is calculated according to the fact that as a segment connecting two circumcentres, PQ perpendicularly bisects AC. Note that although the temperature T_N at the port N is not the same as the weighted average temperature of the quadrilateral $AXCY$, it is an adequate first-order approximation.

Substituting (5.2.1), (5.2.2), (5.2.3) and (3.1.1) into (5.2.10) yields

$$\begin{aligned}I_L+I_R=-\left(c_{p,L}\ \rho_{m,L}\frac{|\overrightarrow{XN}|}{2}\Delta l\right)\frac{dV_N}{dt}-\left(c_{p,R}\ \rho_{m,R}\frac{|\overrightarrow{YN}|}{2}\Delta l\right)\frac{dV_N}{dt} \\ +Q_{VS,L}\frac{|\overrightarrow{XN}|}{2}\Delta l+Q_{VS,R}\frac{|\overrightarrow{YN}|}{2}\Delta l.\end{aligned} \tag{5.2.11}$$

Note that I_L flows towards node centre P, and I_R flows towards node centre Q. According to $\Delta I=-C\cdot dV/dt+I_s$, the analogous capacitance C and the analogous current source I_s are expressed as (5.2.12) and (5.2.13) if the heat flowing into the two-dimensional domain due to the heat source is mapped to the current source.

$$C_{tot}=\frac{c_{p,L}\ \rho_{m,L}|\overrightarrow{XN}|\Delta l}{2}+\frac{c_{p,R}\ \rho_{m,R}|\overrightarrow{YN}|\Delta l}{2} \tag{5.2.12}$$

$$I_{s,tot}=Q_{VS,L}\frac{|\overrightarrow{XN}|}{2}\Delta l+Q_{VS,R}\frac{|\overrightarrow{YN}|}{2}\Delta l \tag{5.2.13}$$

To share the capacitance and the current source between two adjacent nodes, they are split intentionally.

$$C_L=\frac{c_{p,L}\ \rho_{m,L}\ \Delta_L\Delta l}{2} \tag{5.2.14}$$

$$C_R=\frac{c_{p,R}\ \rho_{m,R}\ \Delta_R\Delta l}{2} \tag{5.2.15}$$

$$I_{s,L}=\frac{Q_{VS,L}\ \Delta_L\Delta l}{2} \tag{5.2.16}$$

$$I_{s,R} = \frac{Q_{VS,R}\ \Delta_R \Delta l}{2} \tag{5.2.17}$$

The transmission-line circuit for the triangular cell ABC, as is used in Fig. 5.2.1, is shown in Fig. 5.2.2. The port voltages are denoted as V_i, and other transmission-line parameters, namely R_i, C_i and $I_{s,i}$ ($i = 0, 1, 2$ denotes the edge (port) index) are obtained according to (5.2.8), (5.2.9), (5.2.14), (5.2.15), (5.2.16) and (5.2.17) as:

$$R_i = \frac{\Delta_i}{k_{th,i} \Delta l}, \tag{5.2.18}$$

$$C_i = \frac{c_{p,i}\ \rho_{m,i}\ \Delta_i \Delta l}{2}, \tag{5.2.19}$$

$$I_{s,i} = \frac{Q_{VS,i}\ \Delta_i \Delta l}{2}. \tag{5.2.20}$$

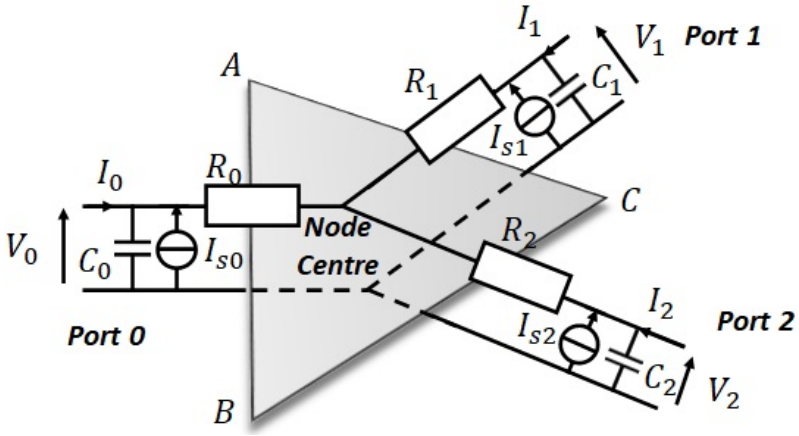

Fig. 5.2.2: Transmission-line circuit of an arbitrary triangular thermal UTLM node (Triangle ABC is the computational cell)

5.2.2 Transmission-Line Model

One UTLM node is connected to its neighbouring nodes via ports. The equivalent circuit at the port is illustrated in Fig. 5.2.3a, where R_L, R_R represent the resistance of the transmission-lines connecting two adjacent nodes, and C_L, C_R represent the capacitance of each transmission-line. The series link lines are used to replace capacitors in the thermal UTLM equivalent circuit. The characteristic impedance [57] of the capacitive series link lines is given as

$$Z_C = \frac{\Delta t/2}{C}, \tag{5.2.21}$$

and the introduced error is in the associated error inductance of this link line which is expressed as

$$L_e = \frac{(\Delta t/2)^2}{C}, \tag{5.2.22}$$

where Δt is the simulation time step, and $\Delta t/2$ is the single trip time on the link.

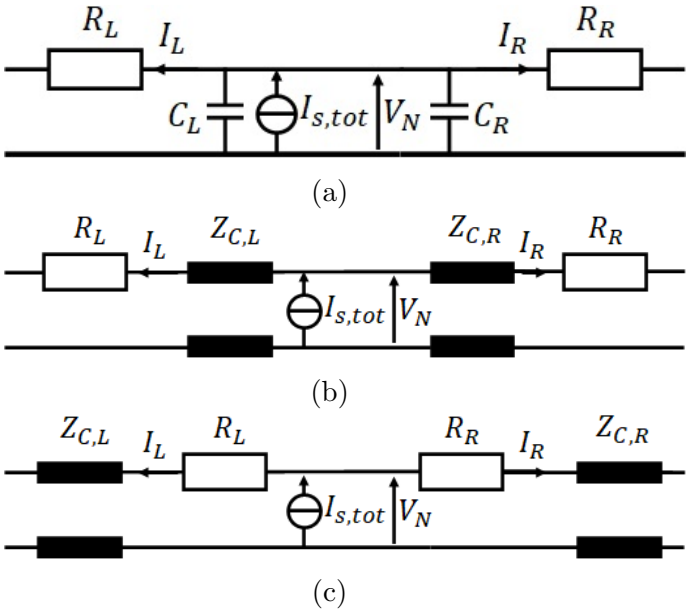

Fig. 5.2.3: (a) Transmission-line circuit at a port (b) Classic resistor-link model (c) Alternative link-resistor model

The transmission-line circuit (Fig. 5.2.3a) is turned into its resistor-link model shown in Fig. 5.2.3b, where the shunt capacitors are replaced by capacitive link lines with impedance given in (5.2.21). The position of the capacitive link line and its adjacent resistor in series could be exchanged, giving an alternative link-resistor model shown in Fig. 5.2.3c which is one of the optional ways to prevent the simulation data from excessively oscillating (known as the jump-to-zero problem [86]).

The thermal UTLM is unconditionally stable for all positive time step Δt because all electrical component quantities are positive and hence physical. One only needs to consider whether the wave behaviour is much less significant than the diffusion behaviour [57], which means that the inductive reactance ωL due to the error inductance (5.2.22) should be much less than the resistance in series (5.2.8) (5.2.9). Substituting the capacitance (5.2.14) (5.2.15) into this relationship yields

$$\omega \left(\Delta t/2\right)^2 \ll \min_{\text{all triangles}} \left\{ \frac{\Delta_i^2 c_p \rho_m}{2k_{th}} \right\}, \tag{5.2.23}$$

where ω is the frequency component of the solution, Δ_i the distance between a node centre and its port, and the subscript $_i$ denotes the edge index within a triangle.

5.2.3 Scattering and Connection

After the equivalent circuit has been set up, scatterings and connections are executed alternately following the same principle as the regular TLM [57] algorithm. The Thévenin equivalent circuits used in the scattering computation at ports and node centres are demonstrated in Fig. 5.2.4a and Fig. 5.2.4b respectively, where V_N represents the middle voltage at the port, and V_M represents the middle voltage at the node centre. $Z_{C,L}$, $Z_{C,R}$, Z_0, Z_1 and Z_2 are the characteristic impedance of link capacitors, and they are calculated with the single trip time $\Delta t/2$ as

$$Z_{C,L} = \frac{\Delta t/2}{C_L}, \qquad (5.2.24) \qquad Z_{C,R} = \frac{\Delta t/2}{C_R}, \qquad (5.2.25)$$

$$Z_0 = \frac{\Delta t/2}{C_0}, \quad (5.2.26) \qquad Z_1 = \frac{\Delta t/2}{C_1}, \quad (5.2.27) \qquad Z_2 = \frac{\Delta t/2}{C_2}. \quad (5.2.28)$$

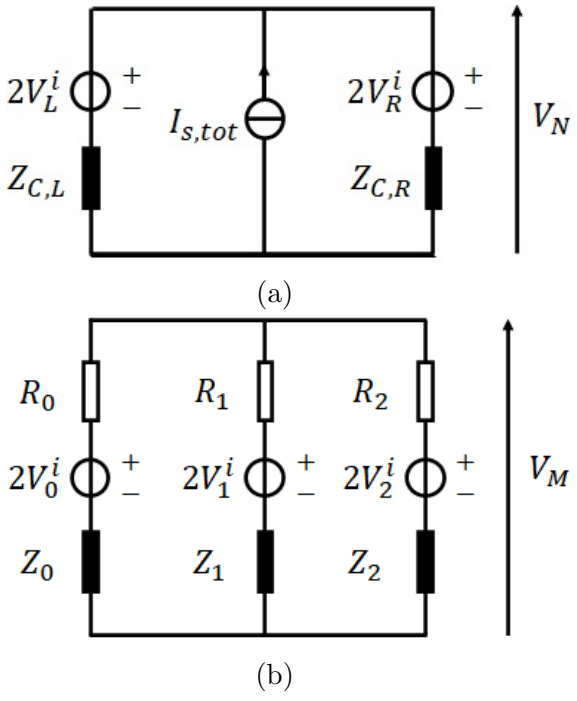

Fig. 5.2.4: Thévenin equivalent circuits used in the scattering and connection process (a) at ports (b) at node centres

By applying nodal voltage analysis to the equivalent circuit shown in Fig. 5.2.4a, the middle voltage V_N at the port is calculated as

$$V_N = \frac{I_{s,tot} + \dfrac{2V_L^i}{Z_{C,L}} + \dfrac{2V_R^i}{Z_{C,R}}}{\dfrac{1}{Z_{C,L}} + \dfrac{1}{Z_{C,R}}}. \tag{5.2.29}$$

Then, the reflected voltages are obtained by

$$V_L^r = V_N - V_L^i, \tag{5.2.30}$$

$$V_R^r = V_N - V_R^i. \tag{5.2.31}$$

In terms of the node centres, applying nodal voltage analysis to the circuit in Fig. 5.2.4b gives the middle voltage

$$V_M = \frac{\dfrac{2V_0^i}{R_0 + Z_0} + \dfrac{2V_1^i}{R_1 + Z_1} + \dfrac{2V_2^i}{R_2 + Z_2}}{\dfrac{1}{R_0 + Z_0} + \dfrac{1}{R_1 + Z_1} + \dfrac{1}{R_2 + Z_2}}. \tag{5.2.32}$$

The reflected voltages are obtained by

$$V_0^r = \left(V_M - \frac{V_M - 2V_0^i}{R_0 + Z_0} R_0\right) - V_0^i, \tag{5.2.33}$$

$$V_1^r = \left(V_M - \frac{V_M - 2V_1^i}{R_1 + Z_1} R_1\right) - V_1^i, \tag{5.2.34}$$

$$V_2^r = \left(V_M - \frac{V_M - 2V_2^i}{R_2 + Z_2} R_2\right) - V_2^i. \tag{5.2.35}$$

The connection process is simply that the reflected voltages from the ports become the incident voltages towards their adjacent node centres, and the reflected voltages from the node centres become the incident voltages towards their ports.

5.2.4 Initial Conditions and Boundary Conditions

The initial temperature can be set up by specifying the incident voltages towards either the node centres or the ports before the scattering process of the first iteration. If the incident voltages towards the ports are initialised, then the scattering at the ports should be completed before the scattering at node centres in each iteration; on the other hand, if the incident voltages towards the node centres are initialised, then

the scattering at the node centres should be done first instead. The initial incident voltage equals half of the initial temperature at the node centre in terms of quantity because the Thévenin equivalent circuit of the transmission-line has a voltage source of twice the incident voltage. If the classic resistor-link model (Fig. 5.2.3b) is used, then it is suggest that the incident voltages towards the node centre should be initialised to reduce small oscillations of the temperature during the simulation.

The boundary temperature is controlled by specifying the middle voltages at boundary ports during their scattering processes. This voltage equals the boundary temperature itself in terms of quantity and does not need to be halved.

5.2.5 Node Clustering and Mesh Optimisation

The suggested time step of the UTLM method is defined by the minimum link-line length in the mesh, i.e. PN length and QN length in Fig. 5.2.1. These lengths are always positive because P and N never cross over each other. This feature is guaranteed by the Delaunay mesh and is important for the stability of the UTLM method. In the situation where a link-line length is very small or even zero, the cell resistance will be exceedingly large and the suitable simulation time step will be prohibitively small. To alleviate this problem, two adjacent nodes that share a very short link line need to be combined into a single quadrilateral node [71], which is illustrated in Fig. 5.2.5. Although Fig. 5.2.5 shows an example using shunt nodes, this technique can be applied to series nodes as well.

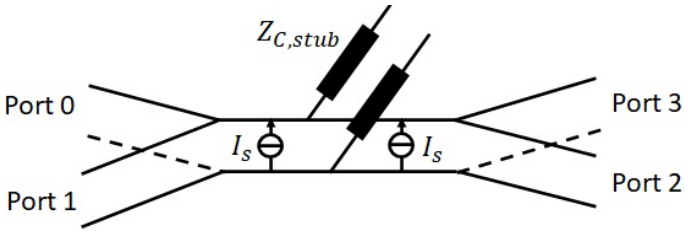

Fig. 5.2.5: Quadrilateral clustered node

A capacitive stub is used to replace the short capacitive link lines. The characteristic impedance of the capacitive stub and its associated error inductance [57] are given as

$$Z_C = \frac{\Delta t/2}{C}, \qquad (5.2.36) \qquad L_e = \frac{(\Delta t/2)^2}{C}. \qquad (5.2.37)$$

In a general Delaunay mesh, chances are that more than two triangular nodes should be combined together due to small link-line lengths in a similar manner, and this will add huge complexity to the code implementation. To mitigate this problem, it is preferred to use the optimal Delaunay triangulation (ODT) mesh [79, 81] in practice which not only averages the shape of triangles and minimises the interpolation error but also maximises the minimum link-line length [78]. When ODT is in place, only quadrilateral nodes and normal triangular nodes need to be considered as ODT eliminates the need for higher-level clustering. The ODT algorithm is described in Section 4.5 and is available in detail in [78, 81].

5.3 Results

5.3.1 Convergence Test

In this section, we evaluate the accuracy and convergence of the thermal unstructured TLM method by comparing its results against a known analytical solution. A canonical test is carried out first within a square computational domain $[-1, 1]$ (m)$\times[-1, 1]$ (m). The physical parameters are specified as $\rho_m = 1.225$ kg·m^{-3}, $k_{th} = 0.0262$ W $\cdot$ m^{-1} $\cdot$ K^{-1} and $c_p = 1.005 \times 10^3$ J $\cdot$ kg^{-1} $\cdot$ K^{-1}. No heat source is placed in the domain. The initial temperature profile is set to

$$T(x, y, 0) = 298.15 + 75 \cos\left(\frac{\pi}{2}x\right) \cos\left(\frac{\pi}{2}y\right), \qquad (5.3.1)$$

and the boundary temperature is fixed at 298.15 K. This test problem has an analytical solution given as

$$T(x, y, t) = 298.15 + 75 \cos\left(\frac{\pi}{2}x\right) \cos\left(\frac{\pi}{2}y\right) \exp\left(-\alpha\frac{\pi^2}{2}t\right), \qquad (5.3.2)$$

where $\alpha = k_{th}/(\rho_m c_p)$.

The square computational domain is triangulated using different numbers of

elements, and the ODT mesh optimisation is applied before the simulation. A constant time step of $\Delta t = 2 \times 10^{-1}$ s is used in this convergence test, and the stop time t_{stop} is set to 5×10^4 s. The thermal UTLM algorithm runs with ODT meshes of different numbers of elements respectively. The temperature at every UTLM node centre is recorded and compared with the analytical solution, and the RMS error

$$Err_{RMS} = \sqrt{\frac{\sum_{i=1}^{N} e_i^2}{N}} \tag{5.3.3}$$

is used as the criterion to assess the overall error, where e_i is the absolute error of temperature at each node centre, and N is the number of nodes.

The RMS error obtained from each mesh is plotted in Fig. 5.3.1, and as is shown, it decreases as the mesh becomes finer, i.e. as the number of triangles in the mesh increases. The local minima in Fig. 5.3.1 are because the thermal UTLM method solves diffusion equations via modelling the diffusion process as low-frequency waves in highly lossy media so that the underlying wave behaviour may cause the numerical result at a fixed measurement point to oscillate around the exact solution. It may occur at different time for different mesh resolutions because the error inductances are different for different mesh resolutions and simulation time steps (Δt) so that the underlying wave frequencies are different.

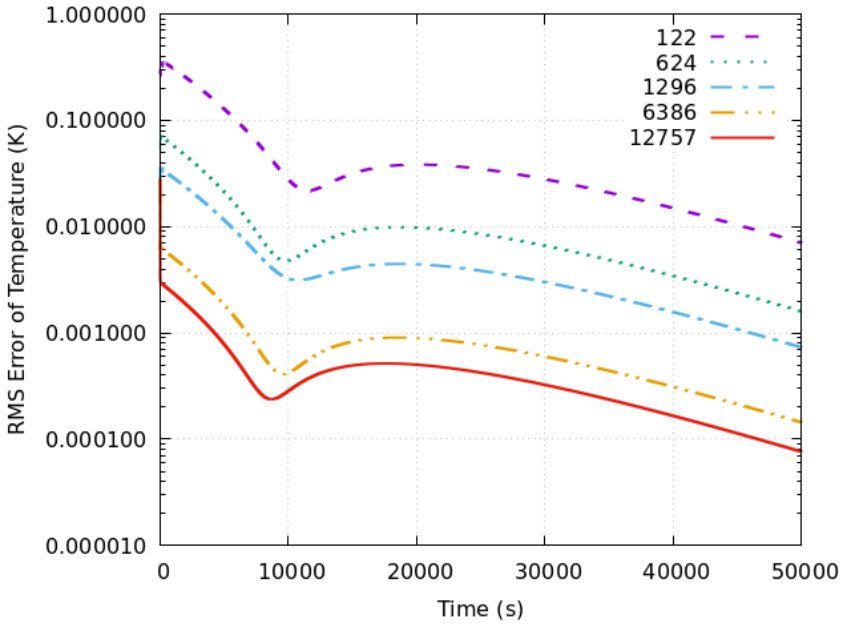

Fig. 5.3.1: RMS error of temperature obtained using different number of triangles.

Fig. 5.3.2 shows the computational domain of the problem with 122 and 1296 cells and the corresponding temperature distribution at $t_{stop} = 5 \times 10^4$ s for these two meshes. It is seen that the finer mesh provides much smoother temperature profiles.

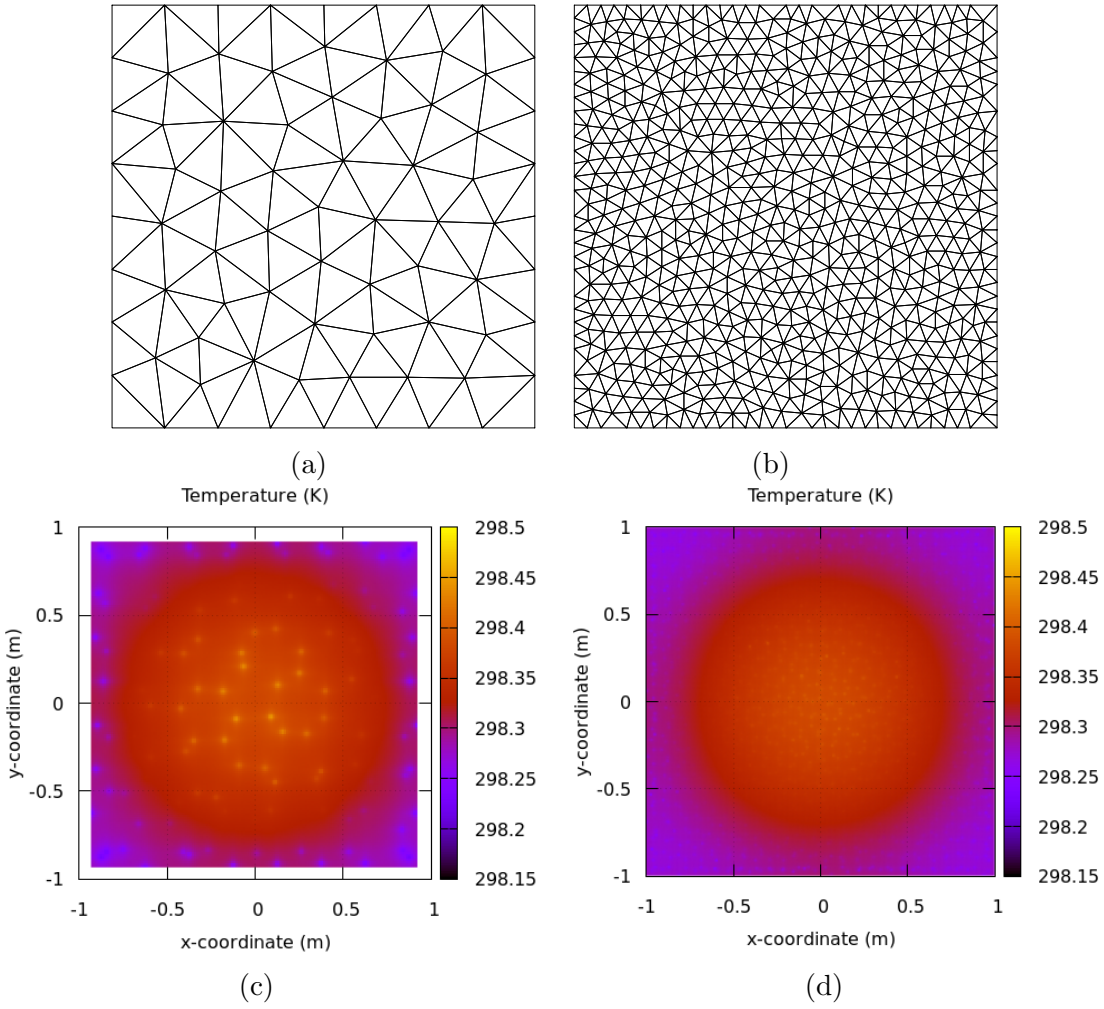

Fig. 5.3.2: ODT meshes and simulation results. (a) ODT mesh (122 triangles) (b) ODT mesh (1296 triangles) (c) Final temperature (122 triangles) (d) Final temperature (1296 triangles)

A further error analysis is shown in Fig. 5.3.3, where the RMS error at $t = 10^4$ s is plotted against the average distance between adjacent node centres (Δx) in logarithmic scale. Δx is approximated using the number of triangles and the total area of the computational domain, and it is equivalent to the average mesh element size. The gradient of the trendline in Fig. 5.3.3 confirms the second-order average local spatial accuracy of the thermal unstructured TLM (UTLM) method.

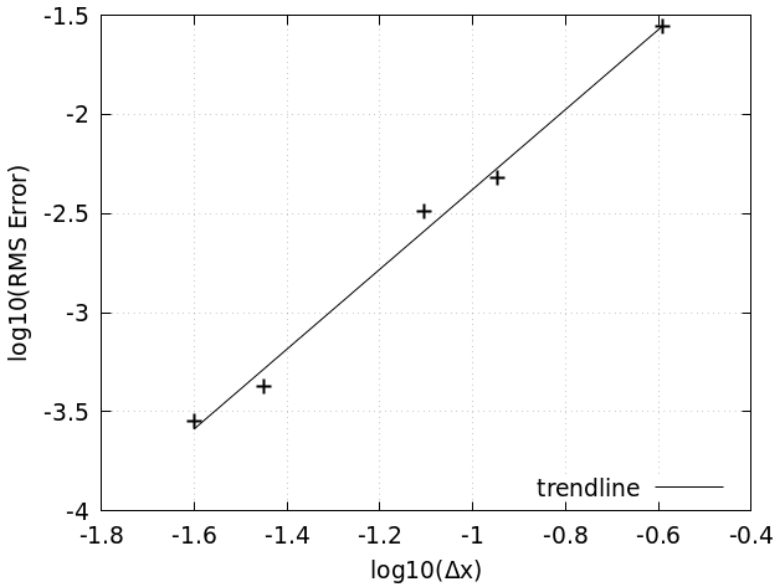

Fig. 5.3.3: RMS error at $t = 10^4$ s of different mesh resolutions in logarithmic scale

5.3.2 Mesh with Quadrilateral Combined Nodes

To test the quadrilateral combined node, structured meshes containing only isosceles right-angled triangles are deliberately created for the thermal UTLM algorithm. Every pair of isosceles right-angled triangles in a square unit become clustered, i.e. combined automatically into a quadrilateral node because their circumcentres coincide. The thermal UTLM results are compared against the fully explicit five-point finite difference scheme as

$$T_{i,j}^{n+1} = T_{i,j}^{n} + \alpha \frac{\Delta t}{\Delta x^2} \left(T_{i+1,j}^{n} + T_{i-1,j}^{n} + T_{i,j+1}^{n} + T_{i,j-1}^{n} - 4 \cdot T_{i,j}^{n} \right) \tag{5.3.4}$$

with a time step limit of

$$\frac{\alpha \Delta t}{\Delta x^2} < \frac{1}{4}. \tag{5.3.5}$$

The finite difference algorithm runs with two different grid resolutions, namely 200×200 and 400×400 Cartesian nodes, and the thermal UTLM runs with a 100×100 square-structured mesh ($20,000$ isosceles right-angled triangles). The time step used in the finite difference method is 2×10^{-2} s (under the stability condition), and the time step used in the thermal UTLM is kept as $\Delta t = 2 \times 10^{-1}$ s. The same canonical test as in Fig. 5.3.1 is used, and Fig. 5.3.4 shows the RMS errors obtained from three simulations. Fig. 5.3.4 proves the correctness of the thermal UTLM method with quadrilateral combined nodes, and it also illustrates that the thermal UTLM method can achieve slightly better accuracy with a lower gird resolution and a larger time step compared with the fully explicit five-point finite difference scheme, although more memory is required for computation. Similar to the reason why the local minima exist in Fig. 5.3.1, the spike in Fig. 5.3.4 is still because of the underlying wave behaviour depending on different mesh resolutions and simulation time steps (Δt). As the simulation time increases, the envelope of the error is smoothly decreasing because there is no heat source placed in the domain.

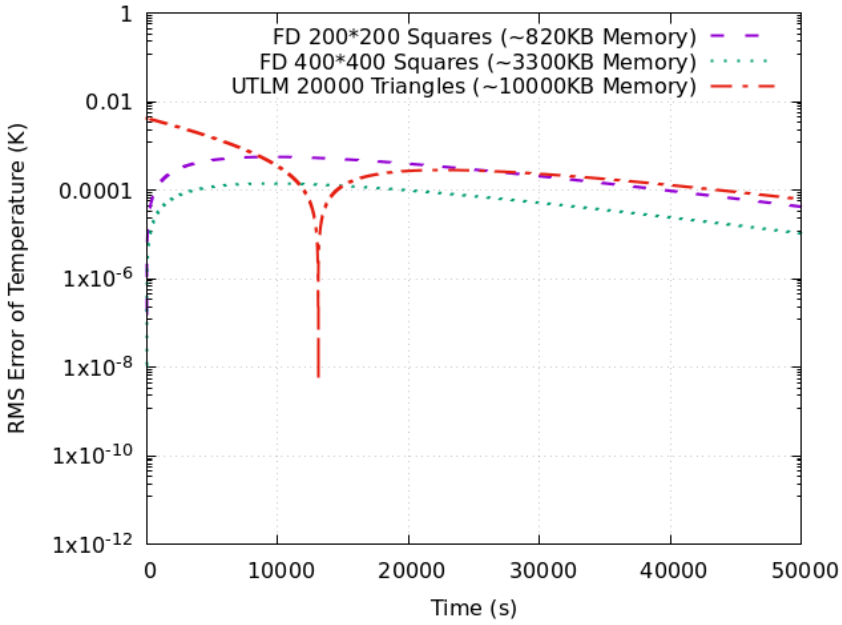

Fig. 5.3.4: RMS error of temperature obtained using the fully explicit 5-point finite difference scheme and the thermal UTLM scheme

5.3.3 Simulation of Power Transistor

The thermal UTLM has the advantage of being able to simulate real engineering cases particularly when non-Cartesian boundaries and multiple materials are involved. This section demonstrates an example simulation of the temperature profile around a power transistor with a heat sink on top. The schematic of the physical model and the layout of the computational domain is shown in Fig. 5.3.5, where the power transistor is modelled as silicon, and the heat sink is modelled as copper. The physical parameters of silicon, copper and the surrounding air taken in this simulation are listed in Table 5.3.1 [32], and the volume heat source of the silicon region is specified as $Q_{VS} = 9 \times 10^5$ W $\cdot$ m^{-3} to describe a typical heat dissipation.

Table 5.3.1: Thermal parameters setup

Material	k_{th} (W/(m $\cdot$ K))	ρ_m (kg/m^3)	c_p (J/(kg $\cdot$ K))
Air	0.0262	1.225	1005
Silicon	148	2320	700
Copper	393	8960	276

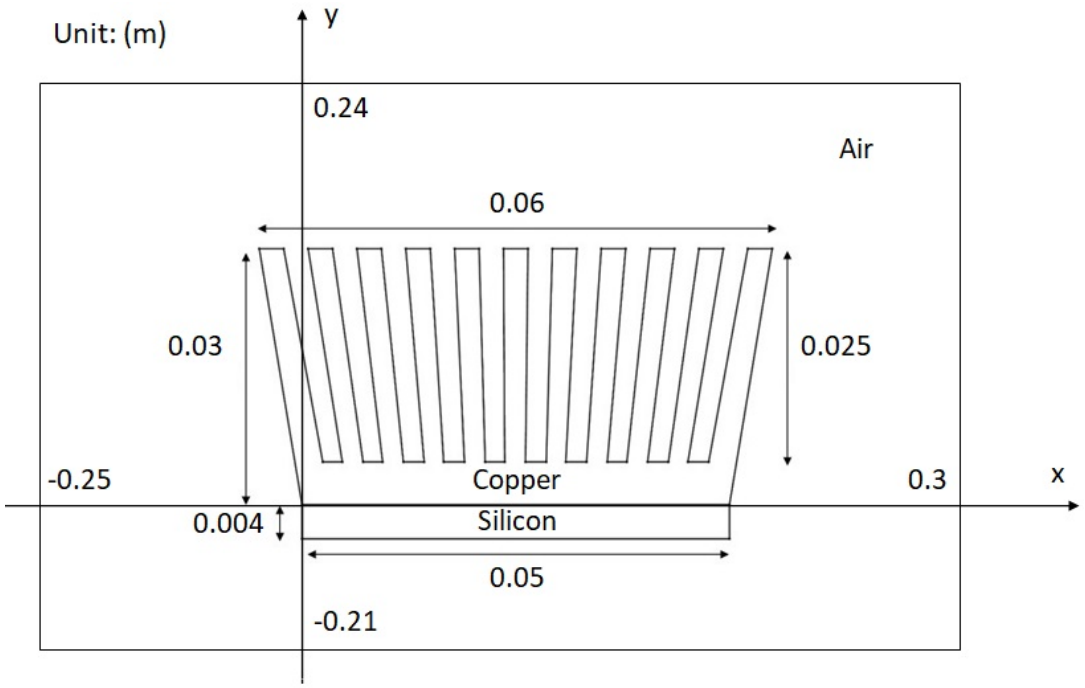

Fig. 5.3.5: Layout of a heat sink on top of a power transistor. The fins and the air gaps have the same width and evenly divide the top and bottom of the trapezoidal shape. The scale of the outer rectangular boundary is for illustration purposes only and does not match the scale of the axes.

The 2D heat sink model shown in Fig. 5.3.5 is triangulated, and the effectiveness of the mesh optimisation technique is tested. The 2D heat sink geometry is firstly triangulated using the classic Delaunay triangulation algorithm, and then the ODT algorithm is applied to optimise it.

Fig. 5.3.6 compares the Delaunay mesh of the 2D heat sink model before and after the ODT iterations. Note that the structure is not coordinate-aligned along the y-axis and that in both cases the Delaunay triangulation provides smooth boundaries. These two histograms illustrate that the ODT mesh (Fig. 5.3.6b) leads to more uniform link-line lengths compared with the unoptimised mesh (Fig. 5.3.6a). The ratio between the maximum link-line length and the minimum link-line length can also be used as a measure of mesh uniformity, and it has reduced from 4173.1 to 151.7. Furthermore, the ODT mesh uses fewer triangles (851) compared with the normal Delaunay mesh (876). Note that the node clustering technique is not used in this test.

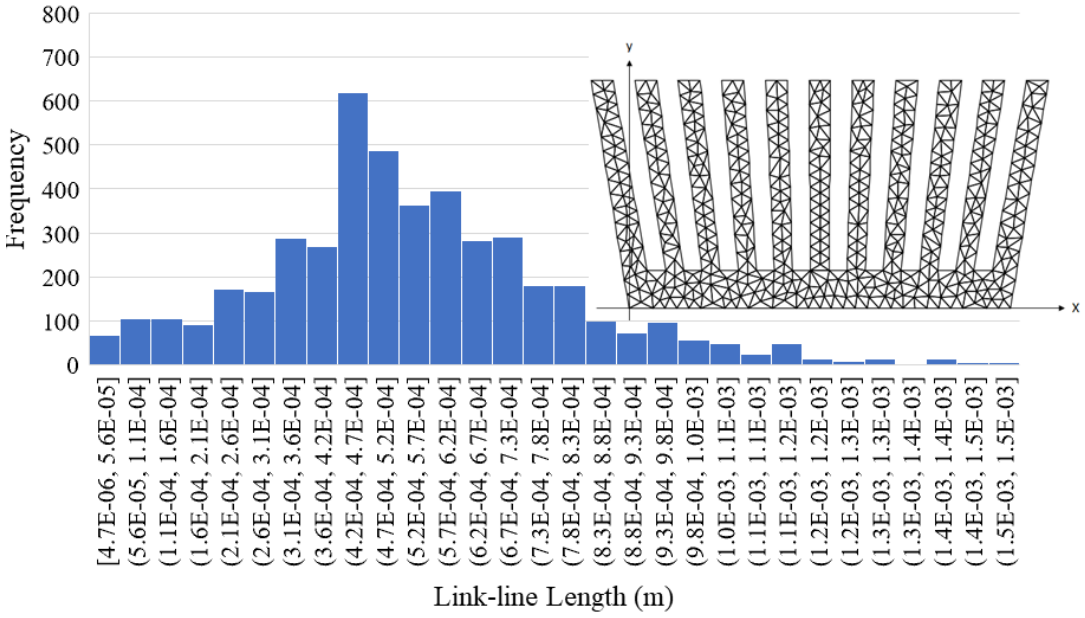

(a)

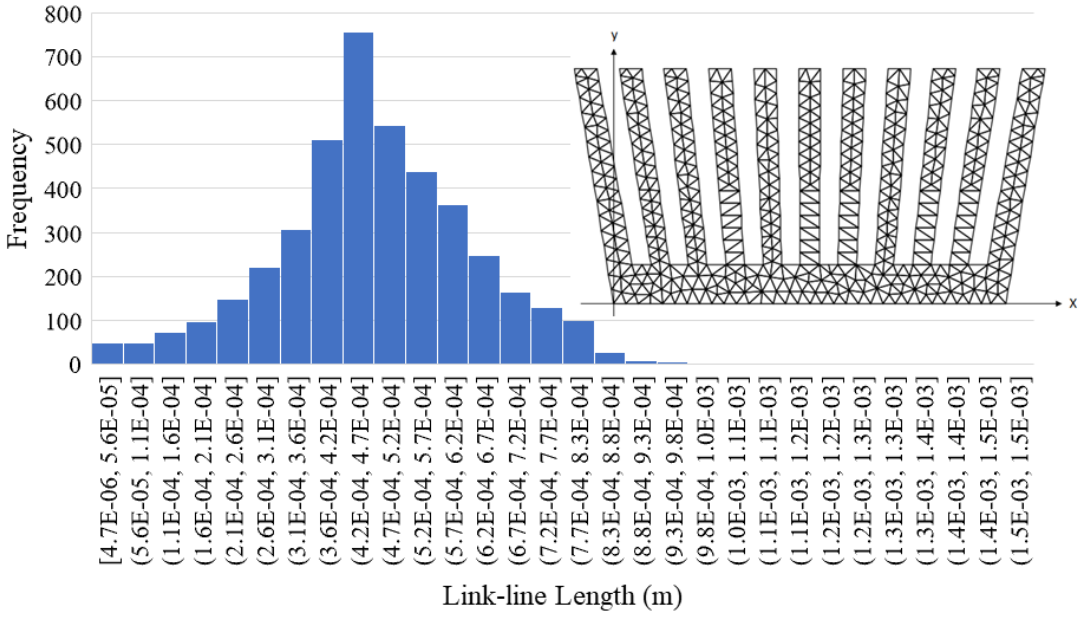

(b)

Fig. 5.3.6: (a) Normal Delaunay triangular mesh (876 triangles) (b) ODT mesh (851 triangles). Histograms show the distributions of resultant link-line lengths. Insets are the meshes.

The initial temperature across the whole domain is set to 298.15 K, and the boundary temperature is fixed as 298.15 K. The temperature distribution after 5 s and 300 s obtained by the thermal UTLM method is shown in Fig. 5.3.7a and Fig. 5.3.7b respectively. In this simulation, an ODT mesh with 978649 triangles generated by the ODT algorithm is used, and the time step is chosen as $\Delta t = 2 \times 10^{-2}$ s. It is seen that the thermal UTLM method based on the ODT mesh can keep being stable and produce a reasonable solution with smooth temperature transitions at all material interfaces, which indicates the great reliability of the proposed method particularly for unstructured complicated geometries and multi-material heat transfers. Note that the diffusion equation only models heat conduction, so convection and radiation are not considered in this simulation. Although techniques such as using the equivalent thermal conductivity with the Nusselt number [25] can be applied, they are beyond the scope of this demonstration test which is designed to show the capability of the proposed method when dealing with multi-material heat diffusion problems with complicated geometries.

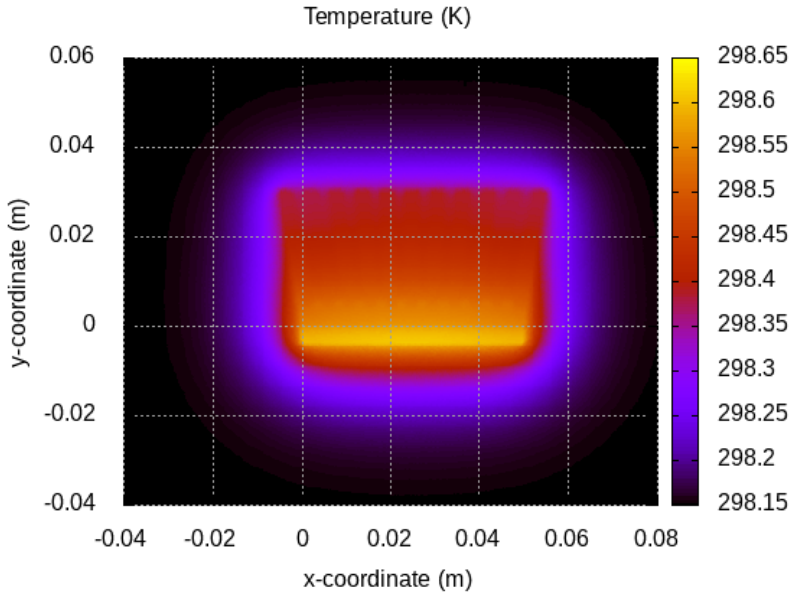

(a)

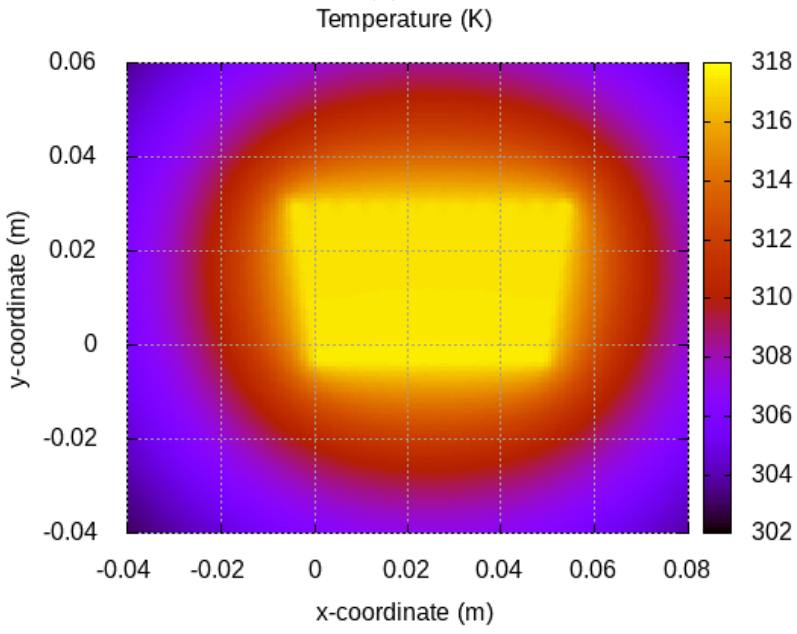

(b)

Fig. 5.3.7: Temperature distribution around the transistor with a heat sink after (a) 5 s and (b) 300 s.

5.4 Conclusion

The two-dimensional UTLM method using the ODT mesh has been presented and applied to solve the thermal diffusion equation numerically. The heat diffusion equation is mapped onto the equivalent transmission-line parameters, and the spatial second-order average local accuracy of this scheme has been shown. The thermal UTLM method using the ODT mesh is shown to be correct, stable and reliable when the physical model involves complicated boundary shapes and multi-material profiles. Also, the time-domain thermal UTLM method is not limited by the CFL condition on the time step, and as an explicit scheme, it does not require matrix-solving either, which is the main advantage against both implicit schemes and other explicit schemes.

Chapter 6

Drude Plasma Model and the Implementations

This chapter starts with a brief introduction to the plasma physics behind the Drude plasma model, covering the formulae to evaluate plasma parameters. Then, the implementations of the Drude model in the two-dimensional TE series TLM method based on Cartesian grids and unstructured triangular grids are derived respectively. The implementation using the unstructured TLM method is newly proposed, in which the frequency-dependent electrical permittivity of plasma and the Joule heating power density evaluation are supported.

6.1 Plasma Physics and the Drude Model

6.1.1 Overview

Plasma is known as the fourth state of matter in addition to solid, liquid and gas, and two well-known phenomena of plasma are the lightning strikes and the auroras. Containing high energy is one of its major characteristics. Detailed physics of plasma is out of the scope of this work, but the parameters related to the Drude plasma model are briefly introduced in this section.

6.1.2 The Drude Model

According to [87], applying Newton's laws of motion to a particle gives

$$\frac{d}{dt}\boldsymbol{p}(t) = -q_e\boldsymbol{E}(t) - \boldsymbol{p}(t)/\tau_c, \tag{6.1.1}$$

where $\boldsymbol{p} = m_e\boldsymbol{v_e}$ is the momentum of the electron, q_e is the electron charge, $\boldsymbol{E}$ is the electric field strength, and τ_c is the mean free time between collisions. The second term on the RHS of (6.1.1) represents the damping term due to the Drude effects [87]. In the frequency domain, (6.1.1) is expressed as

$$\boldsymbol{p}(\omega) = -\frac{q_e\boldsymbol{E}(\omega)}{\nu_c + j\omega}, \tag{6.1.2}$$

where $\nu_c = 1/\tau_c$ is the electron-ion collision frequency.

From the definition of the volume current density we get

$$\boldsymbol{J}(\omega) = -n_e q_e \boldsymbol{v_e} = -n_e q_e \frac{\boldsymbol{p}}{m_e}, \tag{6.1.3}$$

where n_e is the electron density, $\boldsymbol{v}_e$ is the electron velocity, and m_e is the electron mass. Substituting (6.1.2) into (6.1.3) gives

$$\boldsymbol{J}(\omega) = \frac{n_e q_e^2}{m_e(\nu_c + j\omega)}\boldsymbol{E}(\omega), \tag{6.1.4}$$

and based on Ohm's law, we find the complex electrical conductivity as

$$\sigma_e(\omega) = \frac{n_e q_e^2}{m_e(\nu_c + j\omega)}. \tag{6.1.5}$$

The relationship between the complex permittivity and the complex conductivity is shown as

$$\varepsilon(\omega) = \varepsilon_0\left(1 + \frac{\sigma_e(\omega)}{j\omega\varepsilon_0}\right), \tag{6.1.6}$$

and substituting (6.1.5) into (6.1.6) gives

$$\varepsilon(\omega) = \varepsilon_0 \left(1 + \frac{n_e q_e^2}{m_e \varepsilon_0} \frac{1}{\omega(j\nu_c - \omega)}\right). \tag{6.1.7}$$

The plasma frequency is defined as

$$\omega_p = \sqrt{\frac{n_e q_e^2}{\varepsilon_0 m_e}}, \tag{6.1.8}$$

and the complex permittivity can be written in the form of

$$\varepsilon(\omega) = \varepsilon_0 \left(1 + \frac{\omega_p^2}{\omega(j\nu_c - \omega)}\right). \tag{6.1.9}$$

This is the Drude model, the same as we mentioned early in Chapter 1. Also, substituting (6.1.8) into (6.1.5) yields the complex electrical conductivity in the frequency domain as

$$\sigma_e(\omega) = \frac{\omega_p^2 \varepsilon_0}{\nu_c + j\omega}. \tag{6.1.10}$$

When the wave frequency ω is much greater than the electron-ion collision frequency ν_c (i.e. $\omega \gg \nu_c$), the permittivity can be reduced to

$$\varepsilon(\omega) = \varepsilon_0 \left(1 - \frac{\omega_p^2}{\omega^2}\right). \tag{6.1.11}$$

In this case, the wave propagation constant is [48]

$$\gamma = j\omega\sqrt{\mu\varepsilon_0}\sqrt{1 - \frac{\omega_p^2}{\omega^2}}, \tag{6.1.12}$$

which means that frequency components less than ω_p will lead to a purely real propagation constant γ and hence will be strongly attenuated in plasma [88]. Plasma leading to this case is known as overdense plasma [89]. Furthermore, as will be seen in Section 6.2, the plasma frequency ω_p is positively correlated with the temperature T; therefore, a higher temperature gives a higher plasma frequency, making relatively low-frequency wave components harder to penetrate the plasma, and a low enough temperature makes the plasma similar to simple air gas.

In fully ionised plasma, all collisions are between charged particles, and for charged particles, their effective radius during collisions is much larger than their atomic radius because of Coulomb forces. The deflection angle in this case also tend to be small. These collisions under the effect of Coulomb fields are named the Coulomb collisions [90, 91]. The Coulomb forces are confined approximately within a spherical area, named the Debye sphere, with a radius of λ_D, named the Debye length. The Debye length can be seen as the effective radius of particles during Coulomb collisions, and it is calculated as [89, 90]:

$$\lambda_D = \sqrt{\frac{\varepsilon_0 k_B T}{q_e^2 n_e}}, \tag{6.1.13}$$

where ε_0 is the permittivity of free space, $k_B = 1.38 \times 10^{-23} \mathrm{J \cdot K^{-1}}$ is the Boltzmann constant, and T is the temperature.

The electron-ion collision frequency ν_c is calculated using [92]

$$\nu_c = 2.9 \times 10^{-12} \left(\frac{n_e \ln \Lambda}{T_{eV}^{3/2}} \right), \tag{6.1.14}$$

where T_{eV} is the temperature in electron-volt (1 eV $\approx$ 11606 K), and $\ln \Lambda$ is the Coulomb logarithm which is calculated using [89]

$$\ln \Lambda = \ln \frac{9 N_D}{Z}, \tag{6.1.15}$$

where Z is the ion charge state, N_D is the number of electrons inside the Debye sphere calculated as

$$N_D = n_e \cdot \frac{4}{3} \pi \lambda_D^3. \tag{6.1.16}$$

One can also use the effective and simplified formulae provided in [92] to calculate the Coulomb logarithm $\ln \Lambda$:

$$\ln \Lambda = 23 - \frac{1}{2} \ln \left(\frac{10^{-6} n_e}{T_{eV}^3} \right). \tag{6.1.17}$$

Note that the unit of n_e used in [92] is cm^{-3}, so there is an extra scaling factor of 10^{-6} in (6.1.14) and (6.1.17).

6.2 Expression of Electron Concentration

The electron concentration n_e is also a function of the temperature T, and a figure that records this relation is provided in [93]. Since the explicit expression of $n_e(T)$ is not given, Lagrange interpolation is used in this work to obtain an explicit expression of $n_e(T)$. The pressure is assumed to be 1 atm when evaluating n_e. Having considered that the $(\log_{10} n_e) - T$ curve has different characteristics at different ranges of T, the interpolated function (defined as (6.2.3)) is divided into three pieces to fit the fast-rising part (exponent modelled using (6.2.1)), the slow-rising part (exponent modelled using (6.2.2)) and the plateau part (exponent modelled as a constant) respectively.

$$\begin{aligned} L_1(T) = {} & 10.347216872112 \left(\frac{T}{1000}\right) - 2.091767471935 \left(\frac{T}{1000}\right)^2 \\ & + 0.197825060533 \left(\frac{T}{1000}\right)^3 - 0.006992048206 \left(\frac{T}{1000}\right)^4 \end{aligned} \tag{6.2.1}$$

$$\begin{aligned} L_2(T) = {} & 16.143076923077 + 0.92 \left(\frac{T}{1000}\right) \\ & - 0.034353846153 \left(\frac{T}{1000}\right)^2 + 0.000292307692 \left(\frac{T}{1000}\right)^3 \end{aligned} \tag{6.2.2}$$

$$n_e(T) = \begin{cases} 10^{L_1(T)} & T < 10000 \\ 10^{L_2(T)} & 10000 \leq T < 20000 \\ 10^{23.14} & T \geq 20000 \end{cases} \tag{6.2.3}$$

The effectiveness of the piecewise-defined interpolated $n_e(T)$ is shown in Fig. 6.2.1, and a good fit of the numerical model to the original data curve is observed.

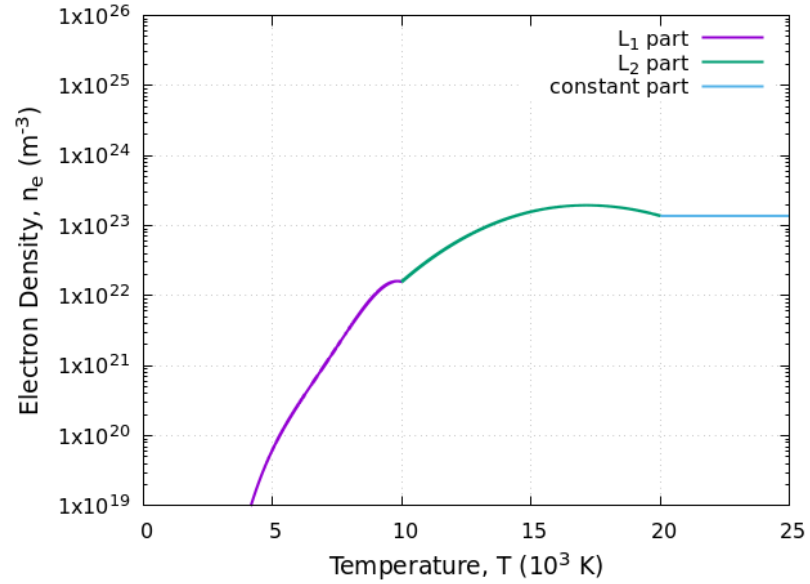

(a)

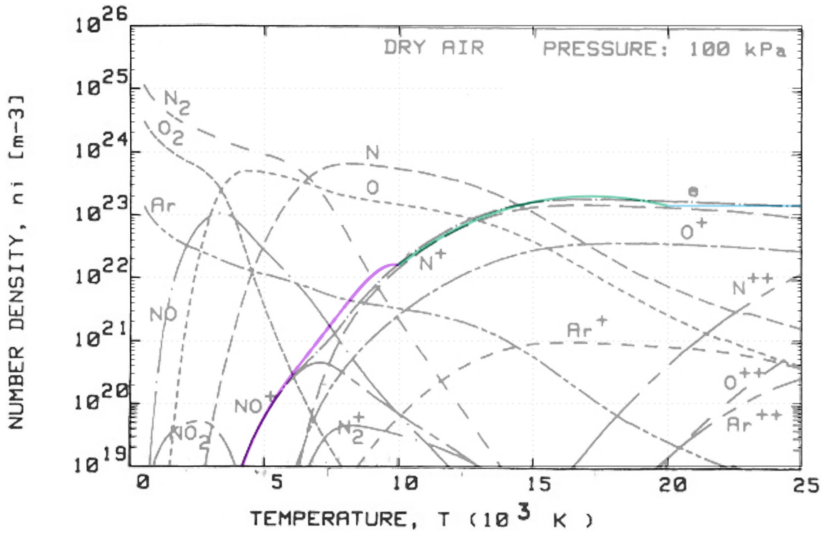

(b)

Fig. 6.2.1: Electron density of dry air at 1 atm as a function of temperature: (a) piecewise interpolated function defined by (6.2.3), and (b) the comparison between the interpolated function and the reference curve given on page 241 of [93].

6.3 Implementation of the Drude Model

6.3.1 Overview

The overall idea guiding the implementation of the Drude model in TLM methods is to design digital voltage filters as replacements of classic voltage calculation formulae used to solve the Thévenin equivalent circuits. The voltage filters are placed at each port between adjacent nodes in the mesh to replace the classic way to calculate the middle voltage at ports during the scattering and connection process of TLM methods, while the scattering and connection process at node centres is not changed. First, the transmission-line equations are expressed in the Laplace domain (s-domain) and the frequency domain to cope with the frequency-dependent permittivity, leading to s-domain filters. Then, the bilinear transformation is used to discretise s-domain filters, giving z-domain digital filters which are next embedded in the scattering and connection process. If the Joule heating effect is also considered in the model, another digital filter will be required for the current density evaluation.

In terms of 2D applications, TE modes are more of interests in this work that involves the plasma heating and lightning effect investigations, and therefore, this work implements the Drude plasma model in the 2D TE series version of both Cartesian and unstructured TLM methods, with a particular focus on the latter. The specific digital voltage filters differ between Cartesian grids and unstructured triangular grids. In [37], a first-order digital filter was designed to embed the Drude model into the classic Cartesian TE TLM method, and this formulation is re-derived as follows in a more general way without using normalisation. To implement the Drude model in the unstructured TLM (UTLM) method, a new digital filter, which is second-order, is derived in this section as follows. The current density evaluation filter remains the same for Cartesian and unstructured grids.

6.3.2 In Cartesian Uniform Grids

The implementation of the Drude plasma model in Cartesian uniform grids is introduced in this section. According to (2.4.6) and Fig. 2.4.1, the series inductance

on a single branch of the TE series TLM node is

$$L = \frac{\frac{1}{2}\mu_0 \Delta l}{2} = \mu_0 \Delta l/4, \tag{6.3.1}$$

and its associated error capacitance is

$$C_e = \frac{(\Delta t/2)^2}{L} = \frac{\Delta t^2}{\mu_0 \Delta l}, \tag{6.3.2}$$

where

$$\Delta t = \frac{1}{\sqrt{2}} \Delta l / c_0 \tag{6.3.3}$$

is the simulation time step, and c_0 is the speed of light in vacuum.

The stub capacitance at the port is used to model the non-uniform permittivity; it is shown in Fig. 6.3.1a and it is calculated as

$$C_s = \varepsilon(\omega) \Delta l - 2C_e, \tag{6.3.4}$$

where the coefficient 2 before C_e is because it counts for the error capacitance from both sides. Then, substituting the Drude model permittivity (6.1.9), the error capacitance associated with a single inductive link (6.3.2) and the simulation time step (6.3.3) into (6.3.4) gives

$$C_s = \frac{\omega_p^2}{s(\nu_c + s)} \varepsilon_0 \Delta l, \tag{6.3.5}$$

where the angular frequency variable ω is substituted by the Laplace complex variable s based on $s = j\omega$.

At the interface between two adjacent ports, nodal voltage analysis to the Thévenin equivalent circuit shown in Fig. 6.3.1b gives

$$\frac{V_m - 2V_L^i}{Z_L} + \frac{V_m - 2V_R^i}{Z_R} + V_m (s \cdot C_s) = 0, \tag{6.3.6}$$

where V_m is the voltage at the middle of the port.

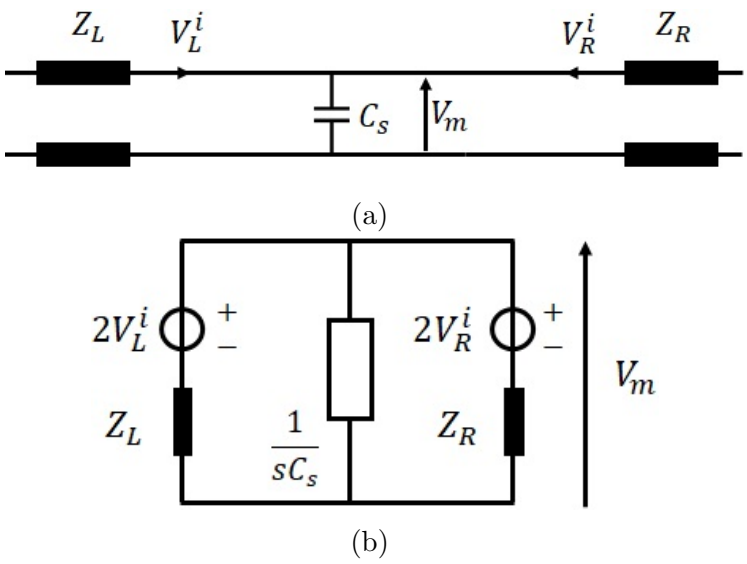

Fig. 6.3.1: (a) A port connecting two 2D Cartesian series nodes and (b) its Thévenin equivalent circuit

Substituting (6.3.5) into (6.3.6) and then using the bilinear transformation $s = \frac{2}{\Delta t}\frac{1-z^{-1}}{1+z^{-1}}$ yield the voltage relation in the z-domain as

$$\begin{aligned}
&\left((Z_L+Z_R)\left(\nu_c+\frac{2}{\Delta t}\right)+Z_LZ_R\cdot\omega_p^2\varepsilon_0\Delta l\right)V_m\\
&=\left(\nu_c+\frac{2}{\Delta t}\right)\left(2V_L^iZ_R+2V_R^iZ_L\right)\\
&+\left(\nu_c-\frac{2}{\Delta t}\right)\left(2V_L^iZ_R+2V_R^iZ_L\right)z^{-1}\\
&-\left((Z_L+Z_R)\left(\nu_c-\frac{2}{\Delta t}\right)+Z_LZ_R\cdot\omega_p^2\varepsilon_0\Delta l\right)V_mz^{-1}.
\end{aligned} \tag{6.3.7}$$

Applying the inverse z-transform to (6.3.7) gives the time-domain update formula as

$$\begin{aligned}
V_m[n] = &\frac{1}{\left((Z_L+Z_R)\left(\nu_c+\frac{2}{\Delta t}\right)+Z_LZ_R\cdot\omega_p^2\varepsilon_0\Delta l\right)}\\
&\cdot\left(\left(\nu_c+\frac{2}{\Delta t}\right)\left(2V_L^i[n]Z_R+2V_R^i[n]Z_L\right)\right.\\
&+\left(\nu_c-\frac{2}{\Delta t}\right)\left(2V_L^i[n-1]Z_R+2V_R^i[n-1]Z_L\right)\\
&\left.-\left((Z_L+Z_R)\left(\nu_c-\frac{2}{\Delta t}\right)+Z_LZ_R\cdot\omega_p^2\varepsilon_0\Delta l\right)V_m[n-1]\right),
\end{aligned} \tag{6.3.8}$$

where $[n]$ and $[n-1]$ represent the samples at the present time and one time step before respectively.

The Joule heating power density of the plasma is calculated via first expressing the complex plasma electrical conductivity in the s-domain as

$$\sigma_e(s) = \frac{\omega_p^2 \varepsilon_0}{\nu_c + s}. \tag{6.3.9}$$

Therefore, the current density in the Laplace domain is

$$\boldsymbol{J}(s) = \sigma_e(s)\boldsymbol{E}(s) = \frac{\omega_p^2 \varepsilon_0}{\nu_c + s}\boldsymbol{E}(s), \tag{6.3.10}$$

where $\boldsymbol{E} \equiv (E_x, E_y)$ represents the transverse electric field. Applying the bilinear transformation gives the current density in the z-domain as

$$\boldsymbol{J}[z] = \frac{\omega_p^2 \varepsilon_0 \Delta t}{\nu_c \Delta t + 2}\boldsymbol{E}[z]\left(1 + z^{-1}\right) - \frac{\nu_c \Delta t - 2}{\nu_c \Delta t + 2}\boldsymbol{J}[z]z^{-1}. \tag{6.3.11}$$

The inverse z-transform is used to obtain the discrete time domain update formula for the current density

$$\boldsymbol{J}\left[n\right] = \frac{\omega_p^2 \varepsilon_0 \Delta t}{\nu_c \Delta t + 2}\left(\boldsymbol{E}\left[n\right] + \boldsymbol{E}\left[n-1\right]\right) - \frac{\nu_c \Delta t - 2}{\nu_c \Delta t + 2}\boldsymbol{J}\left[n-1\right], \tag{6.3.12}$$

and the Joule heating power density is calculated as

$$P\left[n\right] = \boldsymbol{E}\left[n\right] \cdot \boldsymbol{J}\left[n\right]. \tag{6.3.13}$$

The Joule heating power density is taken as the volume heat source of heat diffusion problems during electrothermal coupling if the Joule heating is the only source of heat. In this case, we have

$$Q_{VS}[n] = P[n]. \tag{6.3.14}$$

Remarks

One may not prefer to calculate the Joule heating power density directly using the frequency domain relationship $P(\omega) = \sigma_e(\omega)\boldsymbol{E}^2(\omega)/2$ as it is not simple to

discretise a higher-order response. Also, Parseval's theorem is not applicable here to simplify the expression because σ_e is not constant.

6.3.3 In Unstructured Triangular Grids

The implementation of the Drude model in unstructured triangular grids is similar to that in Cartesian grids, but since the link-line lengths in unstructured grids are naturally not all the same, extra coefficients are involved as is explained below in this section.

The stub capacitance at the port is designed to model the permittivity and also compensate for uneven link-line lengths in the unstructured TLM method. Since in the UTLM formulation, the value of the capacitance and the inductance depends on different definitions of node centre positions and port positions (see [71, 94] and also Chapter 4), general coefficients (α and β) are employed here for now to express the capacitance and the inductance in the UTLM formulation.

$$C = \alpha\varepsilon \qquad (6.3.15) \qquad\qquad L = \beta\mu \qquad (6.3.16)$$

If the model introduced in Section 4.4 (also [94]) is in use, α and β are then

$$\alpha = \frac{\Delta_i}{l_i}, \qquad (6.3.17) \qquad\qquad \beta = \frac{l_i r}{2}. \qquad (6.3.18)$$

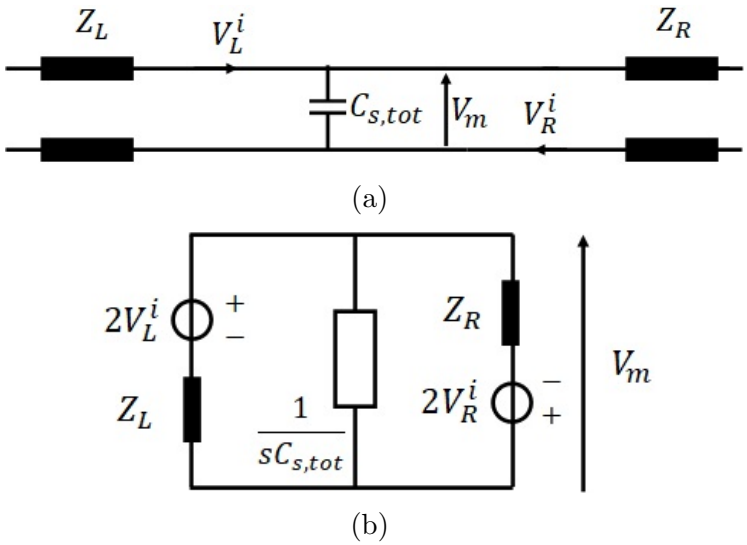

Fig. 6.3.2: (a) A port connecting two 2D triangular series nodes and (b) its Thévenin equivalent circuit

Summing up the stub capacitance from the left side and the right side gives the total stub capacitance $C_{s,tot}$ illustrated in Fig. 6.3.2a. Note that α and β may be different for the left side and the right side. Fig. 6.3.2b is the Thévenin circuit of Fig. 6.3.2a, and all the circuit parameters are denoted in the Laplace s-domain. Subscript $_L$ and $_R$ represent the left side and the right side of the port without loss of generality. Z_L and Z_R represent the transmission-line characteristic impedance, and V_L^i and V_R^i are incident voltages. Note that V_L^i and V_R^i are in different directions because of the definition given in Section 4.4.

In the Laplace domain, the complex permittivity in (6.1.9) becomes

$$\varepsilon\left(s\right) = \varepsilon_0 \left(1 + \frac{\omega_p^2}{s\left(\nu_c + s\right)}\right), \tag{6.3.19}$$

where $s = j\omega$.

The stub capacitance of each side is calculated still by subtracting the error capacitance of the link inductor from the original model capacitance, denoted as

$$C_{s,L} = C_L - \frac{\left(\Delta t/2\right)^2}{L_L} = \alpha_L\ \varepsilon_L(s) - \frac{\left(\Delta t/2\right)^2}{\beta_L\ \mu} \tag{6.3.20}$$

and

$$C_{s,R} = C_R - \frac{\left(\Delta t/2\right)^2}{L_R} = \alpha_R\ \varepsilon_R(s) - \frac{\left(\Delta t/2\right)^2}{\beta_R\ \mu} \tag{6.3.21}$$

if the general coefficients (6.3.15) and (6.3.16) are used, and the single trip time on each inductive link is $\Delta t/2$.

The total stub capacitance at a port $C_{s,tot}$ is calculated via summing up the left-side stub capacitance and the right-side stub capacitance. Then, substituting (6.3.19) into it yields

$$C_{s,tot} = N + \frac{M}{s\left(\nu_c + s\right)}, \tag{6.3.22}$$

where

$$N = \left(\alpha_L + \alpha_R\right)\varepsilon_0 - \frac{\left(\Delta t/2\right)^2}{\beta_L\mu} - \frac{\left(\Delta t/2\right)^2}{\beta_R\mu}, \tag{6.3.23}$$

and

$$M = \left(\alpha_L + \alpha_R\right)\varepsilon_0\omega_p^2. \tag{6.3.24}$$

The coefficient N is used to cope with uneven link-line lengths between adjacent node centres, and N is zero in the uniform square Cartesian grid. Δt represents the simulation time step, and the voltage pulse takes $\Delta t/2$ to propagate from the node centre to the port.

Applying nodal voltage analysis to the Thévenin equivalent circuit shown in Fig. 6.3.2b gives

$$\frac{V_m(s) - 2V_L^i(s)}{Z_L} + \frac{V_m(s) + 2V_R^i(s)}{Z_R} + V_m(s)\left(sC_{s,tot}\right) = 0, \tag{6.3.25}$$

where V_m is the voltage at the middle of the port.

Substituting (6.3.22) into (6.3.25) and then using the bilinear transformation $s = \frac{2}{\Delta t}\frac{1-z^{-1}}{1+z^{-1}}$ yields

$$\begin{aligned} K_0 V_m[z] =& 2\left(V_L^i[z]Z_R - V_R^i[z]Z_L\right) \\ & \cdot \left(K_1 + K_2 z^{-1} + K_3 z^{-2}\right) \\ & - K_4 V_m[z] z^{-1} - K_5 V_m[z] z^{-2} \end{aligned} \tag{6.3.26}$$

where

$$K_0 = (Z_L + Z_R)\left(\nu_c + \frac{2}{\Delta t}\right) + N \cdot Z_L Z_R \frac{2}{\Delta t}\left(\nu_c + \frac{2}{\Delta t}\right) + M \cdot Z_L Z_R, \tag{6.3.27}$$

$$K_1 = \left(\nu_c + \frac{2}{\Delta t}\right), \tag{6.3.28}$$

$$K_2 = 2\nu_c, \tag{6.3.29}$$

$$K_3 = \left(\nu_c - \frac{2}{\Delta t}\right), \tag{6.3.30}$$

$$K_4 = (Z_L + Z_R)\,2\nu_c - 2N \cdot Z_L Z_R \left(\frac{2}{\Delta t}\right)^2 + 2M \cdot Z_L Z_R, \tag{6.3.31}$$

$$K_5 = (Z_L + Z_R)\left(\nu_c - \frac{2}{\Delta t}\right) - N \cdot Z_L Z_R \frac{2}{\Delta t}\left(\nu_c - \frac{2}{\Delta t}\right) + M \cdot Z_L Z_R. \tag{6.3.32}$$

By using the inverse z-transform, the update formula for the port voltage in the

discrete time domain is obtained as

$$\begin{aligned} V_m[n] = \frac{1}{K_0}(&2K_1\left(V_L^i Z_R - V_R^i Z_L\right) \\ &+ 2K_2\left(V_L^i[n-1]Z_R - V_R^i[n-1]Z_L\right) \\ &+ 2K_3\left(V_L^i[n-2]Z_R - V_R^i[n-2]Z_L\right) \\ &- K_4 V_m[n-1] - K_5 V_m[n-2]), \end{aligned} \tag{6.3.33}$$

where $[n]$, $[n-1]$ and $[n-2]$ represent the samples at the present time, one time step before and two time steps before respectively.

Note that at each individual port built on a fixed triangular mesh, α and β are constants; therefore, N is also a constant, and M varies with the plasma frequency ω_p. The update formula (6.3.33) can be seen as a second-order digital filter that is placed at each port between adjacent triangles in the mesh to calculate the middle voltage at ports during the scattering and connection process.

The way to evaluate the Joule heating power density shown in (6.3.12) and (6.3.13) remains the same for unstructured triangular meshes, since Ohm's law in the s-domain remains the same from Cartesian grids to unstructured triangular grids.

6.4 Results

6.4.1 Power Density Calculation Method

A separate test is conducted to verify the power density calculation method. In this test, the gold plasma parameters [95] are employed, giving the plasma frequency $\omega_p = 1.323 \times 10^{16}$rad/s and the collision frequency $\nu_c = 1.26 \times 10^{14}$Hz. Based on these two plasma parameters, the theoretical effective conductivity at wavelength $\lambda = 1.55\mu m$ is obtained by using (6.1.10) and taking its real part, giving

$$\sigma_{e,eff}(\text{theoretical}) = 130815 \text{ S/m}. \tag{6.4.1}$$

This wavelength is specified according to the operating wavelength given in [96].

The simulated effective electrical conductivity obtained based on (6.3.12) and (6.3.13) is evaluated by dividing the time-average power density by the time-average of the squared electric field strength, shown as

$$\sigma_{e,eff}(\text{simulated}) = \frac{\left(\sum_{i=1}^{N_T} P[i]\right)/N_T}{\left(\sum_{i=1}^{N_T} (E[i])^2\right)/N_T}, \tag{6.4.2}$$

where N_T is the number of simulation time steps. For simplicity and effectiveness, the electric field strength used in this test is specified to be a scalar instead of a vector. The simulation time step, i.e. the sampling time interval of the digital filter, is chosen to be $\Delta t = 2 \times 10^{-17}$ s. The simulated effective conductivity is evaluated at various different stop time frames up to the final stop time $t_{stop,final} = 10^{-11}$ s (namely 10 ps). The input electric field strength is specified to be

$$E[i] = \begin{cases} 0 & i < 0 \\ \sin\left(2\pi \frac{c_0}{\lambda}(i\Delta t)\right) & i \geq 0 \end{cases}, \tag{6.4.3}$$

where c_0 is the speed of light in vacuum, $\Delta t = 2 \times 10^{-17}$ s, and $\lambda = 1.55\mu m$ as mentioned above.

The simulated effective conductivity up to different stop time frames is plotted in Fig. 6.4.1. As is seen, the effective conductivity settles very fast to its steady state after an overshoot at the very beginning when the input signal (electric field strength) starts. Details at the very beginning and at the steady state of Fig. 6.4.1 are displayed in Fig. 6.4.2. The steady state value is about 130944 S/m, and it is close to the theoretical value with an relative error of only $|130944 - 130815|/130815 = 0.099\%$. The percentage ripple at the steady state is only $105/130944 = 0.080\%$ and is insignificant. Furthermore, the ripples are small enough after 0.1 ps.

This test demonstrates that the proposed Joule heating power density calculation method, namely (6.1.10), can reveal the plasma electrical conductivity correctly according to the given wavelength (hence frequency) under an ideal sinusoidal input.

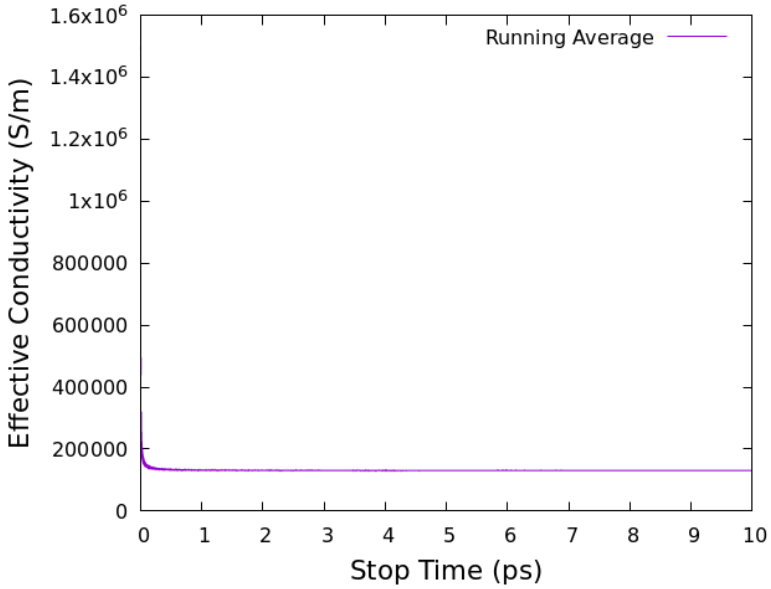

Fig. 6.4.1: Simulated effective conductivity obtained up to different stop time

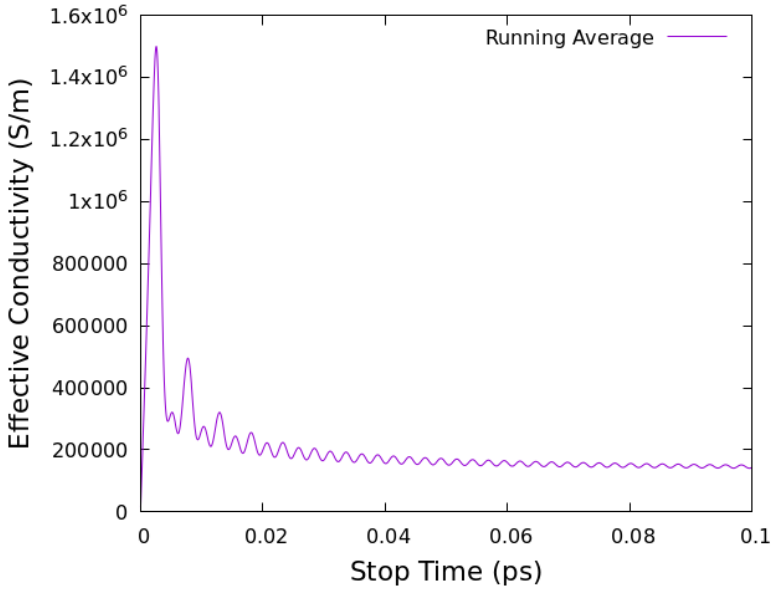

(a)

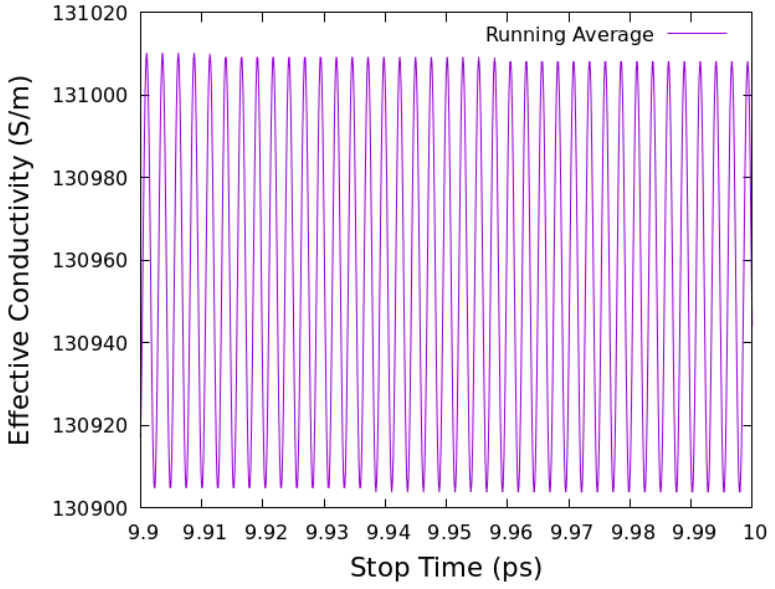

(b)

Fig. 6.4.2: Simulated effective conductivity obtained up to different stop time: (a) details at the beginning, and (b) details at the steady state

6.4.2 Nanotip Waveguide

This test is used to validate the voltage evaluation filter (6.3.33) and the Joule heating power density evaluation filter (6.3.12) and (6.3.13). The 2D TE series EM UTLM method provides the power density, and the power density is fed into the 2D thermal UTLM method as the heat source, forming one-way coupling at this moment. The two-way fully electrothermal coupled scheme will be proposed in Chapter 7.

The two-dimensional model of a plasmonic nanotip inserted into the gold wall [96] (shown in Fig. 6.4.3) is used to validate the newly developed digital filter methods for plasma. The applications of the plasmonic nanotip include focusing electromagnetic waves and heating liquids at the nanoscale. The Drude model is used to describe the gold material. The rectangular part of the silicon waveguide has a length of 3 μm and a width of 1 μm, and the triangular part has a base width of 0.45 μm and a length of 1 μm. The thickness of the silicon waveguide is 250 nm. The refractive index of the silicon waveguide is $n_m = 3.477$ [97], and at the chosen operating wavelength $\lambda = 1.55$ μm [96], its effective refractive index is $n_{eff} = 3.3917$.

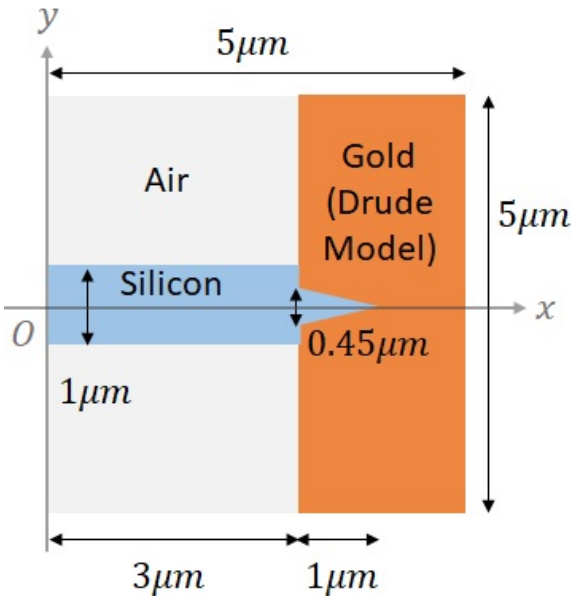

Fig. 6.4.3: The schematic of a silicon waveguide taper inserted into gold walls

The fundamental mode of the dielectric waveguide is chosen as the excitation function, which is implemented at the left boundary of the model. Note that the plasmonic mode has H_z and E_y as the dominant field components. The magnetic

field excitation function is given as

$$H_z(y,t) = H_z^0(y) \cdot \sin\left(2\pi \frac{c_0}{\lambda} \cdot t\right), \tag{6.4.4}$$

where

$$H_z^0(y) = \begin{cases} A\cos(K_n d_0)\exp(-\gamma_c(y-d_0)) & y > d_0 \\ A\cos(K_n y) & -d_0 \le y \le d_0 \\ A\cos(K_n d_0)\exp(\gamma_c(y+d_0)) & y < -d_0 \end{cases}, \tag{6.4.5}$$

$A = 27512.2$, $K_n = \frac{2\pi}{\lambda}\sqrt{n_m^2 - n_{eff}^2}$, $\gamma_c = \frac{2\pi}{\lambda}\sqrt{n_{eff}^2 - n_c^2}$, $c_0 = 1/\sqrt{\mu_0 \varepsilon_0}$, $n_c = 1$, $n_m = 3.477$, $n_{eff} = 3.3917$ and $d_0 = 0.5 \times 10^{-6}$ m.

The amplitude A is calculated in order to give the same input power density as the input power source used in [96]. The wave impedance calculated as

$$\eta = \frac{\beta}{\omega\varepsilon} = \frac{\beta\lambda}{2\pi c_0 \varepsilon} = n_{eff}\frac{2\pi}{\lambda}\frac{\lambda}{2\pi c_0 \varepsilon} = \frac{n_{eff}}{c_0 \varepsilon_0 n_m^2} = 105.62\ \Omega,$$

and the amplitude A is calculated to be

$$\frac{1}{2}\eta A^2 = \frac{10 \times 10^{-3}\ (\mathrm{W})}{1 \times 10^{-6}\ (\mathrm{m}) \times 250 \times 10^{-9}\ (\mathrm{m})} \Longrightarrow A = 27512.2\ \mathrm{A/m}$$

at an input power of 10 mW into the waveguide of size given in [96].

The plasma frequency of gold is fixed at $\omega_p = 1.323 \times 10^{16}$rad/s, and the collision frequency is fixed at $\nu_c = 1.26 \times 10^{14}$Hz according to [95]. The associated thermal parameters are listed in Table 6.4.1, where k_{th} is the thermal conductivity, ρ_m is the mass density and c_p is the specific heat capacity.

Table 6.4.1: Thermal Parameters Setup

	Air	Silicon	Gold
k_{th} (W/(m · K))	0.0262	148	317
ρ_m (kg/m^3)	1.2928	2320	19320
c_p (J/(kg · K))	1005	710	129

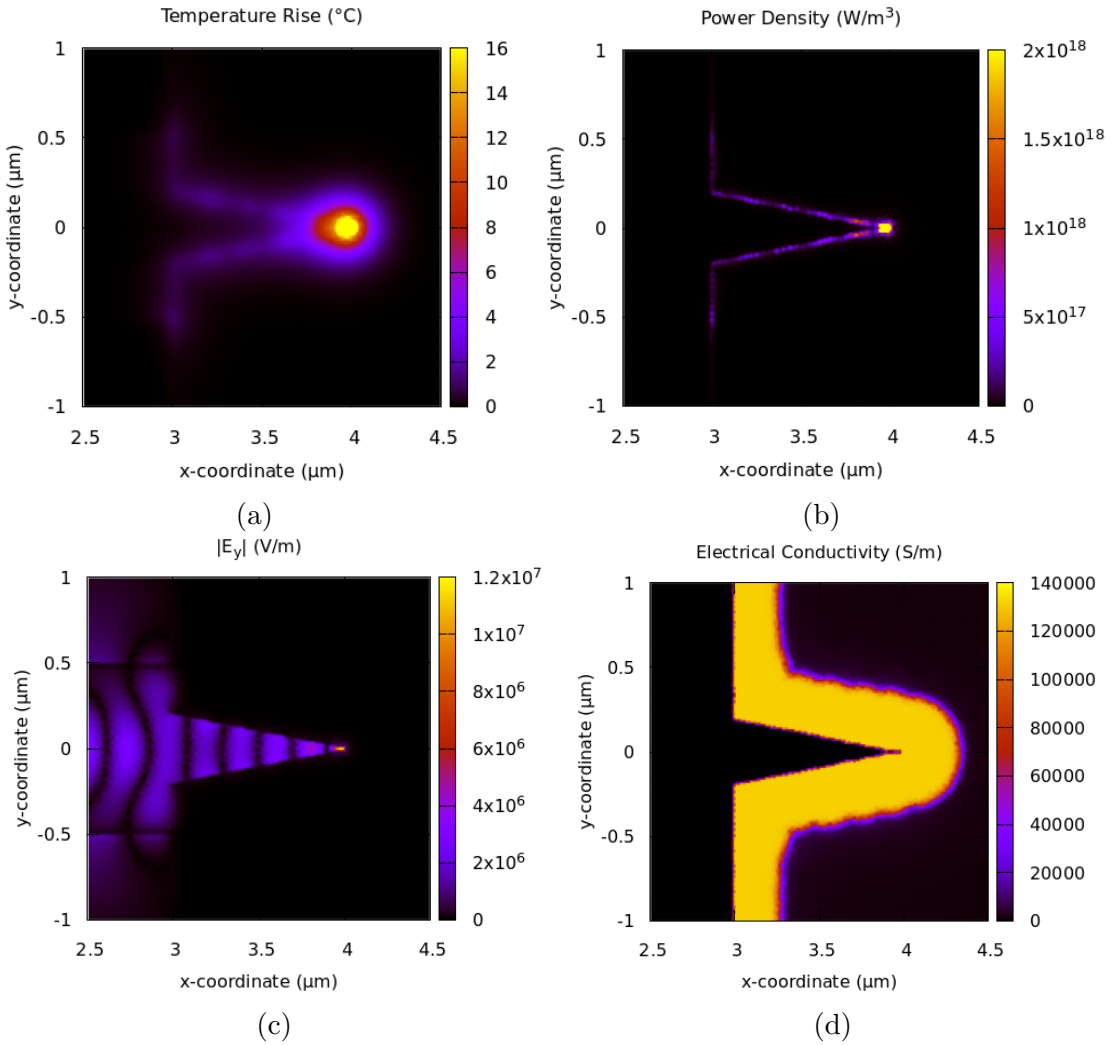

Fig. 6.4.4: (a) Temperature increase, (b) Power density, (c) Magnitude of E_y, (d) Effective conductivity, around the taper area. $t_{stop} = 82.78$ ps.

The Delaunay mesh used here has about 40000 triangles, and the stop time of the simulation is set to $t_{stop} = 82.78$ ps as it gives a steady state temperature at the tip. Fig. 6.4.4a shows a temperature rise of approximately 16°C at the tip area, which is close to the simulation results shown in [96] (approximately 15°C). Fig. 6.4.4b shows that the power density generated at the interface between the silicon waveguide and the gold wall due to Joule heating. The magnitude of this Joule heating power on average matches the result given in [96] (approximately $7 \times 10^{17} \mathrm{W} \cdot \mathrm{m}^{-3}$). The E_y component of the electric field is presented in Fig. 6.4.4c showing the optical mode that is propagating in the silicon waveguide, and its singular behaviour at the tip of the waveguide demonstrates that the digital filter (6.3.33) can evaluate the EM field correctly and stably.

The way to calculate the simulated effective electrical conductivity is similar to

(6.4.2), but the electric field strength is now vector, leading to

$$\sigma_{e,eff}(\text{simulated}) = \frac{\left(\sum_{i=1}^{N_T} P[i]\right)/N_T}{\left(\sum_{i=1}^{N_T} |\boldsymbol{E}[i]|^2\right)/N_T}, \tag{6.4.6}$$

where N_T is the number of simulation time steps.

As is shown in Fig. 6.4.4d, the effective conductivity of gold evaluated by the coupled UTLM method is approximately 130000 S/m, and it is very close to the theoretical value 130815 S/m obtained in (6.4.1), which demonstrates that the digital filters (6.3.12) and (6.3.13) can generate correct plasma electrical conductivity under real engineering scenarios according to the wave frequency. It also shows the impact of using the Drude model of plasma because otherwise the conductivity of gold may be modelled as a constant instead of a frequency-dependent value.

6.5 Conclusion

The implementation of the Drude plasma model in two-dimensional TE series Cartesian TLM method is derived, and the result agrees with the conclusion in [37]. The implementation of the Drude model in 2D TE series UTLM method is proposed; a significant step from the previous TLM work is highlighted to be the use of an unstructured, rather than a Cartesian mesh. The Joule heating power density evaluation formula is validated by both a separate 1D test and the simulation of a 2D real engineering application case of the plasmonic nanotip waveguide. The nanotip waveguide test also shows that the frequency-dependent permittivity of plasma is successfully embodied in the proposed implementation scheme, and the one-way electrothermal coupled UTLM method can provide the correct the temperature rise. The two-way fully coupled electrothermal UTLM method will be introduced next in Chapter 7.

Chapter 7

Coupled UTLM and Applications on Lightning Protection

In this chapter, a two-way electrothermal coupled scheme for plasma simulation is proposed. This scheme is based on the EM UTLM method and the thermal UTLM method; the frequency-dependent plasma permittivity is supported in this scheme, and the plasma parameters are updated in each iteration according to the temperature profile. This method is, then, used to analyse the direct effects of lightning strikes on segmented lightning diverter strips. The proposed method is able to predict the time to breakdown of a range of different segmented diverters, and the results are compared with [98]. Comments on different diverter strips designs are made based on simulation results.

7.1 Overview

The discharge process during lightning strikes are classified as DC discharges, and it is the most common DC discharge process at atmospheric pressure [99]. Before the DC breakdown, the streamer, as a result of the condensation of charges, is gradually formed from one electrode towards the other electrode; in the context of lightning strikes, it is from the cloud to the ground. When the streamer approaches the opposite electrode, the ionised discharge channel is completely developed, and a strong return current with other subsequent currents will flash through this channel.

The threshold electric field strength to cause the breakdown depends on the pressure according to Paschen's law.

Whilst the detailed breakdown process can be described using atomistic models [93, 99], those models are not suitable for use in the engineering context of lighting protection design for which a macroscopic model of lightning is more appropriate. Coupled electrothermal numerical methods for arc discharge modelling involves solving both the electromagnetic field and the fluid behaviour of plasma, although few of them solve the full EM and fluid governing equations. Magnetohydrodynamic (MHD) plasma models [41, 43, 98, 100, 101] are popular among these methods. However, the dispersive characteristic of the plasma results in its frequency-dependent permittivity, which is not easy to be considered in MHD-based schemes. The Drude model [37, 44–47] is another approach to describe the plasma characteristics, and the implementation of the Drude model in TLM methods have been introduced in Chapter 6. Both MHD models and the Drude model can be used to investigate the lightning strike and its effects, but different from MHD-based methods, the Drude-model-based schemes do not need to pre-define the plasma arc channel on account of full electrodynamics, and the arc channel is naturally formed when the amplitude of the local electric field exceeds a critical value [37].

In this work, the 2D UTLM is used to develop a fully coupled multiphysical electrothermal solver. The 2D EM UTLM method (see Section 4.4 and [94]) is coupled to the 2D thermal UTLM method (see Chapter 5 and [102]) to provide the link between the plasma parameters and the real-time temperature. It is convenient to use the EM and the thermal UTLM together because they share the same Delaunay and Voronoi mesh [72, 73] and hence the positions of node centres and ports so that no re-sampling of the EM field and the temperature profile is needed during the two-way coupling. Two-way electrothermal coupling is described in this work, as the resistive heating of plasma gives the temperature increase, and the temperature affects the plasma parameters. One of the main advantages of TLM methods is its unconditional stability [62] which makes it ideally suitable

for multiphysics simulations. The advantages and demands of using unstructured meshes have been widely explained, especially when curved material interfaces and boundaries are involved.

7.2 Two-way Electrothermal Coupling

This proposed method predicts the formation of the discharge channel by solving the electromagnetic field and the temperature before, during and after the air breaks down. The EM UTLM method and the thermal UTLM method are executed iteratively, and this coupling scheme is presented in Fig. 7.2.1. In this proposed method, the thermal effects are not considered before the breakdown because before the breakdown, the electron temperature rises significantly while the heavy particle temperature changes insignificantly [93, 99]. Plasma that forms in the arc discharge process is often a thermal plasma that satisfies thermal equilibrium dependent on the pressure [93]. Other works such as [37, 41, 43] also make the assumption of thermal equilibrium.

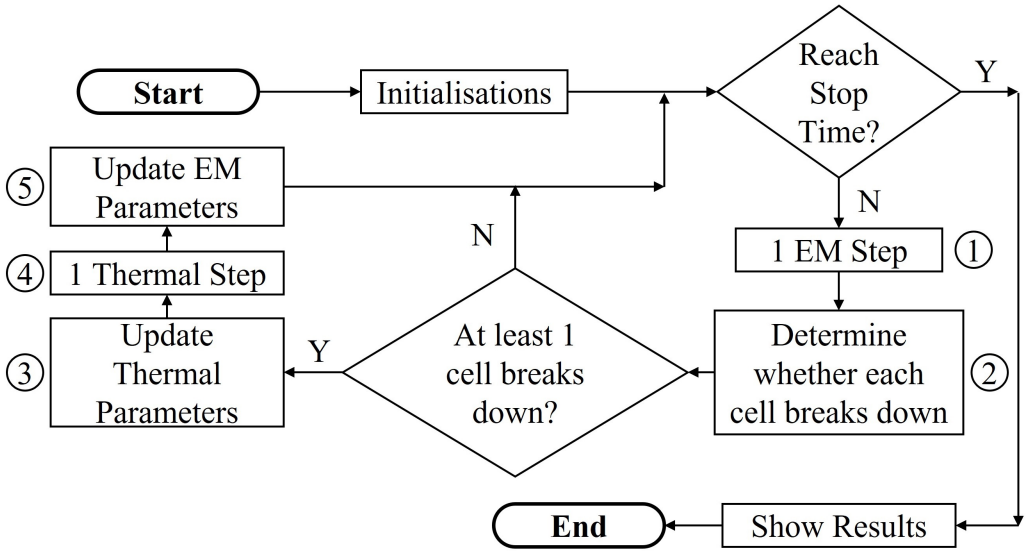

Fig. 7.2.1: Flowchart of the two-way electrothermal coupling scheme

The algorithm begins with initialisations (e.g. setting up the source electric field). In step 1, (6.3.33) is used to evaluate the middle voltage at each port, while the scattering and connection equations at node centres (i.e. (4.4.23), (4.4.24), (4.4.25) and (4.4.26)) remain the same. In step 2, a fixed total electric field strength

threshold of $E_b = 25\text{kV/cm}$ [37] is used to determine whether an air node transforms into an air plasma node. In step 3, (6.3.12) and (6.3.13) are used to evaluate the resistive heating power density at each node. Note that in step 2 and step 3, the orthogonal components of the electric field at each node are required, and the associated evaluation method is covered in Section 4.4.8. In step 4, the current source terms in the thermal UTLM formulation are calculated based on the resistive heating power density calculated in step 3, and the temperature profile in the computational domain is updated accordingly. In step 5, the plasma frequency ω_p, the electron-ion collision frequency ν_c and the electron density n_e are updated according to the new temperature T using (6.1.8) (6.1.14) and (6.2.3).

7.3 Results

7.3.1 Two Lightning Strip Buttons

In this section, the coupled UTLM method is applied to the simulation of the lightning channel between segmented lightning diverter strips. This coupled UTLM method uses the TE series version of the EM UTLM method and the thermal UTLM method, both of which are proposed in this thesis. In the first instance, the problem considers two basic elements of segmented lightning diverter strips, namely two circular aluminium buttons of diameter 3.5 mm separated by 0.5 mm. The problem is excited by an electric field source placed at the right boundary, which is illustrated in Fig. 7.3.1.

The source electric field is placed at $x = 8.5$ mm and is in the negative x-direction (i.e. $\boldsymbol{E} = (-E_x, 0)$). Following the temporal waveform shape suggested in [103], it is defined as

$$E_x(t) = 2.2 \times 10^8 \left(e^{-16065t} - e^{-858888t}\right). \tag{7.3.1}$$

The plasma parameters (n_e, ω_p and ν_c) are all updated according to the temperature, giving two-way electrothermal coupling. When a simple air node is turned into an air plasma node, a base temperature is set to pre-heat it, but no discharge channel is presumed because it is the real-time electric field strength that

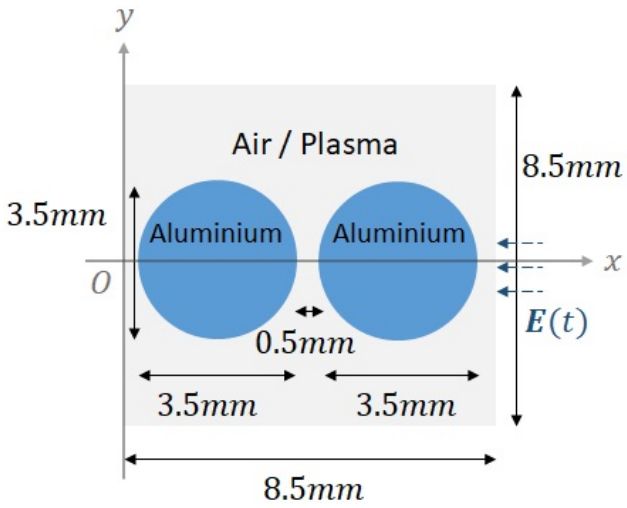

Fig. 7.3.1: The schematic of two circular aluminium buttons

determines the breakdown of an air node. The pre-heating base temperature is chosen to be 5100 K according to [93].

The associated thermal parameters of plasma, aluminium and air are listed in Table 7.3.1.

Table 7.3.1: Thermal Parameters Setup

	Plasma	Aluminium	Air
k_{th} (W/(m · K))	0.8	237	0.0262
ρ_m (kg/m^3)	0.057	2707	1.2928
c_p (J/(kg · K))	2940	897	1005

The stop time is set to $t_{stop} = 65$ ns, and Fig. 7.3.2 shows the temperature increase caused by the burning plasma channel. This channel connects two aluminium buttons and is approximately 1.5 mm wide in the y-direction. The highest temperature rise of approximately 150 K is observed at the centre of the channel. The slight temperature increase close to the left-side boundary is the numerical artefact caused by the very short distance between the circle button and the boundary.

Fig. 7.3.3 compares the results of the temperature rise across the plasma channel obtained by different mesh densities in two cross-sections, namely the cross-section at $x = 4.25$ mm (Fig. 7.3.3a) and the cross-section at $y = 0$ (Fig. 7.3.3b). Fig. 7.3.3a shows that the temperature in the plasma channel rises sharply away from the aluminium buttons. The coarsest mesh (2396 triangles) only captures

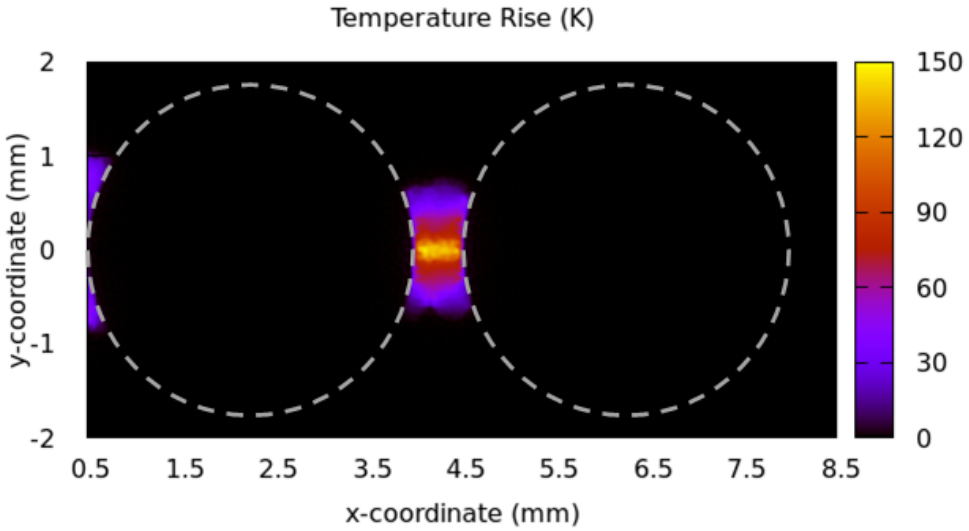

Fig. 7.3.2: Temperature increase obtained using the Delaunay mesh with 20980 triangles. $t_{stop} = 65$ ns.

the crude shape of the temperature distribution, but as the mesh becomes finer ($\geq$11729 triangles), simulations using meshes with different numbers of triangles converge to a stable temperature distribution with a maximum temperature of 150 K. Fig. 7.3.3b shows that the temperature distribution of the plasma channel is more slowly changing across its width and that the overall width of the plasma channel is approximately 1.5 mm. Note that the temperature distribution is not quite symmetric due to the fact that the sampling mesh is not strictly symmetric, but, as expected, this phenomenon reduces for denser meshes.

This test demonstrates that the two-way electrothermal coupled algorithm proposed in this work can predict the arc discharge channel reasonably and stably when curved material interfaces and different mesh densities are involved.

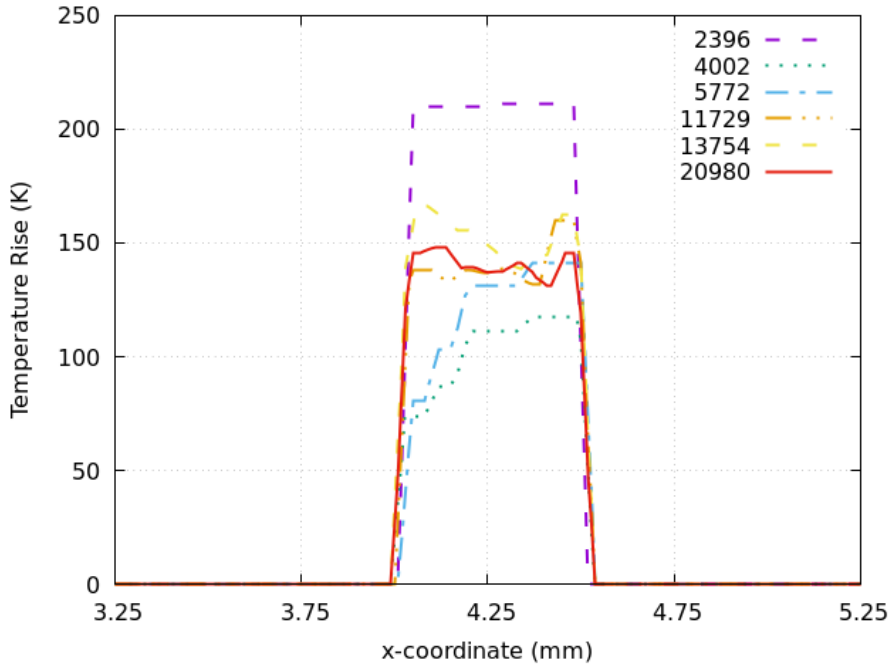

(a)

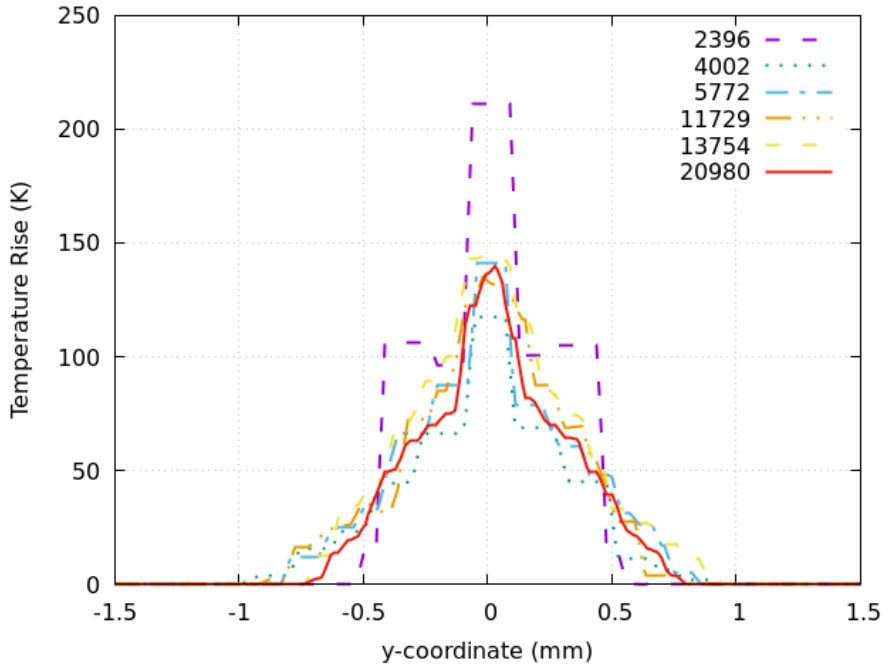

(b)

Fig. 7.3.3: (a) The x-direction slice at $y = 0$ (b) The y-direction slice at $x = 4.35$ mm, of the temperature increase obtained using Delaunay meshes with different numbers of triangles. $t_{stop} = 65$ ns.

Fig. 7.3.4 presents a similar problem but with square buttons, rotated by an angle θ with respect to the x-axis and with all other parameters kept the same. Similar to the analysis in [98], Fig. 7.3.5 presents the time to breakdown for different orientation of square buttons.

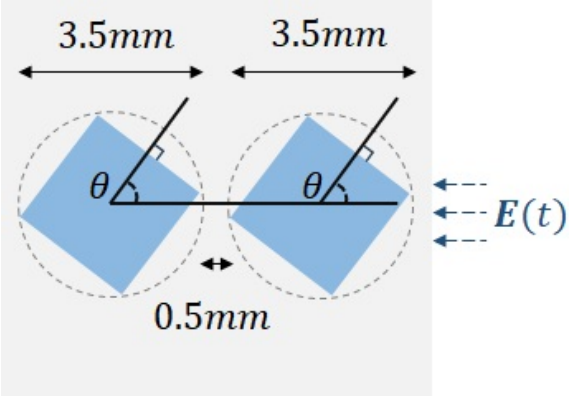

Fig. 7.3.4: The schematic of two rotated square aluminium buttons

The time to breakdown of an air-gap is defined as the first time frame when at least one complete plasma arc (i.e. a channel formed by only plasma cells) has developed between the buttons. The proposed electrothermal coupled algorithm is used to obtain the time to breakdown, and Fig. 7.3.5 illustrates the trend as the rotation angle varies. Each individual Delaunay mesh used in this group of simulations has approximately 13000 triangles.

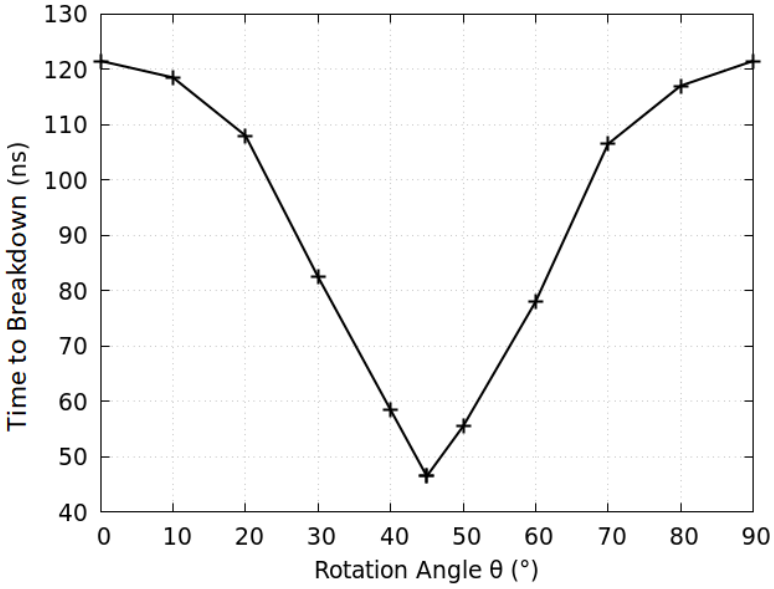

Fig. 7.3.5: Time to breakdown using different rotation angles

It is seen that a rotation angle of 45 degrees gives the shortest time to breakdown since the two square corners where singularities of the electric field occur speed up the establishment of the plasma channel. The breakdown instant when the buttons are rotated 10 degrees is close to that of the 80 degrees case because these two layouts are geometrically symmetrical, so do 20 degrees vs. 70 degrees, 30 degrees vs. 60 degrees and so on. The time to breakdown positively correlates with the breakdown voltage because before and during the breakdown, the applied voltage or the electric field strength is monotonically increasing. Therefore, Fig. 7.3.5 agrees with the results presented in [98] which also concludes that a rotation angle closer to 45 degrees makes the air-gap easier to breakdown.

7.3.2 Lightning Diverter Strips Designs

In this section, the coupled UTLM method is applied to analyse the effectiveness of different lightning diverter strips designs. Five designs illustrated in Fig. 7.3.6 are considered, and the dimensions are referred to the manufacturing parameters specified in [13]. The segmented diverters are described using five differently shaped buttons, namely large and small circles, ellipses, aligned squares and rotated squares. All buttons are aluminium with the same thermal parameters as those stated in Section 7.3.1. The source electric field is placed at the right-hand boundary and is given as (7.3.1).

The time to breakdown of each gap for each design is recorded and compared in Table 7.3.2 and Fig. 7.3.7. A good design exhibits a rapid breakdown between the diverter segments after the lightning hits them. It is seen that segmented diverters with aligned squares lead to the longest time to breakdown, and hence are less ideal for the practical application, whilst those with ellipses and rotated squares have faster time to breakdown and hence perform better for lightning protections. Furthermore, large circles provide an average performance, whilst small circles outperform the others in this test because they have smaller air-gaps. It is noted that as the buttons are all placed in air, the results in Fig. 7.3.7 only show the impact of the button shape on the breakdown instant not of the supporting material.

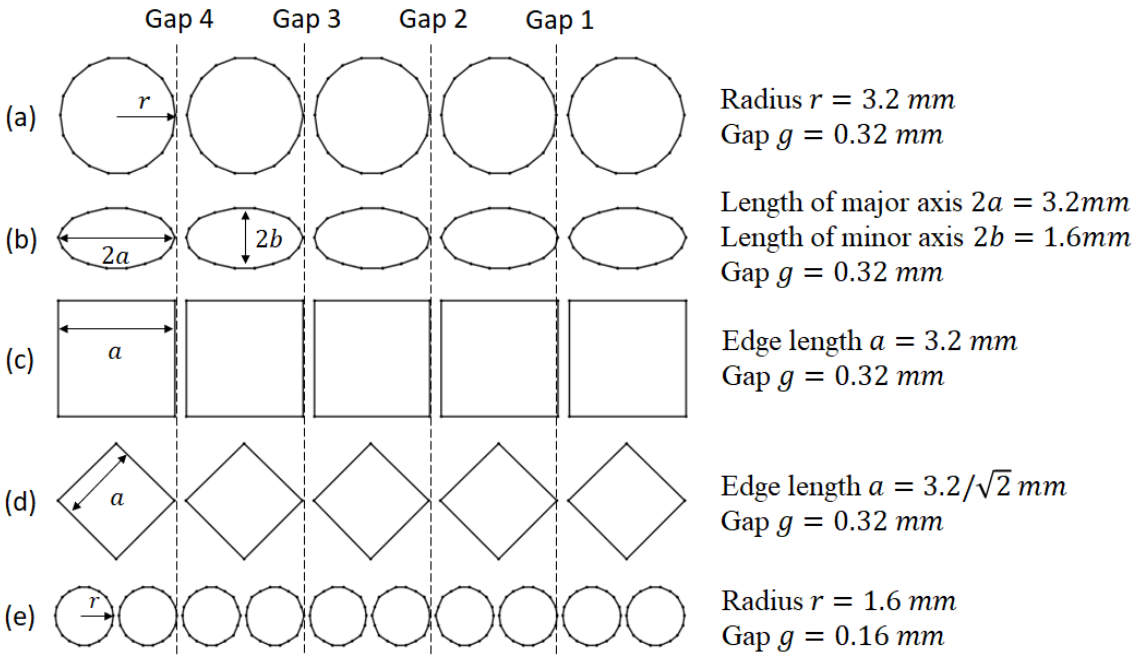

Fig. 7.3.6: The schematics of different designs: (a) 5 large circles, (b) 5 ellipses, (c) 5 aligned squares, (d) 5 rotated squares, (e) 10 small circles.

Table 7.3.2: Time to breakdown of Different Designs (Unit: ns)

	Gap 1	Gap 2	Gap 3	Gap 4
5 circles	49.6	50.1	50.3	50.5
5 ellipses	42.0	42.3	42.6	42.7
5 aligned squares	**56.6**	**57.1**	**57.3**	**57.4**
5 rotated squares	40.2	40.6	40.9	41.0
10 circles	**29.8**	**31.6**	**34.6**	**35.3**

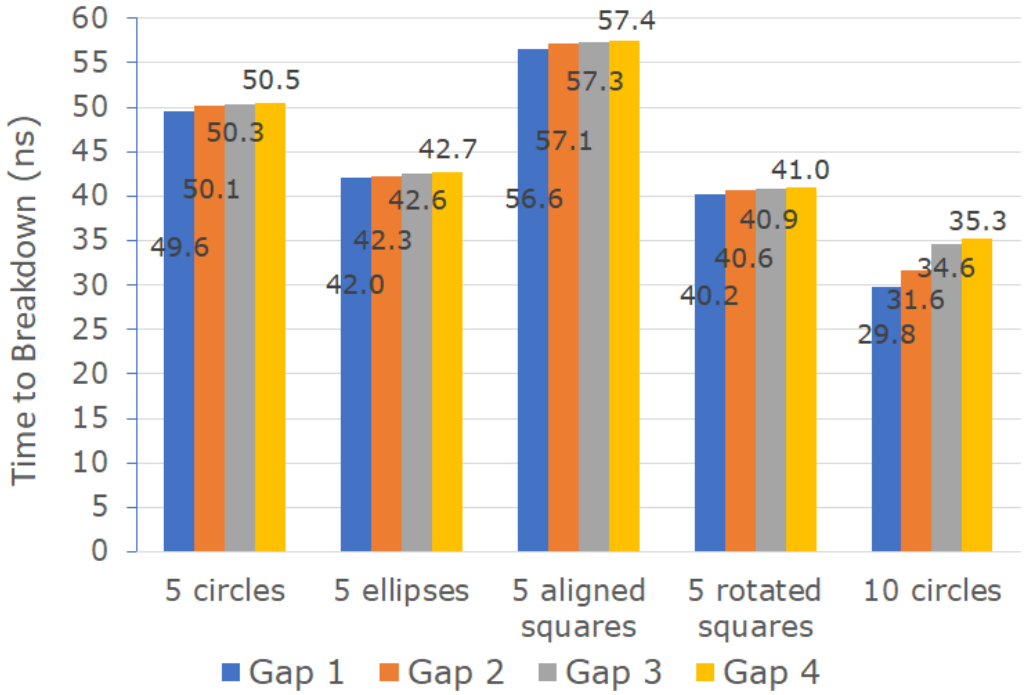

Fig. 7.3.7: Time to breakdown of each gap in different designs

7.4 Conclusion

A fully coupled electrothermal method based on the UTLM framework for modelling lightning protection and plasma arc formation has been presented. The formulation of both the EM and the thermal solvers within the UTLM framework avoids interpolation or re-sampling and thus guarantees the overall stability of the algorithm. Furthermore, the breakdown of air between two circular and square elements of lightning diverter strips is analysed. It is shown that the proposed method can predict the formation of the arc channel and its temperature distribution in a stable manner. Finally, this method is extended to analyse the effectiveness of differently shaped buttons in segmented lightning diverter strips designs, and the results show that small round buttons outperform other designs as they have the fastest time to breakdown that is needed for an efficient and safe diversion of the lightning current.

Chapter 8

Conclusions and Future Work

8.1 Summary of the Thesis

The aim of this project was to develop a two-dimensional two-way electrothermal coupled numerical method to analyse plasma behaviours and the breakdown of air, and this aim has been achieved via coupling the Drude-embedded TE series electromagnetic UTLM method with the thermal UTLM method. The newly-developed coupled scheme is able to analyse different segmented lightning diverter designs.

In Chapter 1, the aim and motivation of this project have been explained, followed by a review of existing works about electrothermal numerical models and plasma models. Then, the Cartesian electromagnetic TLM method, the Cartesian thermal TLM method and the two-dimensional shunt UTLM method have been reviewed and introduced in Chapter 2, Chapter 3 and Chapter 4 respectively; alternative ways to derive some of these existing numerical methods have been provided, and the scattering and connection process has been explained in detail.

The two-dimensional TE series UTLM method and the two-dimensional thermal UTLM method have been developed and presented in Chapter 4 and Chapter 5 respectively; these newly-developed numerical methods are based on unstructured triangular meshes, and they have been validated in terms of their correctness and convergence. The Delaunay triangular mesh and the triangulation algorithm have also been covered in Chapter 4.

Next, the Drude plasma model and the way to embed it into the electromagnetic UTLM method have been covered and derived in Chapter 6. The Drude-embedded electromagnetic UTLM method has been validated using the simulation of a plasmonic nanotip waveguide, and the capability to support the frequency-dependent plasma permittivity has been witnessed.

Lastly, the two-way coupled electrothermal plasma model has been presented in Chapter 7. This proposed scheme supports unstructured triangular meshes, and its stability has been examined using the mesh independent test. This two-way coupled scheme uses the Drude-embedded EM UTLM method and the thermal UTLM method together so that no re-sampling of the EM field and the temperature is required during the coupling process. The effectiveness of different lightning diverter strips designs is evaluated as well via taking use of this electrothermal model.

8.2 Future Work

Although the two-way electrothermal coupled plasma model proposed in this thesis is able to provide reasonable results in real engineering applications, there are still some aspects that can be improved.

Firstly, the model developed in this thesis does not consider the particle transport in the plasma and the heat radiation of plasma. These behaviours are included in MHD-based methods, but are not easy to be considered in electrodynamics based methods (e.g. EM and thermal UTLM methods) because modelling the particle transport requires solving fluid PDEs. A hybrid model combining the fluid dynamics and the electrodynamics is possible, although the model complexity would be high. Secondly, constant thermal parameters of plasma are assumed in this thesis. The explicit expressions of plasma parameters are not easy to obtain, as we have seen when interpolating $n_e(T)$ in Section 6.2, so tabulated equations of state might be required. In addition, different waveforms of the input electric field could be used as the lightning strike model to investigate the influence on the time to breakdown caused by different frequency components. Furthermore, the methodology guiding

the derivation of the Drude model implementation in two-dimension could be utilised to produce the three-dimensional Drude-embedded unstructured TLM method based upon tetrahedral meshes.

This concludes the future work and the thesis as a whole.

Bibliography

[1] F. A. Fisher and J. A. Plumer, *Lightning Protection of Aircraft*. NASA Lewis Research Center, Apr 1977.

[2] Boeing, *AERO QTR_04.12.pdf*. The Boeing Company, 2012.

[3] F. A. Fisher, J. A. Plumer, and R. A. Perala, *Aircraft Lightning Protection Handbook*. Federal Aviation Administrations Technical Center, Sep 1989.

[4] C. C. Goodloe, *Lightning Protection Guidelines for Aerospace Vehicles*. NASA Marshall Space Flight Center, May 1999.

[5] C. Soutis, "Carbon fiber reinforced plastics in aircraft construction," *Materials Science and Engineering: A*, vol. 412, no. 1, pp. 171–176, 2005. International Conference on Recent Advances in Composite Materials.

[6] P. Rajesh, F. Sirois, and D. Therriault, "Damage response of composites coated with conducting materials subjected to emulated lightning strikes," *Materials & Design*, vol. 139, pp. 45–55, 2018.

[7] V. Bedel, A. Lonjon, E. Dantras, and M. Bouquet, "Innovative conductive polymer composite coating for aircrafts lightning strike protection," *Journal of Applied Polymer Science*, vol. 137, no. 20, p. 48700, 2020.

[8] W. Jing, L. Dichen, Z. Jiangfeng, and Z. Wei, "The calculating and analysis of shielding effectiveness of metal meshes in transient electromagnetic interference," in *Asia-Pacific Conference on Environmental Electromagnetics, 2003. CEEM 2003. Proceedings.*, pp. 379–385, 2003.

[9] Z. Guo, W. Yu, Z. Fang, M. Zhang, H. Li, Q. Li, and W. H. Siew, "The influence of the metal mesh to the attachment manner of cfrp wind turbine blades," in *2019 11th Asia-Pacific International Conference on Lightning (APL)*, pp. 1–4, 2019.

[10] Y. Duan, X. Xiong, and P. Hu, "Research on aircraft radome lightning protection based on segmented diverter strips," in *2017 International Symposium on Electromagnetic Compatibility - EMC EUROPE*, pp. 1–6, 2017.

[11] A. Vukovic, P. Sewell, and T. M. Benson, "Impact of in situ radome lightning diverter strips on antenna performance," *IEEE Transactions on Antennas and Propagation*, vol. 68, no. 11, pp. 7287–7296, 2020.

[12] A. Muto, J. Suzuki, and T. Ueda, "Performance comparison of wind turbine blade receptor for lightning protection," in *2010 30th International Conference on Lightning Protection (ICLP)*, pp. 1–6, 2010.

[13] Y. Zheng, A. Vukovic, P. Sewell, and A. Hall, "EM performance of segmented diverter strips used in lightning protection of wind turbine blades," in *2021 Asia-Pacific International Symposium on Electromagnetic Compatibility (APEMC)*, pp. 1–4, 2021.

[14] L. Pichon and O. Meyer, "Coupled thermal-electromagnetic simulation of a microwave curing cell," *IEEE Transactions on Magnetics*, vol. 38, no. 2, pp. 977–980, 2002.

[15] A. Lahlalia, O. Le Neel, R. Shankar, S. Y. Kam, and L. Filipovic, "Electro-thermal simulation & characterization of a microheater for SMO gas sensors," *Journal of Microelectromechanical Systems*, vol. 27, no. 3, pp. 529–537, 2018.

[16] J. Clemens and C. Saltiel, "Numerical modeling of materials processing in microwave furnaces," *International Journal of Heat and Mass Transfer*, vol. 39, no. 8, pp. 1665–1675, 1996.

[17] E. F. Toro, *Riemann Solvers and Numerical Methods for Fluid Dynamics*. Springer, 2009.

[18] B. Sun, X. Ye, C. Wang, M. Qi, and G. Zhai, "Research on electro-thermal coupling simulation platform of switching mode power supply," in *2015 First International Conference on Reliability Systems Engineering (ICRSE)*, pp. 1–5, 2015.

[19] S. S. Attar, M. Yagoub, and F. Mohammadi, "New electro-thermal integrated circuit modeling using coupling of simulators," in *2006 Canadian Conference on Electrical and Computer Engineering*, pp. 1218–1222, 2006.

[20] M. A. Baferani, T. Shahsavarian, C. Li, M. Tefferi, I. Jovanovic, and Y. Cao, "Electric field tailoring in HVDC cable joints utilizing electro-thermal simulation: effect of field grading materials," in *2020 IEEE Electrical Insulation Conference (EIC)*, pp. 400–404, 2020.

[21] Y. Jiang, D. Wang, Q. Zhang, and J. Chen, "Electromagnetic-thermal coupling simulation by ANSYS Multiphysics of induction heater," *Applied Mechanics and Materials*, vol. 701-702, pp. 820–825, Dec 2014.

[22] P. Y. Chen, H. H. Zhang, W. E. Sha, and D. Z. Ding, "Transient electromagnetic-thermal co-simulation based on DGTD method," in *2019 International Applied Computational Electromagnetics Society Symposium - China (ACES)*, vol. 1, pp. 1–2, 2019.

[23] P. Wang, P. Chen, W. Sha, and H. Zhang, "Large-scale parallel DGTD and FETD method for transient microwave heating," in *2020 IEEE MTT-S International Conference on Numerical Electromagnetic and Multiphysics Modeling and Optimization (NEMO)*, pp. 1–3, Dec 2020.

[24] F. Denz, E. Gjonaj, T. Weiland, M. Tuczek, and V. Hinrichsen, "Electric and thermal reaction of zinc oxide to current impulses," in *2010 30th International Conference on Lightning Protection (ICLP)*, pp. 1–5, 2010.

[25] Y. Spaeck-Leigsnering, M. Koch, C. Bergfried, E. Gjonaj, H. De Gersem, and M. Heckel, "Electrothermal finite element analysis of a pluggable high voltage surge arrester," in *VDE High Voltage Technology 2020; ETG-Symposium*, pp. 1–7, 2020.

[26] Y. Späck-Leigsnering, E. Gjonaj, H. De Gersem, T. Weiland, M. Gießel, and V. Hinrichsen, "Investigation of thermal stability for a station class surge arrester," *IEEE Journal on Multiscale and Multiphysics Computational Techniques*, vol. 1, pp. 120–128, 2016.

[27] T. Kojima, Y. Yamada, Y. Nishibe, and K. Torii, "Novel RC compact thermal model of HV inverter module for electro-thermal coupling simulation," in *2007 Power Conversion Conference - Nagoya*, pp. 1025–1029, 2007.

[28] V. Szekely, A. Poppe, and G. Hajas, "Electro-thermal transistor models in the SISSI electro-thermal IC simulator," in *Proceedings of the 5th International Conference on Thermal and Mechanical Simulation and Experiments in Microelectronics and Microsystems, 2004. EuroSimE 2004.*, pp. 105–112, 2004.

[29] P. Liu and V. Dinavahi, "Real-time finite-element simulation of electromagnetic transients of transformer on FPGA," *IEEE Transactions on Power Delivery*, vol. 33, no. 4, pp. 1991–2001, 2018.

[30] P. Liu, N. Lin, and V. Dinavahi, "Integrated massively parallel simulation of thermo-electromagnetic fields and transients of converter transformer interacting with MMC in multi-terminal DC grid," *IEEE Transactions on Electromagnetic Compatibility*, vol. 62, no. 3, pp. 725–735, 2020.

[31] P. W. Webb and I. A. D. Russell, "Application of the TLM method to transient thermal simulation of microwave power transistors," *IEEE Transactions on Electron Devices*, vol. 42, no. 4, pp. 624–631, 1995.

[32] R. Hocine, M. A. Boudghene Stambouli, and A. Saidane, "A three-dimensional TLM simulation method for thermal effect in high power insulated gate bipolar transistors," in *Eighteenth Annual IEEE Semiconductor*

Thermal Measurement and Management Symposium. Proceedings 2002 (Cat.No.02CH37311), pp. 99–104, 2002.

[33] A. Al-Dabbagh, H. G. Sasse, M. Al-Asadi, and A. Duffy, "Modeling thermal radiation effects in nanowires using the TLM method," *IEEE Transactions on Nanotechnology*, vol. 12, no. 6, pp. 1118–1124, 2013.

[34] A. Aldabbagh and A. Duffy, "Ageing effects on power RF LDMOS reliability using the transmission line matrix method," in *2015 10th International Workshop on the Electromagnetic Compatibility of Integrated Circuits (EMC Compo)*, pp. 157–162, 2015.

[35] C. Flockhart, V. Trenkic, and C. Christopoulos, "The simulation of coupled electromagnetic and thermal problems in microwave heating," in *1994 Second International Conference on Computation in Electromagnetics*, pp. 267–270, 1994.

[36] C. Christopoulos, "The application of time-domain numerical simulation methods to the microwave heating of foods," *IMA Journal of Management Mathematics*, vol. 5, pp. 385–397, Jan 1993.

[37] A. Elkalsh, P. Sewell, T. M. Benson, and A. Vukovic, "Coupled electrothermal two-dimensional model for lightning strike prediction and thermal modeling using the TLM method," *IEEE Journal on Multiscale and Multiphysics Computational Techniques*, vol. 2, pp. 38–48, Mar 2017.

[38] H.-Y. Lee, Y.-S. Kim, W.-S. Lee, H.-K. Kim, and S.-H. Lee, "Fully coupled finite element analysis for cooling effects of dielectric liquid due to ionic dissociation stressed by electric field," *IEEE Transactions on Magnetics*, vol. 49, no. 5, pp. 1909–1912, 2013.

[39] H.-Y. Lee, I. M. Kang, and S.-H. Lee, "Fully coupled finite-element analysis for surface discharge on solid insulation in dielectric liquid with experimental validation," *IEEE Transactions on Magnetics*, vol. 52, no. 3, pp. 1–4, 2016.

[40] F. Tholin, L. Chemartin, and P. Lalande, "Numerical investigation of the interaction of a lightning and an aeronautic skin during the pulsed arc phase," *IET Conference Proceedings*, pp. 39 (6 .)–39 (6 .)(1), Jan 2015.

[41] A. Villa, R. Malgesini, and L. Barbieri, "A multiscale technique for the validation of a numerical code for predicting the pressure field induced by a high-power spark," *Journal of Physics D: Applied Physics*, vol. 44, p. 165201, Apr 2011.

[42] L. Chemartin, P. Lalande, C. Delalondre, B. Cheron, and F. Lago, "Modelling and simulation of unsteady DC electric arcs and their interactions with electrodes," *Journal of Physics D: Applied Physics*, vol. 44, p. 194003, Apr 2011.

[43] L. Chemartin, P. Lalande, B. Peyrou, A. Chazottes, P. Elias, C. Delalondre, B. Cheron, and F. Lago, "Direct Effects of Lightning on Aircraft Structure: Analysis of the Thermal, Electrical and Mechanical Constraints," *Aerospace Lab*, pp. p. 1–15, Dec 2012.

[44] L. D. Landau, E. M. Lifshitz, J. Sykes, J. S. Bell, and E. H. Dill, *Electrodynamics of Continuous Media, Volume 8, 2nd Edition.* Pergamon, 1984.

[45] R. J. Luebbers, F. Hunsberger, and K. S. Kunz, "A frequency-dependent finite-difference time-domain formulation for transient propagation in plasma," *IEEE Transactions on Antennas and Propagation*, vol. 39, pp. 29–34, Jan 1991.

[46] N. Dončov, T. Asenov, Z. Stanković, and J. Paul, "Time-domain modelling of graded refractive index metamaterials by using 3D TLM Z-transform method," in *2011 10th International Conference on Telecommunication in Modern Satellite Cable and Broadcasting Services (TELSIKS)*, vol. 1, pp. 35–38, 2011.

[47] D. Kalluri and J. Lee, "FDTD simulation of electromagnetic wave transformation in a dynamic, inhomogeneous, bounded, and magnetized

plasma," in *IEEE Conference Record - Abstracts. 1999 IEEE International Conference on Plasma Science. 26th IEEE International Conference (Cat. No.99CH36297)*, pp. 141–, 1999.

[48] D. K. Cheng, *Field and Wave Electromagnetics*. Pearson, 2 ed., 1989.

[49] G. F. Abdelal and A. Murphy, "A multiphysics simulation approach for efficient modeling of lightning strike tests on aircraft structures," *IEEE Transactions on Plasma Science*, vol. 45, no. 4, pp. 725–735, 2017.

[50] Y. Liu and Y. Wang, "Is indirect electrode a good choice for simulated lightning damage tests?-the effect of metal vapor," *IEEE Transactions on Plasma Science*, vol. 49, no. 5, pp. 1661–1668, 2021.

[51] D. B. S. Audiffred, X. L. Travassos, T. S. Possamai, and N. Ida, "Numerical code for modeling electrothermal effects of lightning strike on CFRP composites," *IEEE Transactions on Magnetics*, vol. 56, no. 3, pp. 1–4, 2020.

[52] J. Schneider and S. Hudson, "A finite-difference time-domain method applied to anisotropic material," *IEEE Transactions on Antennas and Propagation*, vol. 41, no. 7, pp. 994–999, 1993.

[53] K. Yee, "Numerical solution of initial boundary value problems involving maxwell's equations in isotropic media," *IEEE Transactions on Antennas and Propagation*, vol. 14, no. 3, pp. 302–307, 1966.

[54] D. B. Davidson, *Computational Electromagnetics for RF and Microwave Engineering*. Cambridge University Press, 2 ed., 2010.

[55] D. L. Logan, *A First Course in the Finite Element Method*. Cengage Learning, 6 ed., 2016.

[56] K. Kaiser, *Electromagnetic Compatibility Handbook*. Electrical engineering handbook series, Taylor & Francis, 2004.

[57] C. Christopoulos, *The Transmission-Line Modeling Method: TLM*. Wiley-IEEE Press, 1995.

[58] A. Faul, *A Concise Introduction to Numerical Analysis*. Taylor & Francis Inc, Mar 2016.

[59] J. Breil and P.-H. Maire, "A cell-centered diffusion scheme on two-dimensional unstructured meshes," *Journal of Computational Physics*, vol. 224, pp. 785–823, 2006.

[60] P.-H. Maire and J. Breil, "A high-order finite volume cell-centered scheme for anisotropic diffusion on two-dimensional unstructured grids," *Journal of Computational Physics*, vol. 11, pp. 76–15, 2011.

[61] D. de Cogan, "Propagation analysis for thermal modeling," *IEEE Transactions on Components, Packaging, and Manufacturing Technology: Part A*, vol. 21, no. 3, pp. 418–423, 1998.

[62] P. B. Johns, "A simple explicit and unconditionally stable numerical routine for the solution of the diffusion equation," *International Journal for Numerical Methods in Engineering*, vol. 11, no. 8, pp. 1307–1328, 1977.

[63] A. Amri, A. Saidane, and S. Pulko, "Thermal analysis of a three-dimensional breast model with embedded tumour using the transmission line matrix (TLM) method," *Computers in Biology and Medicine*, vol. 41, no. 2, pp. 76–86, 2011.

[64] H. Milan and K. Gebremedhin, "Triangular node for transmission-line modeling (TLM) applied to bio-heat transfer," *Journal of Thermal Biology*, vol. 62, pp. 116–122, 2016.

[65] D. de Cogan and A. de Cogan, *Applied Numerical Modelling for Engineers*. Oxford Science Publications, 1997.

[66] W. Yu and R. Mittra, "A conformal finite difference time domain technique for modeling curved dielectric surfaces," *IEEE Microwave and Wireless Components Letters*, vol. 11, no. 1, pp. 25–27, 2001.

[67] C. Argyropoulos, Y. Zhao, and Y. Hao, "A radially-dependent dispersive finite-difference time-domain method for the evaluation of electromagnetic

cloaks," *IEEE Transactions on Antennas and Propagation*, vol. 57, no. 5, pp. 1432–1441, 2009.

[68] A. Diaz-Morcillo, L. Nuño, J. Balbastre, and D. Sánchez-Hernández, "Adaptive mesh refinement in electromagnetic problems.," in *In 9th International Meshing Roundtable*, pp. 147–155, Jan 2000.

[69] F. Meyer and D. Davidson, "Adaptive-mesh refinement of finite-element solutions for two-dimensional electromagnetic problems," *IEEE Antennas and Propagation Magazine*, vol. 38, no. 5, pp. 77–83, 1996.

[70] C. Christopoulos, *The Transmission-line Modeling (TLM) Method in Electromagnetics*. Synthesis lectures on computational electromagnetics, Morgan & Claypool Publishers, 2006.

[71] P. Sewell, J. G. Wykes, T. M. Benson, C. Christopoulos, D. W. P. Thomas, and A. Vukovic, "Transmission-line modeling using unstructured triangular meshes," *IEEE Transactions on Microwave Theory and Techniques*, vol. 52, no. 5, pp. 1490–1497, 2004.

[72] J. R. Shewchuk, "Triangle: A two-dimensional quality mesh generator and Delaunay triangulator." `https://www.cs.cmu.edu/~quake/triangle.html`.

[73] E. Tonti, "Finite formulation of electromagnetic field," *IEEE Transactions on Magnetics*, vol. 38, no. 2, pp. 333–336, 2002.

[74] S.-W. Cheng, T. K. Dey, and J. Shewchuk, *Delaunay Mesh Generation*. Chapman & Hall/CRC, 1st ed., 2012.

[75] H. Edelsbrunner and R. Seidel, "Voronoi diagrams and arrangements," *Discrete & Computational Geometry*, vol. 1, p. 25–44, 1986.

[76] K. Q. Brown, "Voronoi diagrams from convex hulls," *Information Processing Letters*, vol. 9, no. 5, pp. 223–228, 1979.

[77] F. P. Preparata and S. J. Hong, "Convex hulls of finite sets of points in two and three dimensions," *Commun. ACM*, vol. 20, p. 87–93, Feb 1977.

[78] S. Cole, P. Sewell, A. Vukovic, and T. M. Benson, "Adaptive meshing for optical resonators," in *2012 14th International Conference on Transparent Optical Networks (ICTON)*, pp. 1–4, 2012.

[79] L. Chen and J. Xu, "Optimal Delaunay triangulations," *Journal of Computational Mathematics*, vol. 22, no. 2, pp. 299–308, 2004.

[80] Q. Du, V. Faber, and M. Gunzburger, "Centroidal voronoi tessellations: Applications and algorithms," *SIAM Review*, vol. 41, no. 4, pp. 637–676, 1999.

[81] P. Alliez, D. Cohen-Steiner, M. Yvinec, and M. Desbrun, "Variational tetrahedral meshing," *ACM SIGGRAPH 2005*, pp. 617–625, 2005.

[82] S. P. Lloyd, "Least squares quantization in PCM," *IEEE Transactions on Information Theory*, vol. 28, no. 2, pp. 129–137, 1982.

[83] S. Cole, *Relaxation and Adaptive Meshing for the Unstructured Triangular TLM Method*. University of Nottingham. Theses. Engineering, 2014.

[84] C. Geuzaine and J.-F. Remacle, "Gmsh: A three-dimensional finite element mesh generator with built-in pre-and post-processing facilities," *International Journal for Numerical Methods in Engineering*, vol. 79, pp. 1309–1331, 2009.

[85] P. Sewell, T. M. Benson, C. Christopoulos, D. W. P. Thomas, A. Vukovic, and J. G. Wykes, "Transmission-line modeling (TLM) based upon unstructured tetrahedral meshes," *IEEE Transactions on Microwave Theory and Techniques*, vol. 53, no. 6, pp. 1919–1928, 2005.

[86] D. de Cogan, "Time-step changes and parity effects in TLM thermal models," in *International Conference on Simulation '98. (Conf. Publ. No. 457)*, pp. 325–328, 1998.

[87] N. W. Ashcroft and N. D. Mermin, *Solid State Physics*. Holt, Rinehart and Winston, 1976.

[88] G. Pollack and D. Stump, *Electromagnetism*. Pearson, 2001.

[89] P. Gibbon, "Introduction to plasma physics," *CERN Yellow Reports*, pp. Vol 1 (2016): Proceedings of the 2014 CAS–CERN Accelerator School: Plasma Wake Acceleration, 2016.

[90] U. S. Inan and M. Gołkowski, *Principles of Plasma Physics for Engineers and Scientists*. Cambridge University Press, 2011.

[91] W. Baumjohann and R. A. Treumann, *Basic Space Plasma Physics*. Imperical College Press, 1996.

[92] A. S. Richardson, *NRL Plasma Formulary*. US Naval Research Laboratory, Sep 2019.

[93] M. I. Boulos, P. Fauchais, and E. Pfender, *Thermal Plasmas, Fundamentals and Applications, vol. 1*. Plenum Press, 1994.

[94] K. Yan, A. Vukovic, and P. Sewell, "Two-dimensional TE series node transmission-line modelling based on unstructured triangular meshes," in *2022 52nd European Microwave Conference (EuMC)*, pp. 448–451, 2022.

[95] L. J. Mendoza Herrera, D. M. Arboleda, D. C. Schinca, and L. B. Scaffardi, "Determination of plasma frequency, damping constant, and size distribution from the complex dielectric function of noble metal nanoparticles," *Journal of Applied Physics*, vol. 116, p. 233105, Dec 2014.

[96] B. Desiatov, I. Goykhman, and U. Levy, "Direct temperature mapping of nanoscale plasmonic devices," *Nano Letters*, vol. 14, no. 2, pp. 648–652, 2014. PMID: 24422562.

[97] C. D. Salzberg and J. J. Villa, "Infrared refractive indexes of silicon germanium and modified selenium glass," *Journal of the Optical Society of America*, vol. 47, pp. 244–246, Mar 1957.

[98] H. Chen, F. Wang, X. Xiong, Z. He, and Z. Yue, "Plasma discharge characteristics of segmented diverter strips subject to lightning strike," *Plasma Science and Technology*, vol. 21, p. 025301, Nov 2018.

[99] S. C. Brown, *Introduction to Electrical Discharges in Gases*. Wiley, 1966.

[100] Y. Liu, C. Zhang, E. R. Williams, C. Xiao, Z. Zhao, and S. Shen, "Numerical analysis of the criteria of arc root jump in lightning sweeping on resistive surface," in *2022 36th International Conference on Lightning Protection (ICLP)*, pp. 6–9, 2022.

[101] Q. Chen, B. Chen, and L. Shi, "Numerical study on EoS of lightning return stroke channels and its application in lightning discharge simulations," in *2014 International Conference on Lightning Protection (ICLP)*, pp. 533–539, 2014.

[102] K. Yan, A. Vukovic, P. Sewell, and T. M. Benson, "Two-dimensional thermal diffusion equation solver based on unstructured transmission-line modelling and optimal Delaunay triangular meshes," *IEEE Journal on Multiscale and Multiphysics Computational Techniques*, vol. 7, pp. 268–275, 2022.

[103] AE-2 Lightning Committee, "Aircraft Lightning Environment and Related Test Waveforms." SAE International, `https://www.sae.org/standards/content/arp5412a/`, 2005.